

NUMERICAL MODELING OF THE BEAD-MOBILITY TECHNIQUE

By

Jason Taylor

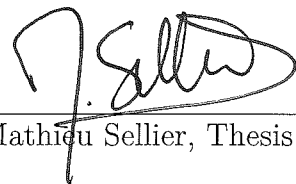
A Thesis Submitted to the Graduate

University of Canterbury

for the Degree of

MASTER OF ENGINEERING

Major Subject: MECHANICAL ENGINEERING



Dr Mathieu Sellier, Thesis Adviser

University of Canterbury
Christchurch, New Zealand

August 2017

CONTENTS

ACKNOWLEDGMENTS	iv
ABSTRACT	v
1. RESEARCH AND LITERATURE REVIEW	1
1.1 Atmospheric Aerosols	1
1.1.1 Origins	1
1.1.2 Composition	3
1.1.3 Formation	3
1.1.3.1 Technical Note: Mechanisms of Aerosol Growth	4
1.1.4 Deposition	5
1.1.5 Lifetime	7
1.1.5.1 Technical Note: Scattering	8
1.1.6 Atmospheric Effects	8
1.1.6.1 Direct Effect	9
1.1.6.2 Indirect Effect	10
1.2 The Importance of Particle Viscosity	11
1.2.1 Cloud Condensation Nuclei (CCN)	12
1.2.2 Uptake of Gases and Water	12
1.2.3 Oxidation	14
1.3 The Bead Mobility Technique	15
2. Theoretical Calculations	17
2.1 Key Parameters	17
2.2 Droplet Size and Shape	18
2.3 Flow Cell Analysis	19
2.4 Fluid Motion Within the Droplet	24
2.4.1 Governing Equation	24
2.4.2 Boundary Conditions	25
2.4.3 Solving Through Integration	25
2.4.4 Shear Stress at Droplet Surface	29
2.5 Comparison to Experimental Data	32
2.6 Reynolds Number of the Gas Phase	35
2.7 Bead Motion	38

3.	Model Development	40
3.1	Model Details	40
3.1.1	Multiphase Flow Interface	41
3.1.1.1	Interface Tracking Methods	42
3.1.2	Geometry	44
3.1.3	Materials	46
3.1.4	Boundary Conditions	46
3.1.5	Justification of Slip Condition over Symmetry	50
3.2	Mesh Study	52
3.2.1	Mesh Configuration	53
3.2.2	Mesh Convergence Variables	53
3.2.3	Water Domain Study	57
3.2.4	Droplet Domain Study	61
4.	Flow Analysis	66
4.1	Analytical Solution	66
4.2	Water Domain	67
4.3	Droplet Domain	73
4.3.1	Literature Comparison	75
4.3.2	Analytical Comparison	77
4.3.3	3D Analysis	78
4.3.4	Droplet Shape	81
4.3.5	Bead Circulation	83
4.3.6	Calculating a Measure of Average Bead Speed	88
5.	Parametric Studies	92
5.1	Droplet Drafting	92
5.2	Surface Tension	97
5.3	Size	100
5.4	Contact Angle	105
5.4.1	Study A	106
5.4.2	Study B	112
5.5	Viscosity	119
5.6	Summary of Parametric Studies	124
	REFERENCES	128

ACKNOWLEDGMENTS

I owe a great debt of gratitude to Dr Mathieu Sellier, Associate Professor and Deputy Head of Mechanical Engineering at the University of Canterbury. Dr Sellier has been an incredible supervisor for this project, for without his knowledge and expertise surrounding the computational modeling involved, this project would not have been completed. Secondly, I would like to express my gratitude to Professor Allan Bertram of the University of British Columbia for his guidance of the project and for allowing me to conduct research in his group as a visiting student. I would also like to thank CMC Microsystems for the provision of COMSOL Multiphysics and SolidWorks used throughout this project.

ABSTRACT

According to the Intergovernmental Panel on Climate Change, aerosols have been the most important atmospheric cooling component in the industrial period. However, the predictions of aerosol impacts are the largest individual source of uncertainty in climate models [1, 2]. Accurately representing organic aerosols (OA) in atmospheric models is one of the key requirements for understanding the climate effects of aerosols. The viscosity of OA's has been shown to range from liquid to solid/semi-solid across the range of atmospheric relative humidity [3]. The viscosity of these atmospheric particles is currently a topic of interest due to its role in the profound effect OAs have on the environment. A method known as the 'bead-mobility technique' has been developed by Renbaum-Wolff et al [4] which is able to quantify the viscosity of an atmospheric particle over a range of atmospherically relevant humidities by studying the motion of fluid inside small droplets placed in a flow cell. This project uses numerical simulations, in conjunction with an analytical solution, to provide validation of the technique and to investigate potential sources of error that could be contributing to the large uncertainties currently present in experimental results. As presented by Renbaum-Wolff et al, the relationship between the droplet viscosity and the droplet fluid velocity was found to fit a single term power law function of the form $u = a\mu^b$, where a and b represent constants with $b \approx -1$. The effect of variations in the droplet surface tension, size, contact angle and the effect of droplet drafting were analyzed over ranges relevant to the bead mobility technique. It was found that the largest contributors of error were due to the range of sizes and contact angles of droplets studied, producing variations in droplet velocity by factors of approximately 2.8 and 1.7 respectively. In light of these results, an alteration to the current technique has been proposed that reduces the errors present due to variations between droplets.

CHAPTER 1

RESEARCH AND LITERATURE REVIEW

1.1 Atmospheric Aerosols

1.1.1 Origins

Atmospheric aerosols are either emitted directly from the Earth's surface or formed by the condensation of gases in the atmosphere [5]. Particles emitted directly into the atmosphere as aerosols are known as Primary Organic Aerosols (POAs). Secondary Organic Aerosols (SOAs) are formed in the atmosphere through condensation of gas-phase precursors [6, 7]. Both of these types of aerosols can have anthropogenic (man-made) or natural origins [8, 9].

Aerosols of natural origins have been reported to make up as much as 90% of all aerosols in the atmosphere by mass [7, 8]. Some common natural sources include volcanic ash and biogenic emissions, as well as wind-blown sea salt and dust [9]. Alteration of the Earth's surface by processes such as deforestation, overgrazing and droughts can increase the rate at which aerosols enter the atmosphere [7].

Although global models show that aerosols due to anthropogenic sources are less abundant [10], they can dominate the air above urban and industrial areas mainly due to the combustion of fossil fuels [7, 9, 11]. In addition, recent studies have found correlations between tracers of urban pollution and organic aerosols [12, 13, 14]. This suggests that these types of emissions may have a larger effect than previously thought [7]. The correlations have been attributed not to large emissions of POA, but to rapid growth of SOA via photochemical processing [12, 15, 16]. Although one would expect these types of aerosols to be present only in highly populated regions, a large contributor to aerosols of anthropogenic origin on a global scale and the most important global source of sub-micrometer carbonaceous aerosol is Biomass burning [17]. Biomass Burning is a common method of clearing forests and consuming farm waste [7]. Aerosols produced by biomass burning are highest in concentration in the tropics, coinciding with regions of high biogenic aerosol formation [8].



Figure 1.1: Desert dust, volatile organic compounds from vegetation, smoke from forest fires, and volcanic ash are natural sources of aerosols. Photographs copyright (left to right) Western Sahara Project, Jonathan Jessup, Vox, Ludie Cochrane [7].

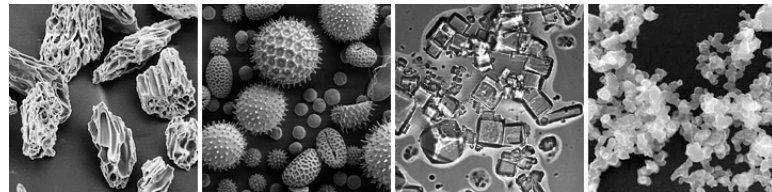


Figure 1.2: These scanning electron microscope images (not at the same scales) show the wide variety of aerosol shapes. From left to right: volcanic ash, pollen, sea salt, and soot [7]. Micrographs courtesy USGS, UMBC (Chere Petty), Arizona State University (Peter Buseck).

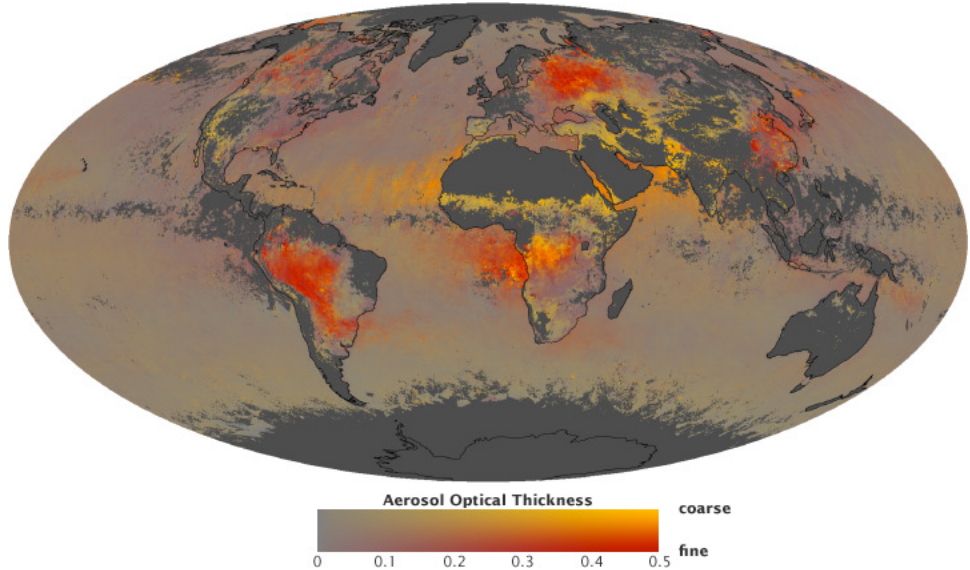


Figure 1.3: Measuring aerosol optical depth is a key method in quantifying the amount of aerosol in the atmosphere. Biomass burning is largely responsible for the amount of aerosol over the Amazon and Central Africa [7].

1.1.2 Composition

Atmospheric aerosols almost always consist of multiple elements. Figure 1.4 shows the typical composition of a fine continental aerosol particle in the lower troposphere. The most dominant fraction present are sulfates, produced mainly anthropogenically by fossil fuel combustion and naturally by volcanoes [5, 7]. These sources emit large amounts of sulfur dioxide which becomes sulfuric acid through oxidation in the stratosphere [11]. Due to its low vapor pressure, it then condenses to form the aqueous sulfate particles seen in figure 1.4. Organic carbon makes up 31% of the fine aerosol in non-urban areas and 24% in urban areas. This is attributed mainly to the condensation of large hydrocarbons produced biogenically and anthropogenically [5].

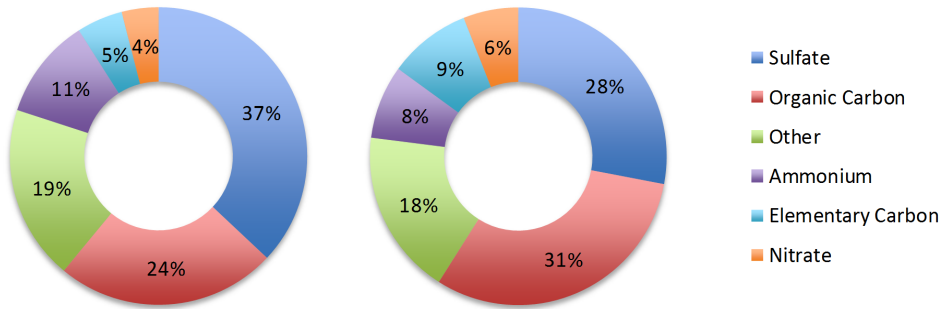


Figure 1.4: Typical compositions of atmospheric aerosols, both non-urban (left) and urban (right) [18].

1.1.3 Formation

POA's are emitted directly from the earth's surface and are driven by wind until they settle out. Contrastingly, SOAs are formed through a series of reactions and originate from gas-phase precursors [5, 8]. Figure 1.5 shows a simplified schematic of the cycle of aerosols, both primary and secondary.

Precursor gases are emitted and nucleate in the atmosphere to form ultra-fine aerosols. These ultra-fine aerosols grow rapidly via condensation and coagulation (random particle collisions) to become fine aerosols with diameters less than $1\mu m$ [18]. Aerosols originating via this method tend to accumulate in the $0.01\mu m - 1\mu m$ range because the relative size of the particle prohibits it from growing rapidly

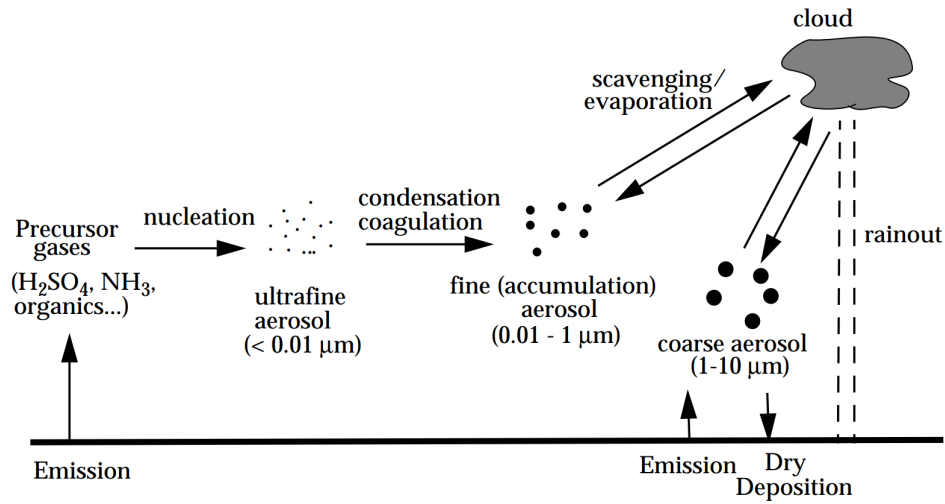


Figure 1.5: Production, growth and removal of atmospheric aerosols [5].

through condensation and the coagulation rate is reduced due to a decreased relative abundance [19, 5]. Coarse aerosols, such as wind-blown sea salt or soot from combustion, are emitted directly from the earths surface and tend to be much larger than their SOA counterparts [5]. It is important to note that although it has not been discussed here, in addition to size, the composition and structure of particles can be changed during this process [3, 10, 20].

1.1.3.1 Technical Note: Mechanisms of Aerosol Growth

It is important to note the different mechanisms involved in the process illustrated in figure 1.5 above. The first three processes involved in the formation of the aerosols; nucleation, condensation and coagulation are differentiated between in figure 1.5. Scavenging, rain-out and dry deposition are all forms of deposition and are covered in the section 1.1.4.

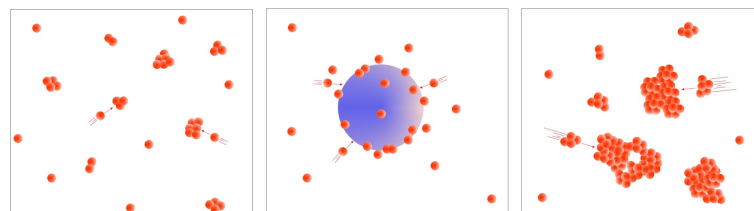


Figure 1.6: Homogeneous nucleation (left), condensation (middle) and coagulation (right) of aerosol particles [20]

1.1.4 Deposition

Deposition is the way in which the atmosphere cleans itself [21]. The two main deposition processes for aerosol particles are wet and dry deposition. Dry deposition describes the uptake of aerosols at the surface of the Earth whereas wet deposition describes the scavenging of aerosol from the atmosphere by precipitation [21, 22].

In rainy areas dry deposition can be neglected compared with wet deposition but can be the dominant mechanism in arid and semiarid regions where intense dust loadings take place [23], as well as being the dominant deposition process of micropollutants in highly industrialized areas [24]. Dry deposition occurs with several mechanisms like turbulent diffusion, sedimentation, Brownian Diffusion, interception, inertial forces, electrical migration, thermophoresis, and diffusiophoresis [20]. Deposition rates are governed by meteorological factors (wind velocity, relative humidity), particle characteristics (size and shape), and surface characteristics (friction velocity, microscale roughness, and temperature) [25, 26]. The dry deposition velocity is often used to quantify the rate at which aerosols are being deposited and is highly dependent on particle size. Ruijgrok et al [27] adopted a model by Sehmel and Hodgson (1980) to produce figure 1.7 which illustrates how the size of the particle influences its deposition velocity and the associated predominant mechanisms. Very fine particles ($< 0.1\mu m$) move mainly by Brownian motion, whereas the motion of larger particles ($> 1\mu m$) is dominated by sedimentation (gravitational) effects [21, 28]. Intermediate sized particles however, are strongly affected by impaction and interception phenomena [21]. This occurs when the aerosol collides with and is collected by an obstacle, such as a raindrop [20].

The wet removal of atmospheric particles by precipitation is by far the most efficient atmospheric aerosol sink [30]. Wet deposition describes the scavenging of soluble gases and aerosol particles from the atmosphere by precipitation [22]. An aerosol is removed from the atmosphere by precipitation when it becomes incorporated into a raindrop or snow particle that falls to the Earth's surface. Wet deposition occurs through either nucleation or impaction scavenging. Nucleation scavenging occurs within clouds when the aerosols serve as cloud condensation nuclei (CCN) or ice nuclei (IN) in the initial stage of cloud formation [23, 30]. The

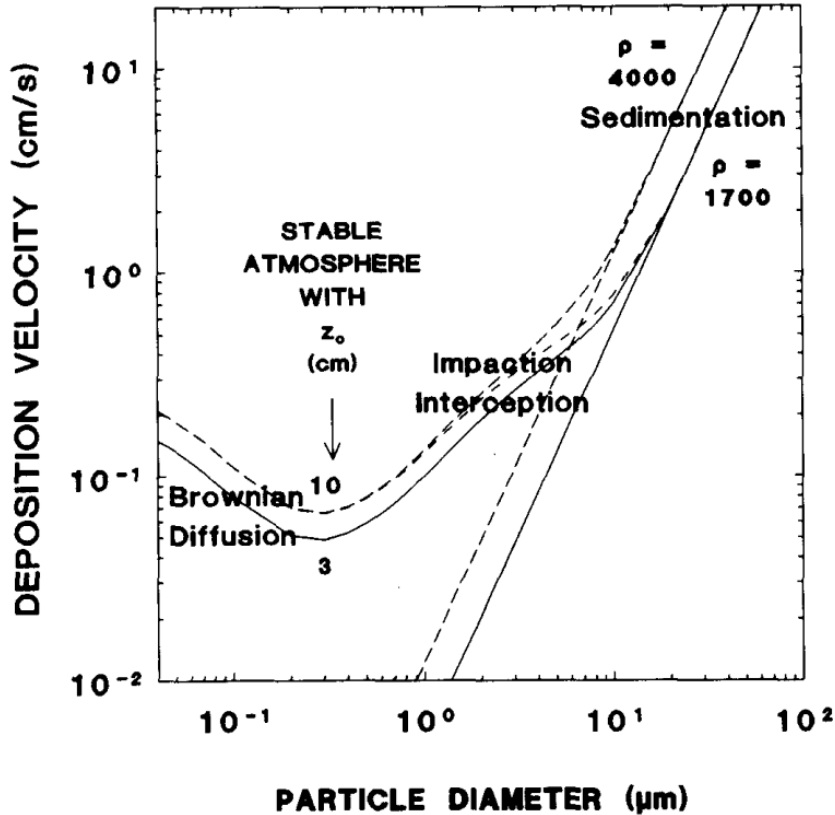


Figure 1.7: Typical Curves for the deposition velocity as a function of size in a stable atmosphere for two different roughness lengths (z_0 in [cm]) and particle densities (ρ in [kg m^{-3}]) using model described by Sehmel and Hodgson [29] with $u = 5 \text{ ms}^{-1}$ [27]

droplets then grow (mainly due to the ambient water vapor within the cloud) until they are large enough to precipitate out, carrying the aerosol within. This process of scavenging is a dominant process at the beginning of cloud formation and can deplete the original aerosol population in the air by up to 90%. In contrast, impaction scavenging transfers aerosol mass in the form of interstitial aerosol within the clouds and below-cloud aerosol into falling raindrops [20, 30]. This may occur through such mechanisms as Brownian Diffusion, interception, impaction or turbulent diffusion. Weak precipitation intensity can remove 50% to 80% of below-cloud aerosol, in both number and mass within 4 hours [23].

1.1.5 Lifetime

The lifetime of an aerosol in the atmosphere is a complex function of the aerosol's physical and chemical characteristics (e.g. particle size, chemical composition, etc.), the time and location of its release and of its resident altitude range [20, 31, 32]. The majority of aerosols (by mass) are located within the lower troposphere with a residence time of approximately 1-2 weeks [5]. As seen in figure 1.8, the smaller particles have a comparatively short lifetime (usually less than a day) as they are effectively removed by coagulation to form larger particles. Similarly, larger particles also have a short lifespan as they fall out quickly due to sedimentation (see figure 1.7, section 1.1.4 regarding settling velocity as a function of particle size) [20, 9]. Aerosols that exist in the Stratosphere, most commonly deposited as a result of sulfates released by large volcanic eruptions, can be suspended for at least up to a year [31]. The extended lifetime of aerosols at this altitude can be attributed mainly to the comparatively low precipitation to that of the lower troposphere [5, 33].

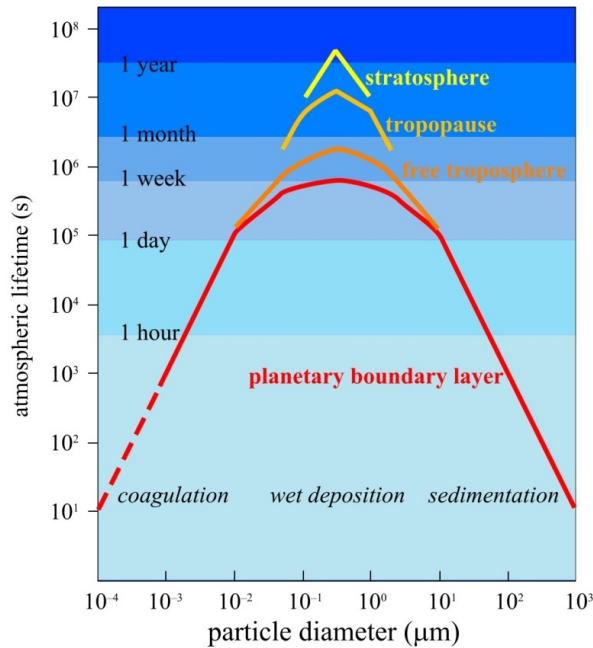


Figure 1.8: Typical size-dependent residence times of particles in the atmosphere and the associated common deposition mechanisms [20].

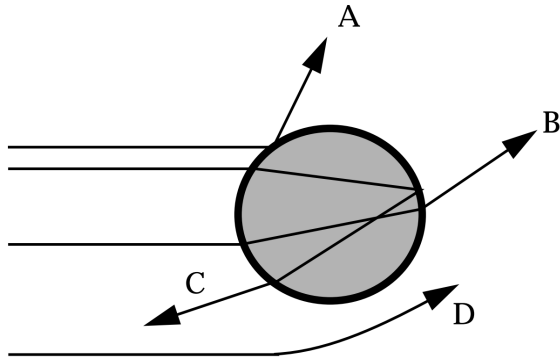


Figure 1.9: Scattering of a radiation beam; processes of reflection (A), refraction (B), refraction and internal reflection (C), and diffraction (D) [5]

1.1.5.1 Technical Note: Scattering

The atmospheric effects of aerosols are in part described through a phenomenon known as scattering. Incoming radiation from the sun is scattered when its direction of propagation is altered without absorption taking place [5], as illustrated in figure 1.9. The radiatively important properties of atmospheric aerosols (both direct and indirect) are determined at the most fundamental level by the aerosol composition and size distribution [9, 34]. Scattering is maximum for a particle radius corresponding to the wavelength of radiation. Consequently, accumulation mode are efficient scatterers of solar radiation [5].

1.1.6 Atmospheric Effects

Aerosols play a major role in determining the amount of solar energy that heats the earth [7, 35]. The addition of aerosols to the atmosphere alters the intensity of sunlight scattered back to space and the amount that is absorbed in the atmosphere. Clouds seeded by aerosols and aerosols themselves intercept approximately a quarter of all sunlight, preventing it from warming the earth's surface [7]. Incoming radiation can be absorbed or scattered by aerosol particles (the direct effect) or absorbed or reflected by the clouds formed through aerosols (the indirect effect) [3, 9, 36]. Such perturbations of sunlight by aerosols are defined by the resulting radiative forcing (RF). Most aerosols are brighter and more reflective than land or ocean and act to cool the earth by reflecting the sun's energy back into space [7].

Although the effect of aerosols on the earth's energy budget opposes that of global warming, it cannot simply be described or used as a countermeasure. The spatial and temporal non-uniformity of the aerosol RF's mean the net effect on Earth's climate is not simply a fractional offset to the effects of forcing by anthropogenic greenhouse gases [36].

1.1.6.1 Direct Effect

Dependent mainly on their physical properties, different aerosols scatter or absorb sunlight to varying degrees [1]. In broad terms, brighter and more translucent particles will tend to reflect radiation whereas darker aerosols tend to absorb the incoming light [7]. An example of this is the surface cooling caused by anthropogenic black carbon (an absorptive aerosol) shown in figure 1.10.

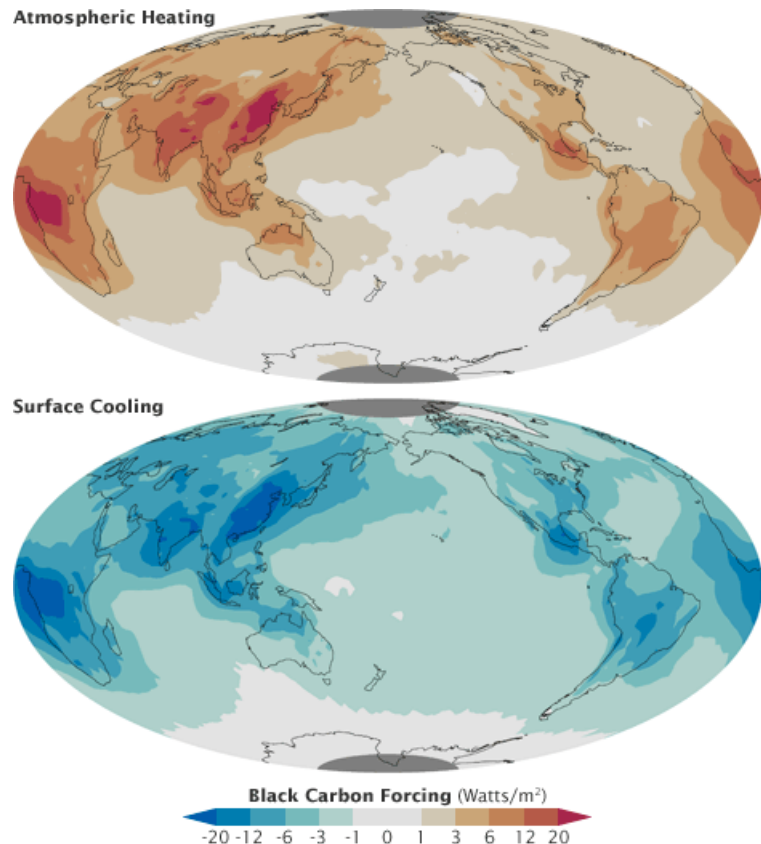


Figure 1.10: Black carbon aerosols absorb sunlight acting to warm the atmosphere containing the carbon (above) whilst cooling the surface below (below) [7]

In addition to scattering and absorbing radiation in the atmosphere, aerosols can alter the albedo of the planet [7]. Albedo (A) is a measure of the reflectivity of the earth's surface and is defined as a fraction of incoming solar energy that is reflected back into space [37], or formally [38]:

$$A = \frac{\text{reflected light}}{\text{incident light}}$$

Albedos range from that of a black body ($A = 0$) which absorbs all incident light, to an object that reflects all light and absorbs none ($A = 1$) [37]. The albedo can be influenced by areas of ice such as the polar caps which reflect a large amount of radiation, and contrarily, the ocean tends to absorb radiation producing a net cooling effect. Aerosols, black carbon in particular, can lessen the reflectivity of surfaces through the deposition of dark sediment [7].

1.1.6.2 Indirect Effect

As mentioned previously, aerosols influence cloud properties through their role as CCN and/or IN [39]. Briefly, although dependent on a number of factors [40], CCN are particles that, in the presence of supersaturated water vapor, activate to become cloud and fog droplets [41, 42]. IN form ice particles mainly through heterogeneous nucleation by several mechanisms such as deposition, condensation freezing, immersion and others [43]. High aerosol particle concentrations, such as that which occurs in a polluted atmosphere, increases the ambient concentration of CCN and IN. A CCN increase can lead to more cloud droplets so that, for fixed cloud liquid water content, pollution rich clouds have more numerous but smaller droplets. This effect leads to brighter clouds as the increased number of droplets provide more surfaces for reflection. This is known as the cloud albedo effect and is analogous to crushed ice being more reflective than a solid block as a result of increased scattering [7, 36]. Similarly to the direct albedo effect, the cloud albedo effect acts to cool the surface, as shown in figure 1.11.

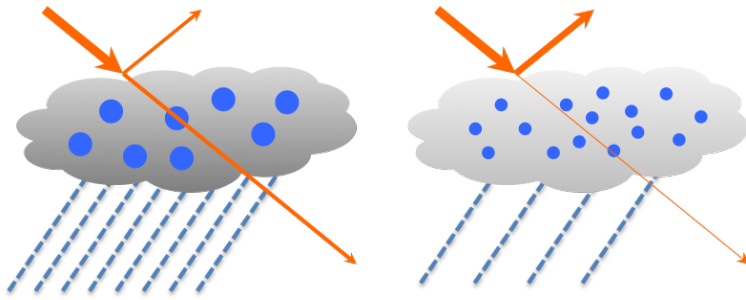


Figure 1.11: The cloud albedo effect. Clouds containing more droplets are more reflective to sunlight and have a larger cooling effect on the underlying earth [44]

1.2 The Importance of Particle Viscosity

Renbaum-Wolff et al [3] have shown that aerosols of hygroscopic nature can exhibit phases ranging from liquid to solid/semi-solid across the range of atmospheric relative humidity. The viscosity of organic aerosols is of utmost importance as it affects the particles ability to accommodate water and act as CCN or IN, influences the partitioning of water and gases, changes the atmospheric lifetime of the particles, and affects the rate of heterogeneous chemical reactions [45]. The particle property that affects the above phenomena may be referred to as either viscosity or diffusivity as the two properties are intimately linked via the Stokes-Einstein equation [4, 40]. This relation allows the diffusivity constant to be calculated through conversion of the aerosol viscosity. The Stokes Einstein equation is defined in equation 1.1.

$$D_{org} = \frac{kT}{6\pi a\nu} \quad (1.1)$$

Where :

- D_{org} is the molecular self diffusion coefficient [$m^2 s^{-1}$]
- k is the Boltzmann constant [$1.38 \times 10^{-23} JK^{-1}$]
- T is the temperature [K]
- a is the effective molecular radius [m]
- ν is the dynamic viscosity [Pas]

1.2.1 Cloud Condensation Nuclei (CCN)

As detailed in described in section 1.1.6.2, aerosols can dramatically cool the earth's surface through the cloud albedo effect. On a global scale, the cloud albedo effect represents one of the largest uncertainties in calculations of climate change [1, 39, 46].

The size distribution of particles is crucial in determining the effect on aerosols on CCN numbers as only particles with diameters larger than approximately 30nm to 100nm can act as CCN. If organic mass tends to condense on ultra-fine aerosols ($< 0.01\mu\text{m}$), more particles will reach a climatically relevant size resulting in a larger number of CCN particles. However if aerosols condense preferentially on larger particles ($> 1\mu\text{m}$), the number of CCN particles will be reduced [19]. The driving force for this condensation is the difference between the ambient vapor partial pressure and the equilibrium partial pressure of the particle surface. The dynamics of the resulting mass transfer are governed in part by the laws of diffusion (also in part by gas kinetic theory) [19, 46].

1.2.2 Uptake of Gases and Water

Renbaum-Wolff et al [3] and Vronique et al [39] reported that large scale modelling studies often use the assumption that equilibrium between gas-phase organic compounds and the bulk of secondary organic particles is rapidly achieved. This implies that diffusion occurs quickly in comparison to accommodation [3, 47, 48]. However, through use of a kinetic flux model, Shiraiwa and Seinfeld [47] have estimated the equilibration timescale can be in the order of days. This is due to a higher viscosity imposing kinetic limitations which increases the time taken for equilibrium to be achieved between the gas and particle phases [6].

This has implications for the mass transport provided by atmospheric particles as the chemical lifetime of reactive compounds can increase from seconds to days depending on the diffusivity of the particles [40, 47, 48]. As detailed in section 1.1.5, the lifetime of these particles depend on the competition between their condensational growth and coagulation scavenging. Thus both nucleation rates and condensational growth of ultra-fine particles must be accurately represented in

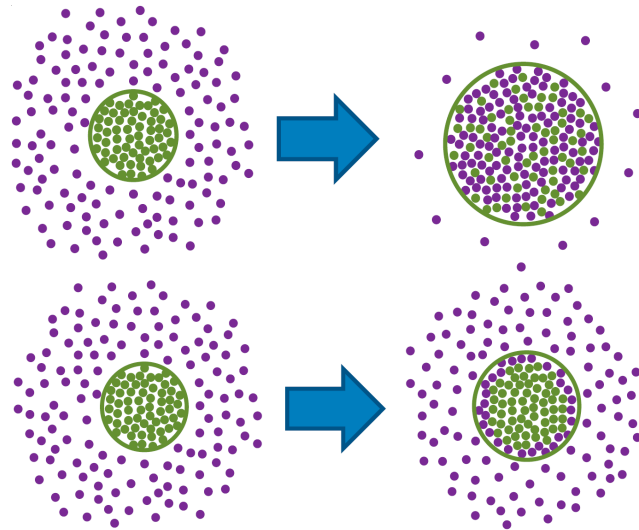


Figure 1.12: Difference in growth of an atmospheric particle by uptake of organic compound for less viscous (upper) and more viscous (lower) particles for the same elapsed time [3]

large-scale atmospheric models [19, 20]. Figure 1.12, taken from Renbaum-Wolff et al [3], illustrates the difference in the uptake of organic compound uptake for a low and high viscosity particle over the same elapsed time. Formally, the characteristic time of mass transport and mixing of gas or water molecules is defined by Shiraiwa et al [40] as:

$$\tau_{cd} = \frac{d_p^2}{4\pi^2 D} \quad (1.2)$$

Where :

- τ_{cd} is the e-folding time of equilibration¹ [s]
- d_p is the atmospheric particles' diameter [m]
- D is the diffusion coefficient of the atmospheric particle [$m^2 s^{-1}$]

¹For partitioning, the e-folding time is the time after which the concentration in the particle core deviates by less than a factor of 1e from the equilibrium value.

1.2.3 Oxidation

The oxidation of atmospheric particles occurs through gas-phase compound uptake (described in section 1.2.2) of atmospheric oxidants such as ozone. The physiochemical properties of atmospheric particles (i.e. chemical composition, size, shape etc) change over time in part due to reactions with gas-phase atmospheric oxidants. The rate of heterogeneous reaction between a condensed phase particle and a gas phase species can be represented by its uptake coefficient (γ) [49]. This uptake coefficient is defined as a ratio of:

$$\gamma = \frac{\text{fractional net loss of gas phase species}}{\text{gas phase collision rate}}$$

The fractional net loss is governed mainly by the diffusion of the atmospheric particle whilst in a condensed phase state [49]. Renbaum-Wolff et al [3] provide a schematic of the effect of particle viscosity on heterogeneous oxidation by ozone (figure 1.13).

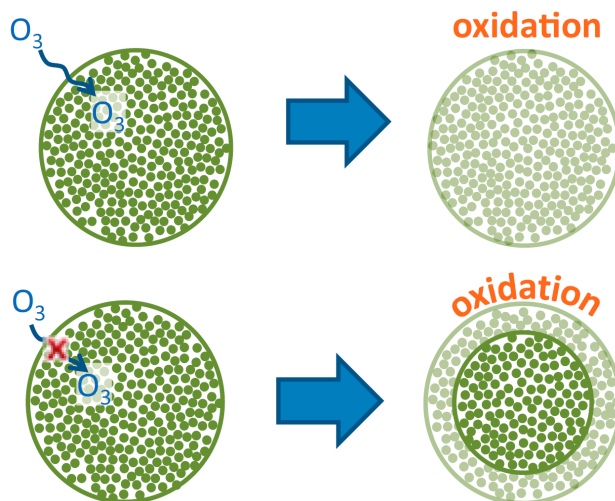


Figure 1.13: Difference in extent of oxidation of an atmospheric particle by uptake of ozone for less viscous (upper) and more viscous (lower) particles for the same elapsed time [3].

1.3 The Bead Mobility Technique

Classical macroscopic rheometry techniques typically require sample volumes of approximately $1ml$ and involve characteristic length scales of approximately $1mm$ [50]. Such large consumptions of fluid is not appropriate for many biological and medical samples which are typically limited to a microliter [51]. In order to decrease the amount of fluid required, many macro-scale devices have been adapted to incorporate micrometric scales. For example Srivastava and Burns [52] developed a silicon-glass hybrid microfluidic device and Muller et al [53] scaled down the classical falling ball method to create a new microviscometer. New techniques such as fluorescence microscopy can study samples as small as single cells however are typically limited viscosities less than $10Pas$ [54, 55]. Unfortunately a common issue associated with the above three techniques is the expensive or complex setup of instrumentation that is required. Han et al [51] developed a PDMS based microliter viscometer however has only been validated up a viscosity $80\ mPas$. Nano scale rheometry can be studied through atomic force microscopy or surface force instruments which both require a small sample volume however instrument artifacts can overwhelm observations facilitating the need to introduce large correction factors in order to compensate for flow non-idealities. In addition, atomic force microscopy is limited to low viscosities ($\leq 5 \times 10^{-2} Pas$) due to the strong dissipative effects which occur at higher viscosities [50].

Although the above techniques are capable of studying the rheometry of very small samples, a common shortcoming is the limitation on the viscosity range. A technique able incorporate a larger range, particularly higher viscosities is needed for applications such as the study of environmental chamber samples. The bead mobility technique is capable of determining viscosities in the range ($10^{-3} < \eta < 10^3 Pas$), a large range in comparison to the techniques outlined above. In addition to this, it only requires $\approx 1\mu l$ of sample, comparable to many microviscometer techniques and adequate for the intended study of environmental chamber samples. A second recurring drawback of existing techniques is the requirement of complex or expensive equipment, however the bead mobility technique utilizes instruments commonly found in laboratories [4].

The bead mobility technique was developed by Renbaum-Wolff et al [3, 4] at the University of British Columbia, Vancouver, Canada. This unique method was devised in order to measure the viscosity of small samples ($< 1\mu l$) over a wide range of viscosities of small samples ($10^{-3} < \eta < 10^3 \text{ Pas}$). Atmospheric aerosols are often produced in labs using environmental chambers yielding small sample volumes, on the order of micro-liters. This method allows real time control over relative humidity (RH) making it capable of simulating atmospheric conditions. This, combined with the small sample volume requirement and viscosity range make this technique highly applicable to the study of atmospheric aerosols. Through this method, the viscosities of secondary organic material produced by α -pinene ozonolysis are quantified for relative humidities between 70% and 90%. The viscosity of the particles were found to range from 791 Pas at 70% RH (comparable to peanut butter) to 6.25 Pas (comparable to honey) at 90% RH.

As a brief summary of the technique, particle material is reduced to a fine mist and sprayed onto a hydrophobic slide. The sample fluid is collected on a slide forming super-micron droplets, typically $20\mu m$ to $50\mu m$ in diameter. In order to visualize the internal circulation of the fluid inside the droplets, a dilute suspension of hydrophilic melamine beads is sprayed over the slide and allowed to settle into the sample droplets. The slide is then placed inside a flow cell with a gas flow velocity of approximately $1ms^{-1}$. The gas is constituted of a mixture of nitrogen and water with the relative humidity of the flow being controlled in real time. The movement of the gas over the droplets generates a shear stress at the surface of the droplets, causing the fluid within the droplet to circulate. The movement of the beads within the droplets is tracked using an optical microscope and used to calculate an average bead velocity. The bead velocity is then used to calculate the droplet viscosity based on a calibration curve constructed using known standards.

CHAPTER 2

Theoretical Calculations

2.1 Key Parameters

Throughout this section there are several recurring parameters and material properties which for ease of reference are given below in tables 2.1 and 2.2. The properties of table 2.2 are taken from an online calculator [56] for Nitrogen at $22.5^{\circ}C$ under 1bar of pressure. These properties are assumed constant even though the relative humidity of the nitrogen changes during the experiment. The density of the droplet is defined as the value adopted by Pathak et al [57]. Two ranges of viscosities have been defined. Firstly, the viscosity range studied during the bead mobility tests of α -pinene particles, and secondly, the range of viscosities used to define the calibration curve. Both sets of experiments were conducted as presented by Renbaum-Wolff et al [3, 4].

Table 2.1: Relevant physical properties of Nitrogen

Property	Symbol	Value	Unit
Density	ρ_g	1.1404	kgm^{-3}
Kinematic Viscosity	ν_g	15.542×10^{-6}	m^2s^{-1}
Dynamic Viscosity	μ_g	17.712×10^{-6}	Pas

Table 2.2: Relevant physical properties of the Droplet

Property	Symbol	Value	Unit
Density	ρ_d	1000	kgm^{-3}
Dynamic Viscosity (alpha-pinene)	μ_d	$16.3 < \mu < 791$	Pas
Dynamic Viscosity (calibration curve)	μ_d	$10^{-3} < \mu < 10^3$	Pas

2.2 Droplet Size and Shape

Renbaum-Wolff et al [4] reported droplet diameters to range between $30\mu m$ and $50\mu m$. The analytical solution will therefore be formulated as an average solution using a radius of $20\mu m$ with upper and lower bounds of $25\mu m$ and $15\mu m$. The droplet radius used throughout this section is therefore defined as:

$$R = 20_{-5}^{+5} \mu m \quad (2.1)$$

Wolff also reported that the contact angles of the droplets ranged between 58° and 95° . For ease of calculation, the contact angle used for this theoretical section will be 90° . However, we cannot yet assume the droplet to have a spherical surface. In order to evaluate the curvature of the surface of the droplet, we need to calculate the Bond number (also known as the Eötvös number). The Bond number is a ratio of the influences from surface tension and body force of the droplet. We can use this dimensionless number to calculate the relative effect of gravity on the particle shape. Figure 2.1 is an illustration of the effect of surface tension of droplet shape. On inspection of figure 2.1, shape of the droplet on the right is the result of a lower surface tension, resulting in a droplet with a flatter apex and a less circular surface, corresponding to a higher Bond number. Contrastingly, the left droplet with a higher surface tension corresponds to a lower Bond number resulting in a more hemispherical shape. Body forces are considered to be negligible in comparison to surface tension if the Bond number is much less than one. The Bond number is calculated using equation 2.2.

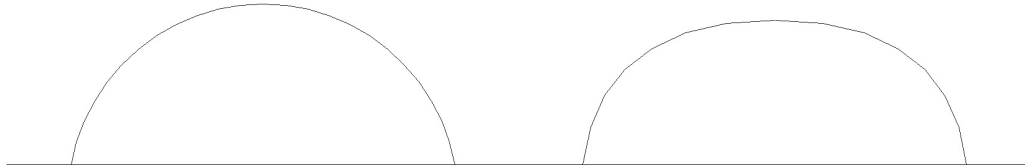


Figure 2.1: Illustration of droplets with low (left) and high (right) Bond numbers.

$$Bo = \frac{\Delta\rho g L^2}{\sigma} \quad (2.2)$$

Where :

- $\Delta\rho$ is the difference in density between the droplet and gas phases
- g is the acceleration due to gravity
- L is the characteristic length, in this case the droplet diameter
- σ is the surface tension of the droplet

For the purpose of this calculation, as the surface tension of the droplet is unknown, we will assume it to be equal to that of water at room temperature. Water is considered to have a high surface tension coefficient of $0.07275 Nm^{-1}$ at $20^\circ C$ [58, 59]. We will also assume the largest diameter of $50\mu m$ as a conservative assumption. The Bond Number of the particles is much less than one, therefore surface tension dominates and the droplet can be safely assumed to take on a spherical shape.

$$Bo \approx \frac{(1000 - 1.1404) \times 9.81 \times (50 \times 10^{-6})^2}{0.0728}$$

$$\therefore Bo \approx 3.36 \times 10^{-4} \ll 1$$

2.3 Flow Cell Analysis

On inspection of the flow cell in figure 2.2, the gas phase is seen to enter the cell through an inlet and undergoes a sudden expansion into the main body of the cell. This creates flow separation as characteristically seen in figure 2.3 and may subject the particles to unstable and turbulent flow. With reference to figure 2.3, although the flow may be fully developed at cross section 1, the sudden expansion of the flow channel causes separation and is not stable again until cross section 2. To determine whether the experiment exposes the particles to unsteady flow, we will calculate an approximate reattachment point of the mainstream flow as a result of the sudden expansion. Renbaum-Wolff et al [4] reported an experimental flow rate of $1.2 Lmin^{-1}$. This is converted to the inlet velocity through the $3mm$ diameter inlet using the unit conversion of equation 2.3. The Reynolds number of the flow at the inlet is then calculated using equation 2.4.

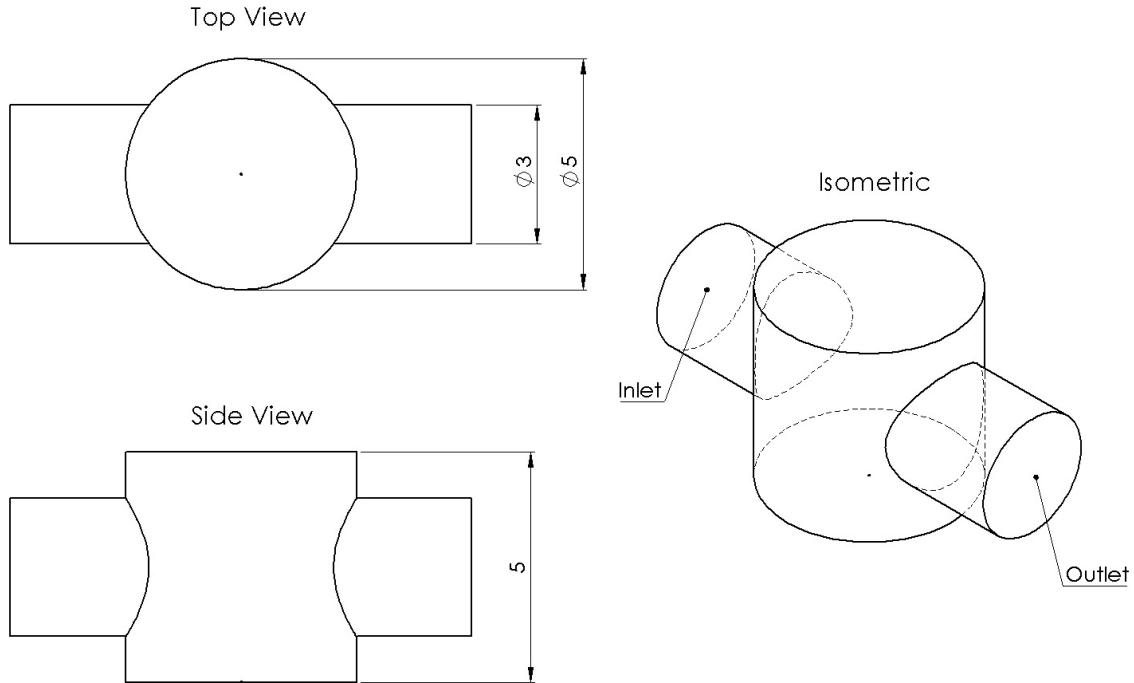


Figure 2.2: Geometry of the flow cell. A single droplet has been placed in the centre of the lower surface of the cell to show the size of a droplet relative to the dimensions of the flow cell.

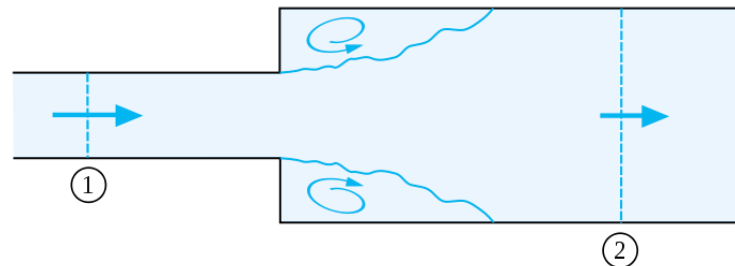


Figure 2.3: Illustration of flow separation in pipe flow due to sudden expansion [60].

Calculating inlet velocity :

$$\begin{aligned}
 \text{Inlet Velocity} &= \left[\frac{L}{min} \right] \times \left[\frac{m^3}{L} \right] \times \left[\frac{min}{s} \right] \times \left[\frac{1}{m^2} \right] = \left[\frac{m}{s} \right] \quad (2.3) \\
 &= 1.2 \times \frac{1}{60} \times \frac{1}{1000} \times \frac{1}{(\pi \times 0.0015^2)} \\
 &= 2.829 m s^{-1}
 \end{aligned}$$

Corresponding Reynolds number :

$$Re = \frac{(V_g D)}{\nu_g} \quad (2.4)$$

Where :

- V_g is the average gas velocity at the inlet
- D is the diameter of the inlet
- ν_g is the kinematic viscosity viscosity of the gas

$$Re = \frac{2.829 \times (5 \times 10^{-3})}{15.542 \times 10^{-6}} = 546$$

This calculation shows the gas phase to be laminar as a value of 546 is below the critical Reynolds number of 2300 [61] designating the upper limit of laminar flow. This Reynolds number can now be used to calculate the size of the region of recirculation produced by the sudden expansion. Cantwell et al [62] studied the effect of a sudden expansion in a circular pipe on the extent of flow separation. Although the flow cell's circular inlet is expanding into a non-circular domain in the direction of flow, the results of Cantwell et all will suffice for the purpose of the calculation. Cantwell et al reported that the length of the region of recirculation after a sudden expansion (x) is dependent on both the step height (h) and the Reynolds number of the flow. The result was found to be linear and is expressed as the ratio presented in equation 2.5.

$$\frac{x}{h} = 0.0876 Re \quad (2.5)$$

$$\frac{x}{(1/2)(0.005 - 0.003)} = 0.0876 \times 346$$

$$\therefore x = 30mm$$

Therefore, the region of recirculation caused by the sudden expansion would theoretically extend 30mm downstream. However, with the flow cell body being only 5mm from inlet to outlet, this result definitively shows that the particles are

not being subjected to steady mainstream flow but rather an unsteady region of unknown velocity making predictions difficult. The moderately high Reynolds number combined with a relatively large step height results in the mainstream flow passing over the lower section of the cell where the droplets are located.

It should be noted that the flow characteristics in the body of the cell are more complex than assumed here for two reasons. Firstly, the sudden expansion is closely followed by a sudden contraction adding to the complexity of the flow. Secondly, as seen in figure 2.2, the body of the cell is a cylinder oriented perpendicular to the flow. Therefore, after the expansion, the flow essentially enters a duct of varying width. Both of these factors are not taken into account in the above calculations, however, considering the relative lengths of the cell and separation regions, the above outcome can be assumed to be reliable. The flow immediately surrounding the droplets is a key factor in determining the motion of the droplet fluid. Therefore, in order to better understand the motion of the nitrogen in relation to the flow over the droplets, a 2D COMSOL model was constructed (a 3D model was attempted but could not be completed).

The average inlet velocity, as calculated in equation 2.3, was used to define a laminar inflow condition at the inlet. This condition creates a steady state parabolic velocity profile based on the specified average velocity. The section of the flow cell is part of a larger system, with the inlet and outlet boundaries defined in figure 2.2 continuing as tubing. This laminar inflow condition allows the inlet to be modeled with a fully developed profile, as in the experiment, without having to extend the inlet tube to an appropriate entry length. Figures 2.4 and 2.5 show the velocity field and streamlines selected to describe the general motion of the flow with the mainstream flow moving from left to right. It should be noted that the black lines of the geometry crossing the flow region are only present as the model was built by overlapping a square and a rectangle and do not impede the flow in any way. The results of the modeling concur with the expected behavior based on the flow reattachment calculations. The mainstream flow moves across the cell with only a small amount of momentum being transferred into the upper and lower sections of the cell. The region of the cell containing the droplets is in fact subjected to a recirculated

flow moving in the opposite direction to the inlet flow and at a much lower velocity. The velocity profile calculated from a vertical line through the center of the flow cell and is shown in figure 2.6. The results of this modeling are used to calculate the analytical solution for the motion of the fluid inside the droplets as detailed in section 2.4.

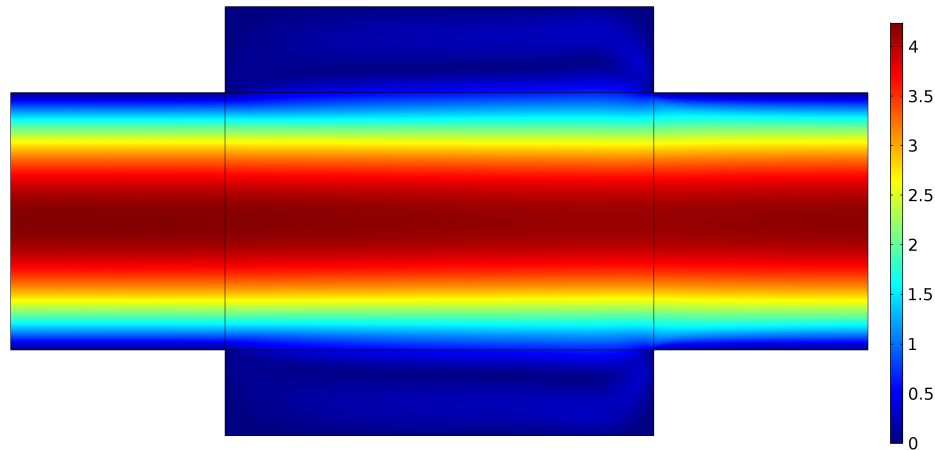


Figure 2.4: Velocity Surface plot of Nitrogen passing through experimental flow cell

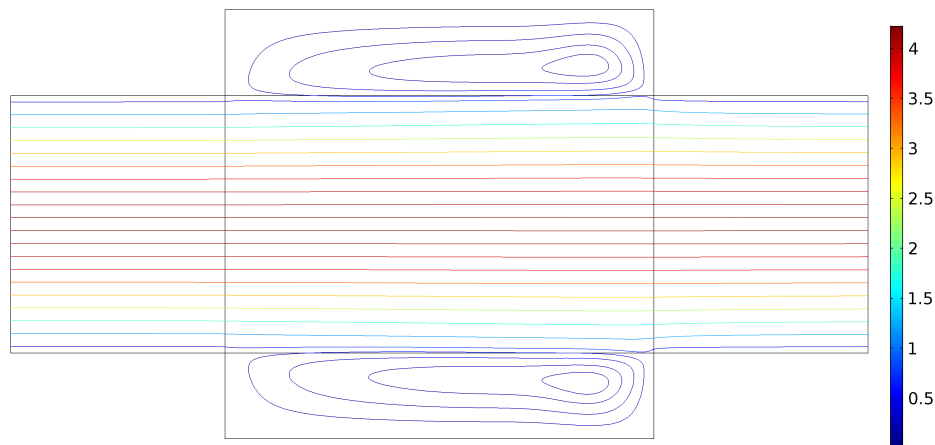


Figure 2.5: Streamlines showing mainstream flow of Nitrogen passing through experimental flow cell with regions of flow recirculation in the upper and lower sections of the cell

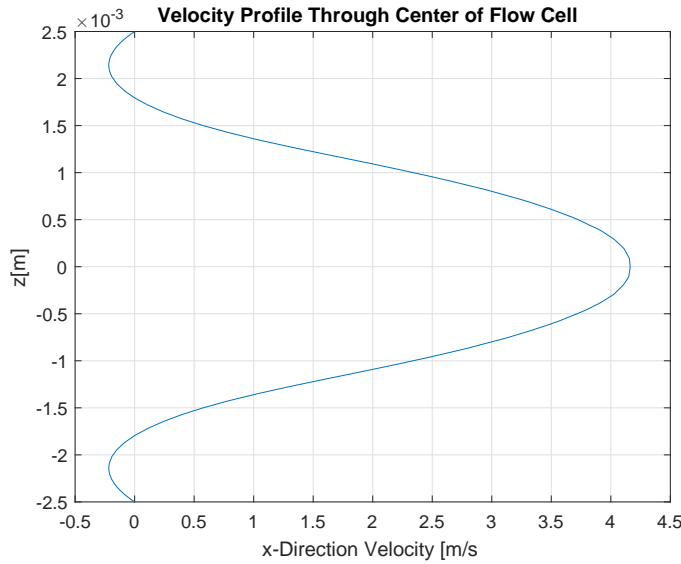


Figure 2.6: x-Direction velocity profile vertically through the center flow cell from the lower to upper surface showing the reverse direction of flow surrounding the droplets

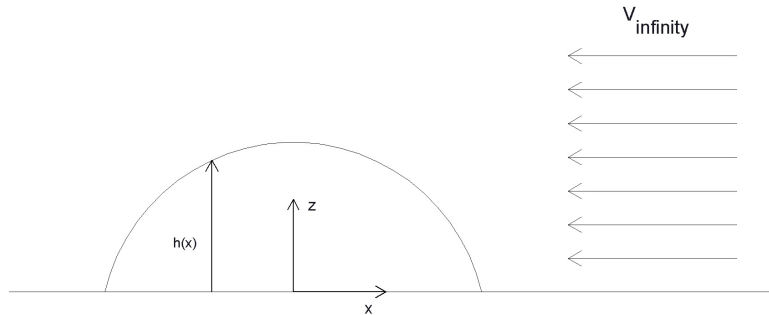


Figure 2.7: Coordinate system used for droplet flow calculations.

2.4 Fluid Motion Within the Droplet

2.4.1 Governing Equation

Figure 2.7 shows the coordinate system for the problem with the origin at the droplet's center. The Navier-Stokes equation in the x-direction is simplified based on the assumption that inertial effects are negligible and the flow is effectively unidirectional. The resulting momentum equation in the x-direction balances viscous stresses and the pressure gradient within the droplet. The resulting second order differential equation is shown in equation 2.6.

$$\mu \frac{\partial}{\partial z} \left(\frac{\partial u}{\partial z} \right) = \frac{\partial p}{\partial x} \quad (2.6)$$

Where :

- u is the velocity in the x direction
- $\frac{\partial p}{\partial x}$ is the pressure gradient in the x direction
- μ is the dynamic viscosity of the droplet phase

2.4.2 Boundary Conditions

1. The hydrophobic surface on which the droplet is positioned exhibits the no slip condition :

$$u(z=0) = 0 \quad (2.7)$$

2. The droplet's surface is subject to a shear stress generated by the flow of gas over the droplet :

$$\mu \left(\frac{\partial u}{\partial z} \right) (z=h) = \tau_s \quad (2.8)$$

2.4.3 Solving Through Integration

Equation 2.6 can then be integrated twice in conjunction with boundary conditions 2.7 and 2.8 to find the velocity of the flow within the droplet.

$$\mu \int \left(\frac{\partial}{\partial z} \left(\frac{\partial u}{\partial z} \right) \right) dz = \int \left(\frac{\partial p}{\partial x} \right) dz$$

$$\mu \frac{\partial u}{\partial z} = \frac{\partial p}{\partial x} z + A$$

Apply boundary condition 2.8 to solve for the first constant of integration (A) :

$$\tau_s = \frac{\partial p}{\partial x} h + A$$

$$\therefore A = \tau_s - \frac{\partial p}{\partial x} h$$

After one integration, the governing equation is now in the form :

$$\mu \frac{\partial u}{\partial z} = \frac{\partial p}{\partial x} (z - h) + \tau_s$$

Integrate a second time :

$$\begin{aligned} \mu \int \left(\frac{\partial u}{\partial z} \right) dz &= \int \left(\frac{\partial p}{\partial x} (z - h) + \tau_s \right) dz \\ \mu u &= \frac{\partial p}{\partial x} \left(\frac{z^2}{2} - zh \right) + \tau_s z + B \end{aligned}$$

Apply boundary condition 2.7 to solve for the second constant of integration (B) :

$$0 = \frac{\partial p}{\partial x} (0 - 0) + 0 + B$$

$$\therefore B = 0$$

The velocity profile is therefore :

$$u(z) = \frac{1}{\mu} \frac{\partial p}{\partial x} \left(\frac{z^2}{2} - zh \right) + \frac{\tau_s z}{\mu} \quad (2.9)$$

At this stage, the equation contains two unknowns :

1. The pressure gradient $(\frac{\partial p}{\partial x})$
2. The shear stress caused by the gas at the surface of the droplet (τ_s)

In order to find an expression for the pressure gradient, we can apply the conservation of mass. If we assume the system has reached a steady state and therefore the droplet shape is unchanging in time, we can equate the mass fluxes through any plane normal to the flow. That is to say, on observation of figure 2.8, the areas defined by the velocity profile on the left and right sides of the $x = 0$ line are equal, thus the flux is equal to zero.

Mathematically this can be evaluated by integrating the velocity profile (equation 2.9) over the height of the droplet (from 0 to h) and equate it to zero:

$$\int_0^h (u(z)) \, dz = 0$$

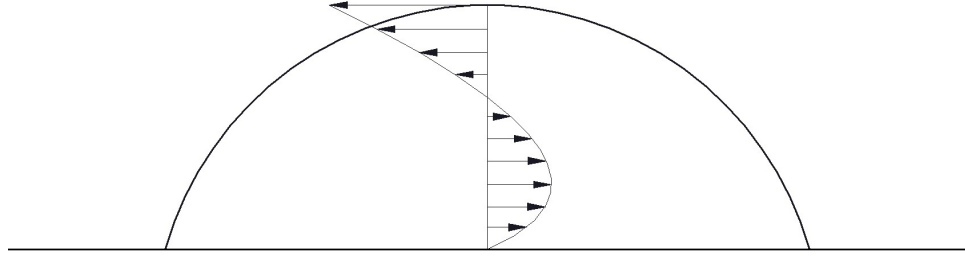


Figure 2.8: Illustration of the velocity profile of the droplet fluid at $x = 0$.

$$\int_0^h \left[\frac{1}{\mu} \frac{\partial p}{\partial x} \left(\frac{z^2}{2} - zh \right) + \frac{\tau_s z}{\mu} \right] dz = 0$$

$$\left[\frac{1}{\mu} \frac{\partial p}{\partial x} \left(\frac{z^3}{6} - \frac{z^2 h}{2} \right) + \frac{\tau_s z^2}{2\mu} \right] \Big|_0^h = 0$$

Evaluating at h and 0 and subtracting :

$$\left[\frac{1}{\mu} \frac{\partial p}{\partial x} \left(\frac{h^3}{6} - \frac{h^3}{2} \right) + \frac{\tau_s h^2}{2\mu} \right] - 0 = 0$$

Rearranging for $\frac{\partial p}{\partial x}$:

$$\frac{1}{\mu} \frac{\partial p}{\partial x} \left(\frac{2h^3}{6} \right) = \frac{\tau_s h^2}{2\mu}$$

$$\frac{\partial p}{\partial x} \left(\frac{h^3}{3} \right) = \frac{\tau_s h^2}{2}$$

$$\frac{\partial p}{\partial x} = \frac{3\tau_s}{2h}$$

This term can then be substituted into the velocity profile :

$$u(z) = \frac{1}{\mu} \frac{3\tau_s}{2h} \left(\frac{z^2}{2} - zh \right) + \frac{\tau_s z}{\mu} \quad (2.10)$$

Rearranging into quadratic form :

$$u(z) = z^2 \left(\frac{3\tau_s}{4\mu h} \right) - z \left(\frac{3\tau_s}{2\mu} \right) + z \left(\frac{\tau_s}{2\mu} \right)$$

$$u(z) = z^2 \left(\frac{3\tau_s}{4\mu h} \right) - z \left(\frac{\tau_s}{2\mu} \right) \quad (2.11)$$

We now have an expression for the velocity profile anywhere in the droplet². An expression for the velocity at the free surface is found by equating $z = h$ into equation 2.10:

$$\begin{aligned}
 u(z = h) &= \frac{1}{\mu} \frac{3\tau_s}{2h} \left(\frac{h^2}{2} - h^2 \right) + \frac{\tau_s h}{\mu} \\
 &= \frac{1}{\mu} \frac{3\tau_s}{2h} \left(\frac{-h^2}{2} \right) + \frac{\tau_s h}{\mu} \\
 &= \frac{-3\tau_s h}{4\mu} + \frac{\tau_s h}{\mu} \\
 &= \frac{\tau_s h}{\mu} \left(\frac{-3}{4} + 1 \right) \\
 u(z = h) &= \frac{\tau_s h}{4\mu}
 \end{aligned} \tag{2.12}$$

Recalling h is a function of x , defining h using the equation for the surface of the droplet will result in the velocity over the surface of the droplet. The general equation of the surface is in the form:

$$x^2 + h^2 = R^2$$

Rearranging gives :

$$h = \sqrt{R^2 - x^2}$$

Substituting into eqation 2.12 :

$$u(z = h) = \frac{\tau_s (\sqrt{R^2 - x^2})}{4\mu} \tag{2.13}$$

We observe that the free surface velocity is proportional to both the applied shear stress (τ_s) and the particle thickness (h) whilst being inversely proportional to the droplet fluid viscosity (μ). A key point resulting from the above equation is that the free surface velocity is not constant. As we move along the surface of the

²Noting that although we have defined $u(z)$, the variable h representing the height of the droplet in the z direction is a function of x . We therefore have an expression for the velocity anywhere within our 2D domain.

droplet from the forward stagnation point (front of the droplet) toward the droplet apex, the droplet height (h) gradually increases, increasing the velocity. Therefore, moving from the forward stagnation point, the free surface velocity increases up to a maximum at the droplet apex and then decreases toward the rear stagnation point.

2.4.4 Shear Stress at Droplet Surface

Equations 2.13 and 2.11 are still defined in terms of an unknown; the shear stress on the droplet surface. The shear stress at the droplet surface can be approximated as equal to the shear on the lower surface of the flow cell, assuming the effect of the droplet to be negligible. Mathematically speaking we are approximating the shear stress at the surface of the droplet (τ_s) to be equal to the shear stress on the lower wall (τ_w):

$$\tau_s = \tau_w$$

The shear stress on the lower surface of the flow can be found using the COMSOL model described in section 2.3. Figure 2.9 shows the viscous stress on the lower surface, recalling the mainstream flow moving from the inlet on the left to the outlet on the right. The shear stress on the lower surface is higher near the outlet of the cell as the mainstream flow is diverted downwards at the location of the sudden contraction defining the outlet. This downward movement of flow causes a spike in the shear stress on the lower boundary which then normalizes as the flow is redirected parallel to the lower boundary. The shear stress is then seen to decrease as the flow loses momentum as it moves toward the inlet, in the reverse direction of the mainstream flow. This large variation in stress over the lower surface of the cell forces us to consider the shear on the droplet in terms of a range. The upper bound is defined as the maximum shear stress of 0.03743Nm^{-2} , occurring at $x = 1.8 \times 10^{-3}\text{m}$. The minimum value is therefore defined as the stress at $x = -1.8 \times 10^{-3}\text{m}$, equal to 0.00735Nm^{-2} . The average value is defined as the shear in the center of the lower surface, at $x = 0$, equal to 0.020543Nm^{-2} . The shear stress on the surface of the droplet is therefore defined as:

$$\tau_s = \tau_w = 0.02054^{+0.01689}_{-0.01319}\text{Nm}^{-2}$$

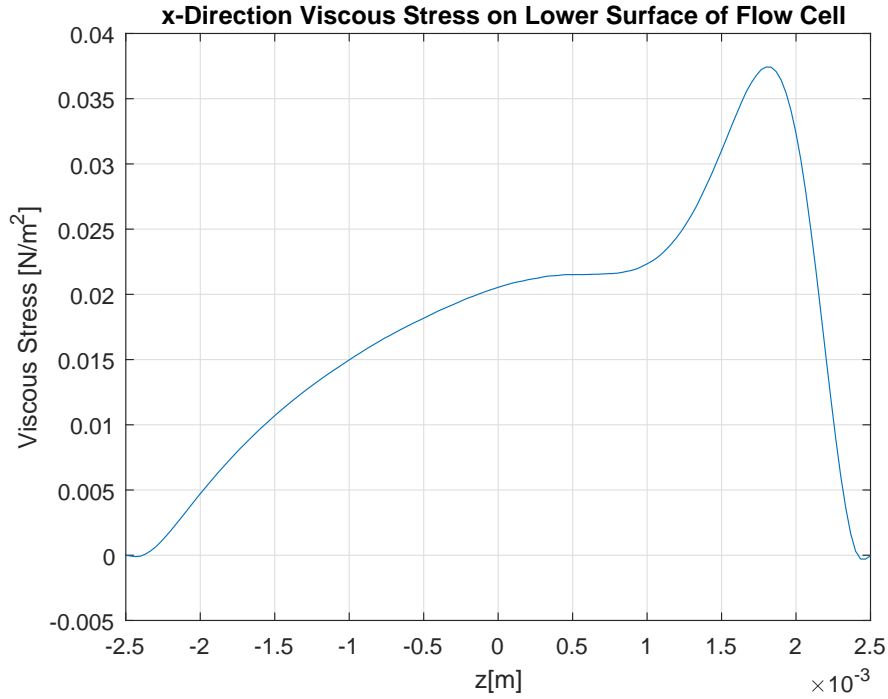


Figure 2.9: Shear stress magnitude across the lower surface of the cell modeled in COMSOL

Equations 2.13 and 2.11 now contain no unknowns and can be solved to produce the velocity profile of the droplet fluid and the surface velocity respectively. As sample calculations, we will assume a droplet viscosity of 1Pas and use the average values for the droplet radius and surface shear of $20\mu m$ and $0.020543Nm^{-2}$ respectively with the resulting figures including the upper and lower bounds defined by the range of droplet radii and shear stresses. Firstly, the velocity profile through the droplet apex is solved for with the result plotted in figure 2.10:

$$\begin{aligned}
 u(z) &= z^2 \left(\frac{3\tau_s}{4\mu h} \right) - z \left(\frac{\tau_s}{2\mu} \right) \\
 u(z) &= z^2 \left(\frac{3 \times (-0.0254)}{4 \times 1 \times (20 \times 10^{-6})} \right) - z \left(\frac{(-0.02054)}{2 \times 1} \right) \\
 \therefore u(z) &= z^2(-770.25) + z(0.0103)
 \end{aligned}$$

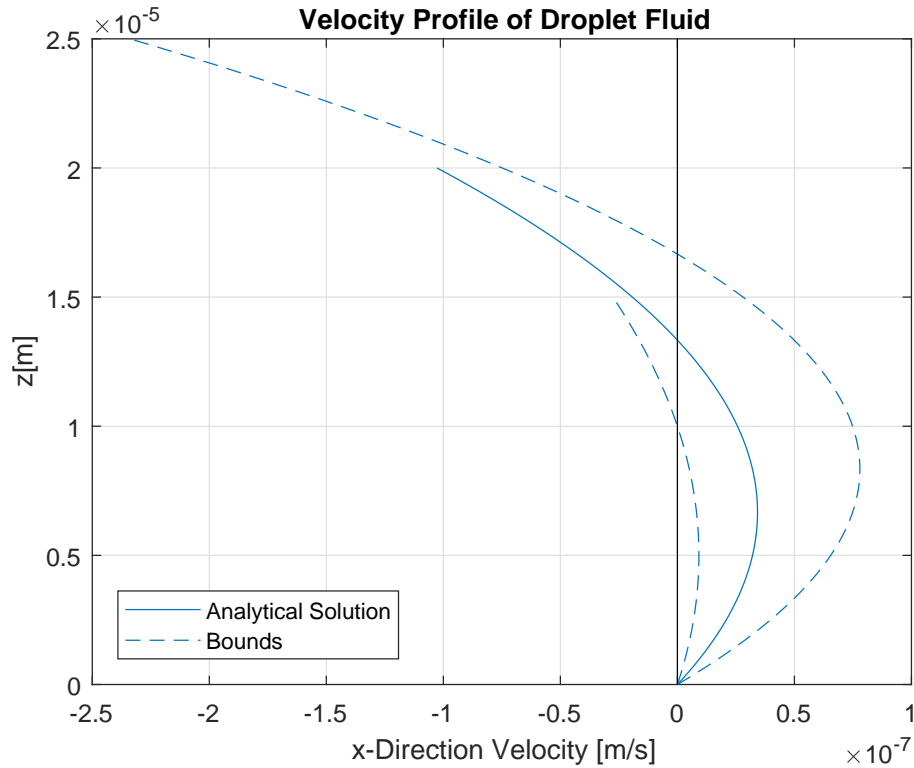


Figure 2.10: 2D Velocity profile through droplet apex

Secondly, we can solve for the free surface velocity :

$$u(z = h) = \frac{\tau_s (\sqrt{R^2 - x^2})}{4\mu}$$

$$\frac{(-0.0254) (\sqrt{(20 \times 10^{-6})^2 - x^2})}{4 \times 1}$$

$$\therefore u(z = h) = (5.135 \times 10^{-3}) (\sqrt{(20 \times 10^{-6})^2 - x^2})$$

The outcome of this analysis relative to the experiment are beads moving with a maximum velocity of 9.11×10^{-8} in the negative x direction, opposite to the direction of the inlet flow. Whilst collecting data from the experiment, beads were not noticed to be moving in the opposite direction to the flow, however it may have been overlooked as the value of interest was the speed of the beads, independent of the direction. The bead speeds will therefore be considered only in magnitude when making comparisons between the analytical solution and the experimental data.

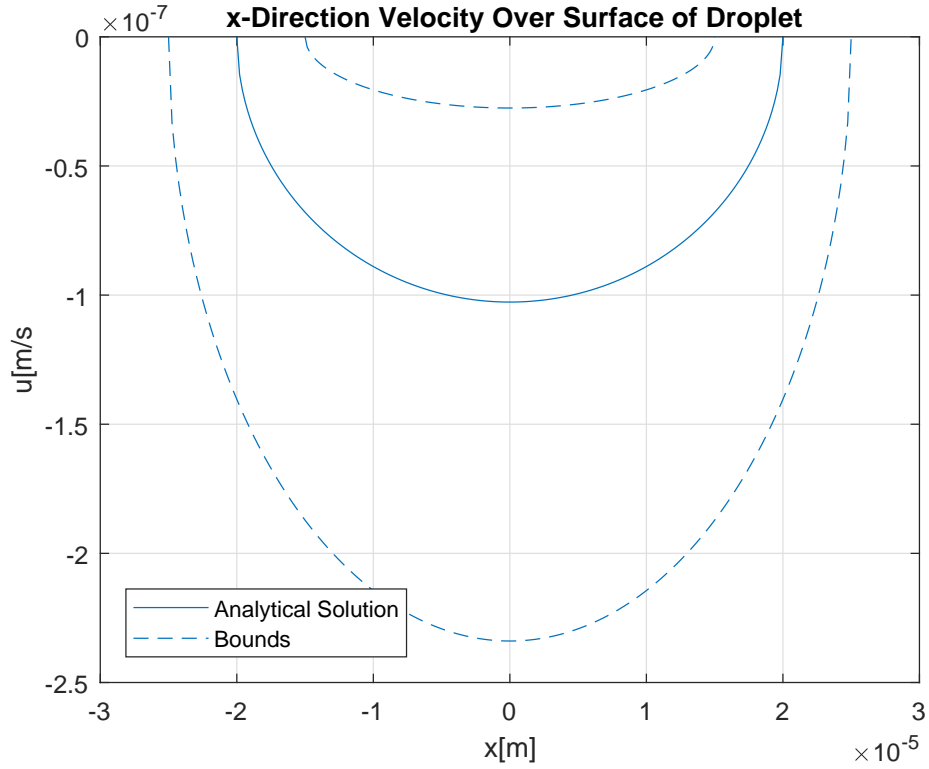


Figure 2.11: 2D surface velocity from the forward to rear stagnation points.

2.5 Comparison to Experimental Data

The bead mobility technique measures the average velocity of beads as they travel across the droplet, as seen from above through the microscope. We do not yet have an analytical solution for the average velocity as it is dependent on experimental techniques. First, we must utilize the data from the particle tracing study performed in section 4.3.5. The particle data was used to form a relationship between the velocity at the droplet apex and the average velocity of a particle, as measured in the bead mobility technique. It was found that the average bead speed can be approximated as 78.0% of the surface apex velocity. This analytical solution for the average bead speed is compared to the data as presented by Renbaum Wolff et al [3, 4] in figure 2.12. The prediction of the average bead speeds made by the model at the upper and lower bounds of each experimental data set is evaluated in table 2.3. The calibration curve constructed by Renbaum Wolff et al [4] was fitted using a single term power law of the form $u = a\mu^b$ where u is the average bead speed, μ

is the droplet viscosity and a and b represent constants. The same function is fitted to the analytical solution with the results presented in table 2.4. The constant 'a' varies by 74.0% whilst the exponent 'b' varies by only 4.71%. The analytical solution is seen to correspond to the data with an error ranging from approximately 60% to 80%, accuracy improving with a decreasing viscosity. The upper bound of the analytical solution improves the discrepancies ranging from -27.0% at $\mu = 10^{-3} \text{ Pas}$ to -63.5% at $\mu = 10^3 \text{ Pas}$, however still under predicts the experimental data.

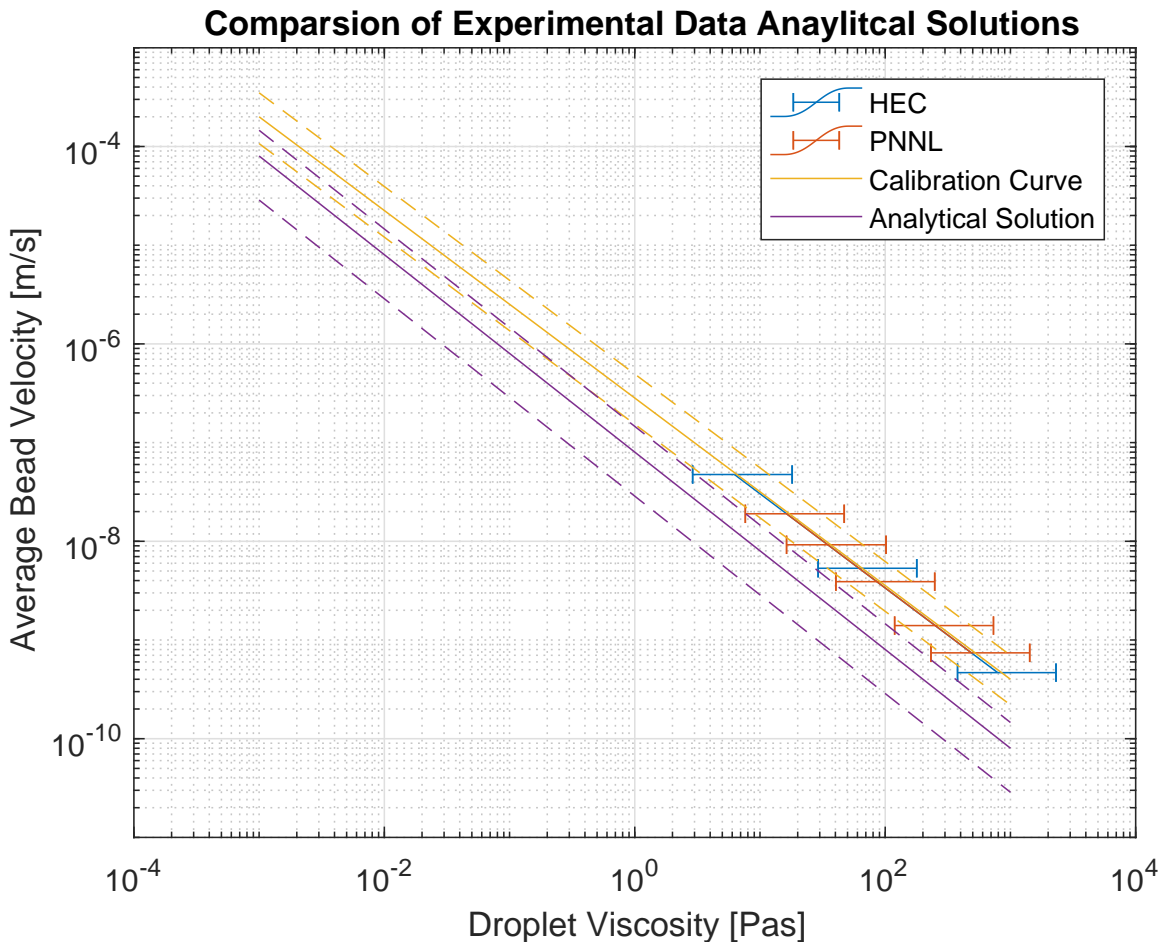


Figure 2.12: Viscosity curves of three experimental results as given by Renbaum-Wolff et al [3] compared to the proposed analytical solution. HEC and PNNL represent data obtained from two separate experiments measuring α -pinene particles. The calibration curve constructed using fluids of known viscosities is also compared to.

Table 2.3: Comparison of average bead speeds between analytical solution and experimental results

Viscosity [Pas]	Analytical Solution	Calibration Curve ³			HEC		PNNL	
		Velocity [ms ⁻¹]	Velocity [ms ⁻¹]	Error [%]	Velocity [ms ⁻¹]	Error [%]	Velocity [ms ⁻¹]	Error [%]
0.001	8.01E-05	2.0E-04	-59.9%	-	-	-	-	-
6.25	1.28E-08	5.0E-08	-74.2%	4.75E-08	-73.0%	-	-	-
16.3	4.91E-09	2.0E-08	-75.4%	1.90E-08	-74.1%	1.90E-08	-74.1%	
488	1.64E-10	7.9E-10	-79.2%	7.40E-10	-77.8%	7.41E-10	-77.8%	
791	1.01E-10	5.0E-10	-79.7%	4.67E-10	-78.3%	-	-	
1000	8.01E-11	4.0E-10	-80.0%	-	-	-	-	

Table 2.4: Comparison of fitted power law function constants between analytical solution and experimental results. Recalling the function to be in the form $u = a\mu^b$

	a	b	R ² Value
Calibration Curve	2.73×10^{-7}	-0.955	0.988
Analytical Solution	7.11×10^{-8}	-1	1
Error	-74.0%	4.71%	-

The reason for the difference in results is not clear, however some possible sources of error are discussed. The analytical methodology is validated by close approximation to the modeling of the droplet flow of section 4 so the error is assumed to be non-systemic. The analytical solution assumes a droplet contact angle of 90°. The range of contact angles of droplets studied ranged from 58° to 95°. The results of section 5 show that the assumed contact angle of 90° should result in higher velocities than the experimental value averaged out over the range of contact angles. The effect of the assumed contact angle is therefore superseded by other factors. It is proposed that the discrepancy may in part be due to the approximation of an average bead speed as 78% of the apex velocity. The method used to obtain this value isolated beads within the droplet model that would theoretically be chosen for calculation, based on current techniques. Currently, there is no systematic method

in place for decided which beads should be measured. A more systematic approach is difficult to impose due to the varied distribution of beads within the droplet. The criteria used to select beads from the model may not have been strict enough to accurately match experimental technique, resulting in a lower measure of average bead speed. The largest contributing factor to the difference between the analytical and experimental results is suspected to be the value of the shear stress taken from the COMSOL model. The flow within the cell is complex making it difficult to model and was therefore only modeled in 2D. The results in a simplified flow that does not take into accounts the flow irregularities discussed in section 2.3. It is believed that this has resulted in an under predicted shear stress.

In addition to the general under prediction of the experimental data, the plot of figure 2.12 shows the analytical solution having a steeper slope than the experimental data, as quantified in table 2.4 as a 4.71% error in the exponent constant. The reason for this discrepancy is believed to be a variation of diffusion time between droplets of different viscosities. As described by Renbaum-Wolff et al [4], a solution containing the tracer particles is sprayed over and allowed to settle into the droplets. However, the calibration curve used droplets in the range $10^{-3} < \mu < 10^3$. Therefore, if the time between the seeding of the droplets and the study of the droplets in the flow cell is the same in each test, droplets of higher viscosity will allow the particles to diffuse to a shallower depth within the droplet. Particles measured in higher viscosity droplets will be closer to the droplet surface, resulting in a higher measured velocity. With reference to figure 2.12, this acts to shift the lower end of the data up, increasing the observed error of the analytical solution at high viscosities.

2.6 Reynolds Number of the Gas Phase

The bead mobility technique forces us to consider two Reynolds numbers. Firstly, that of the gas phase within the domain, and secondly, that of the flow immediately surrounding the droplet. Ordinarily, the Reynolds number within the domain would be expected to govern the flow characteristics. However, in this experiment the scale of the droplet subjected to the flow is many magnitudes smaller than that of the surrounding chamber, as seen in figure 2.2, page 20. This means that

the droplet has little influence on the gas phase and creates only small disturbances, suggesting a lower Reynolds number. The flow dynamics of the flow cell are reasonably complicated making it difficult to accurately define parameters to calculate the Reynolds number. In addition to this, only the flow immediately surrounding the droplet is required to be considered in order to resolve the flow dynamics of the droplet fluid. Therefore, we will calculate the Reynolds number based on a local value for the velocity and using the droplet diameter as the characteristic length. The Reynolds number of the gas flow over the droplet is calculated using the same equation adopted by Renbaum-Wolff et al [4]:

$$Re = \frac{\rho_g V_g d_d}{\mu_g} = \frac{V_g d_d}{\nu_g} \quad (2.14)$$

Where :

- ρ_g is the density of the gas
- V_g is the characteristic gas velocity
- d_d is the diameter of the droplet
- μ_g is the dynamic viscosity of the gas
- ν_g is the kinematic viscosity of the gas

As we are using the diameter of the droplet in our calculation of the Reynolds number, it is necessary to define a local value for velocity as the average velocity through the flow cell in no longer relevant to the small scales being studied. The value for velocity will be calculated as the frictional velocity as defined by the fanning friction factor:

$$f = \frac{\tau_w}{(\frac{1}{2}) \rho_g V_g^2} \quad (2.15)$$

Where :

- f is the fanning friction factor
- τ_w is the average wall shear stress on the lower surface
- ρ_g is the density of the gas
- V_g is a local definition for the gas velocity

As an approximation, we can assume laminar flow in a square channel :

$$f = \frac{14.227}{Re}$$

With the Reynolds number having been defined in equation 2.14 :

$$f = \frac{14.227}{\left(\frac{V_g d_d}{\nu_g}\right)}$$

$$f = \frac{14.227 \nu_g}{V_g d_d} \quad (2.16)$$

Equating equations 2.15 and 2.16, we can solve for the characteristic gas velocity :

$$\frac{14.227 \nu_g}{V_g d_d} = \frac{\tau_w}{\left(\frac{1}{2}\right) \rho_g V_g^2}$$

$$V_g = \frac{\tau_w d_d}{\left(\frac{1}{2}\right) 14.227 \rho_g \nu_g} \quad (2.17)$$

$$V_g = \frac{0.02054 \times (40 \times 10^{-6})}{0.5 \times 14.227 \times 1.1404 \times (15.542 \times 10^{-6})}$$

$$\therefore V_g = 6.516 \times 10^{-3} \text{ ms}^{-1}$$

Substituting back into equation 2.14 :

$$Re = \frac{V_g d_d}{\nu_g}$$

$$= \frac{(6.516 \times 10^{-3})(40 \times 10^{-6})}{(15.542 \times 10^{-6})}$$

$$\therefore Re = 0.0168$$

This is much lower than the Reynolds number calculated by Renbaum Wolff [4] (by a factor of approximately 150) due to the updated value used for the gas velocity. However, this discrepancy is expected to make little difference as the Reynolds number is very low in both cases.

2.7 Bead Motion

The equation for the bead motion can be found by applying Newton's second law:

$$\vec{F} = m \vec{a}$$

Where in the case of the bead, the driving force is the drag force on the bead. The drag force is dependent on the relative motion between the bead and the droplet fluid and on the viscosity of the droplet fluid:

$$\vec{F} = F_{Drag} = \frac{1}{2} C_{Drag} \rho_d (u_d - u_b)^2 A_b \quad (2.18)$$

Where :

- C_{Drag} is the coefficient of drag⁴
- ρ_d is the density of the droplet fluid
- u_d is the velocity of the droplet fluid
- u_b is the velocity of the bead
- A_b is the frontal area of the bead, which for a sphere is equal to :

$$A_b = \frac{\pi d_b^2}{4}$$

On examination of equation 2.18 we can see that if the particle is accelerating, there must be a drag force and therefore a difference between the bead and fluid velocities. Although small, if the bead is accelerating, there will be an error in the reading given by the bead velocity as it will not match that of the fluid. However, equation 2.12 defines the fluid velocity such that it is a maximum at the droplet apex. As this is a maximum, at this point there should be no acceleration experienced by the bead and therefore the bead and fluid velocities should be the same. It seems therefore that it would be most accurate to measure the maximum bead speed

⁴It should be noted that this value does change depending on particle size, shape and the Reynolds number of the fluid. Considering the variations in these quantities with the bead diameter varying only slightly ($930 \pm 50\text{nm}$) and the Reynolds number being minimally affected, we can assume this to be constant.

occurring at the droplet apex rather than the current method of calculating average bead speeds. A measurement of apex velocity may however be difficult to implement due to the droplet fluid velocity being measured based on tracer particles, the locations of which are mostly uncontrollable.

The Stokes number is calculated as the tracer particles within the droplet will only follow the streamlines if the Stokes number is small (lower than 0.1).

$$Stk = \frac{\text{characteristic response time of the fluid}}{\text{characteristic response time of the bead}}$$

$$Stk = \frac{\tau V_g}{d_b} \quad (2.19)$$

Where :

- d_c is the diameter of the beads
- τ is the bead relaxation time, which for a low Reynolds number is defined :

$$\tau = \frac{\rho_b d_b^2}{18\mu_g} \quad (2.20)$$

Where :

- ρ_b is the bead density
- μ_g is the dynamic viscosity of the droplet

As given by Renbaum-Wolff et al [4], the bead diameter is equal to 930nm whilst the bead density is approximated as 1500kgm^{-3} . As a worst case, the droplet viscosity will be assumed to be equal to the most viscous droplet applicable to this technique at 1000Pas . These values can be substituted into equations 2.19 and 2.20:

$$\tau = \frac{1500 \times (930 \times 10^{-9})^2}{18 \times 1000} = 7.21 \times 10^{-14}$$

$$\therefore Stk = \frac{(7.21 \times 10^{-14}) \times 1}{930 \times 10^{-9}} = 7.75 \times 10^{-8} \ll 0.1$$

Therefore, the beads will follow the streamlines with a tracing accuracy error less than 0.1% [63].

CHAPTER 3

Model Development

3.1 Model Details

This research revolves around developing and utilizing a COMSOL model of the bead-mobility technique. As previously discussed, the technique currently suffers from poor accuracy. The aim of the project is to use a COMSOL model to validate the relationship formed by Renbaum-Wolff et al [4] and to investigate how the technique can be adjusted to improve its accuracy. The proposed methodology for the development and use of the COMSOL model is illustrated in figure 3.1. The bead mobility technique uses Nitrogen as the medium flowing over a droplet of varying viscosity. Prior to the creation of the model outlined in this section, considerable time was spent in the attempt to construct a model with the same experimental parameters as in bead mobility technique. The result was a failed model as the flow within the droplet domain was unable to be resolved. This null result prompted the creation of a new model, using parameters not bound by experimental conditions. The aim of this new model is simply to make use of parameters that facilitate flow within the droplet. To achieve this, the model inherited conditions from an earlier model, created in 2D, using a droplet of engine oil in a medium of water. This 'oil and water' model was originally created as an initial model but will now provide guidance for a functioning 3D model. As a result of the modeling achieved with the oil and water model, it is suspected that the timescales used in trying to create a model using nitrogen were not long enough. It is believed that that time taken for the droplet fluid to reach steady state, with the small amount of momentum transfer from the nitrogen phase, was underestimated. Nonetheless, this model provides useful insight into the flow dynamics associated with the bead mobility technique and successfully explores potential sources of error through parametric studies.

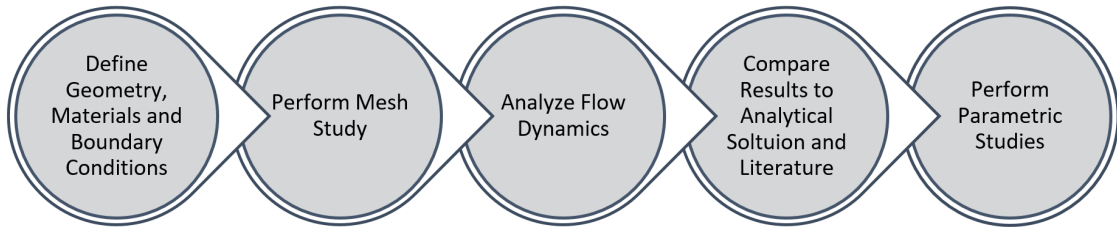


Figure 3.1: COMSOL model design methodology

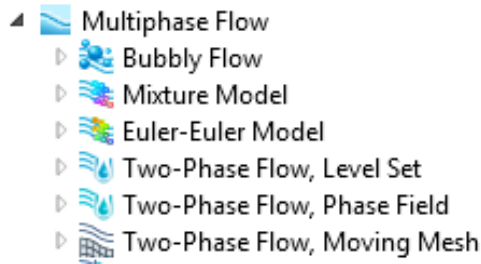


Figure 3.2: COMSOL screenshot of the six different multiphase flow models.

3.1.1 Multiphase Flow Interface

The COMSOL model is required to solve a multiphase flow problem due to the presence of both the droplet and water phases. COMSOL offers six different interfaces that deal with multiphase flow problems which are shown in figure 3.2. Discussed in the following section is the justification for the use of the Moving Mesh, Two Phase Flow interface. Each of the above multiphase flow models fall under one of two categories; disperse methods and interface tracking methods. The first three models of figure 3.2 (bubbly flow, mixture and Euler-Euler) fall under disperse methods whilst interface tracking encompasses the last three models (level set, phase field and moving mesh). Disperse methods are tailored toward larger scale simulations where a large number of droplets or bubbles are being studied. Its computationally inexpensive characteristic is achieved by not explicitly tracking the position of each interface between the fluids (as interface methods do) but instead calculating the volume fraction of each phase. Contrastingly, interface tracking methods model the flow of two phases separated by a clearly defined interface. This method is both accurate and provides a clear picture of the flow field however comes at a high computational cost. This method is therefore best suited to applications with small

domains where only a few droplets (or bubbles) are studied. The interface method is clearly the more applicable to the simulation of the bead mobility technique as only one droplet and interface are being studied [64].

3.1.1.1 Interface Tracking Methods

As stated previously, the interface tracking method encompasses the level set, phase field and moving mesh models. Both the level set and phase field methods track and overlay the interface of the phases on a fixed mesh defined by the geometry. In addition to solving the Navier-Stokes and Continuity equations for momentum and mass respectively, the location of the interface is tracked by solving additional transport equations. The interface that is resolved is fairly diffuse in comparison to that of the moving mesh method as shown in figure 3.3. The difference between the phase field and level set methods are their underlying principles. The phase field method minimizes the mixing energy⁵, a physical consideration, whereas the level set method adopts a more mathematical approach. The result being, if the interface is properly resolved by the mesh, the phase field method is more accurate but as a trade-off is more computationally expensive (as it requires solving two transport equations, one more than level set). Unlike the level set and phase field methods, the moving mesh method produces a clearly defined interface tracked using the Arbitrary Lagrangian-Eulerian (ALE) method. Typically, fluid interfaces are much thinner than domain geometry based meshes, a potential issue with the level set and phase field methods. The moving mesh method however, bypasses this problem by deforming the mesh elements to the shape of the fluid-fluid boundary. The mesh deforms to the contour of the interface so that its position is located at the mesh element boundaries of the two phases. This mesh boundary location characteristic negates the need for any transport equations (required by both level set and phase field). The well-defined interface also means it is possible to accurately solve for different physics in each domain. The drawback of this method is that it cannot be used to solve models that undergo large topological changes [64]. A summary of the three interface tracking methods is given in tables 3.1 and 3.2.

⁵Mixing energy is the sum of the surface and bulk energies of the flow.

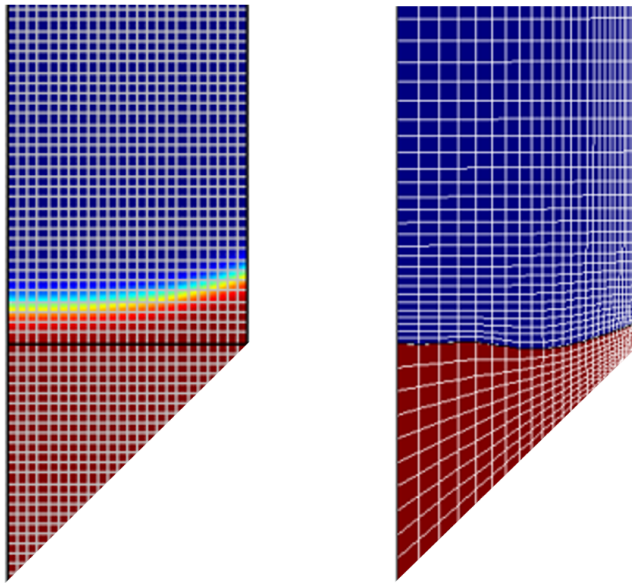


Figure 3.3: Comparison between level set and phase field (left) and moving mesh (right) methods in terms of interface resolution and mesh element configurations.

Table 3.1: Comparison of interface tracking method properties

Property	Level Set	Phase Field	Moving Mesh
Resolution of Phase Interface	good	better	best
Turbulence Models Offered	yes	yes	no
Allows Topological Changes	yes	yes	no

Table 3.2: Comparison of interface tracking methods in terms of equations solved

Equation	Level Set	Phase Field	Moving Mesh
Navier-Stokes	1	1	1
Continuity	1	1	1
Transport	1	2	0
ALE	0	0	1

Regarding the modeling of the bead mobility technique, the moving mesh method is much better suited. The fluid inside the droplet circulates due the shear continuity at the surface of the droplet. In order to accurately model the shear stress transferred from the water phase to the droplet, the interface (i.e. droplet surface) needs to be clearly defined. This alone warrants the use of the moving mesh method as opposed to the level set or phase field. In addition to this, the drawbacks of the moving mesh method are nullified when modelling the bead mobility technique due to its fluid-fluid interface. As discussed above, the moving mesh method is unable to handle large topographical changes of the fluid interface however parameters of the droplet and water phases are chosen so that the surface of the droplet should only deform slightly. The minimal distortion of the droplet will also help to keep the computational cost down as the mesh elements should undergo minimal deformations.

3.1.2 Geometry

This geometry specifies the computational domain studied, representing only the section of the actual domain immediately surrounding the droplet. The geometry of the computational domain was defined as shown in figure 4, with a droplet of oil placed in the center of the lower boundary. The size of the computational domain surrounding the droplet was based on inspection of the water phase streamlines ensuring the boundaries extend past the curved streamlines deforming around the droplet. Similarly, the upstream length was chosen so that the flow was observed to be fully developed by the time it reached the leading edge of the droplet. The positioning of these boundaries was tested by extending all domain boundaries and observing little (0.6%) or no change in velocities of the water phase. The origin was placed at the center of the droplet on the lower boundary using the directional orientations shown in figure 4. This computational domain has been constructed using a simple inspection of the water flow streamlines and briefly checking if extending the domain boundaries affects water flow velocities. The domain has therefore not been optimized for this simulation. It is expected that the dimensions of the domain can be reduced whilst leaving the flow of water around the droplet unchanged. In

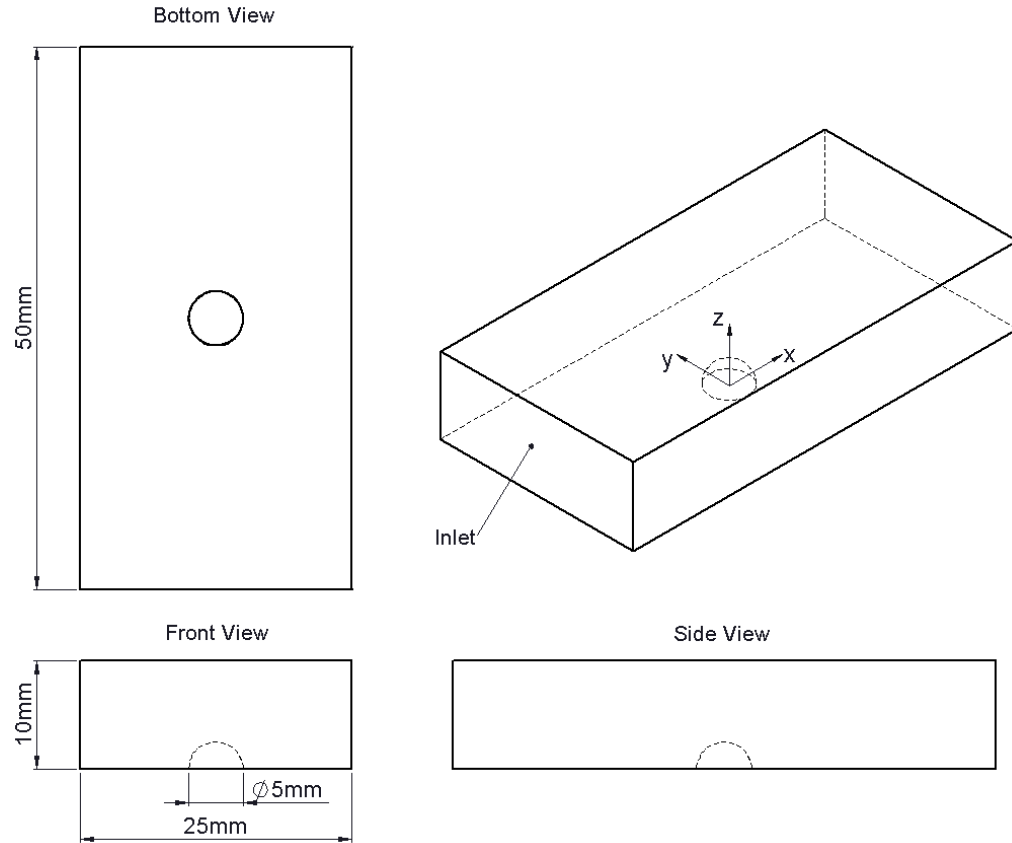


Figure 3.4: Geometry of COMSOL model.

addition to this, the droplet is positioned in the center of the lower surface, at equal distances from both the inlet and outlet boundaries. However, it is likely that a more efficient droplet positioning exists where the droplet is closer to the inlet as the upstream water flow should become fully developed over a shorter distance than the downstream flow which may contain recirculation regions due to the presence of the droplet. It has been decided however, that optimizing the domain will have little influence on the efficiency of the model due to the distribution of mesh elements. As will be discussed in section 3.2, many more mesh elements reside within the droplet domain. Altering the dimensions of the domain only optimizes the water domain which comparatively is responsible for much less computational effort. Therefore, performing parametric studies to determine the most efficient computational domain geometry is deemed unnecessary. The remainder of this investigation will use the domain defined in figure 3.4.

3.1.3 Materials

As discussed previously, this model approximates the bead mobility technique using a droplet of oil in a medium of water. The density viscosity of the oil droplet is set at even values of 1000 and 1 respectively (actual values of engine oil are approximately 900 and 0.3 respectively) with a surface tension equal to that of water. The relevant physical properties of the water and droplet domains are given in tables 3.3 and 3.4.

Table 3.3: Relevant physical properties of Water at 20°C [65]

Property	Symbol	Value	Unit
Density	ρ_{water}	998.23	kgm^{-3}
Dynamic Viscosity	μ_{water}	1.003×10^{-6}	Pas
Kinematic Viscosity	ν_{water}	1.002×10^{-3}	m^2s^{-1}

Table 3.4: Relevant physical properties representing the oil droplet

Property	Symbol	Value	Unit
Density	$\rho_{droplet}$	1000	kgm^{-3}
Dynamic Viscosity	$\mu_{droplet}$	1	Pas
Surface Tension	$\sigma_{droplet}$	70×10^{-3}	Nm^{-1}

3.1.4 Boundary Conditions

In order to set up the model, several boundary conditions need to be defined to instruct the software on what physics are to be applied in relation to governing the fluids behavior. As discussed previously, the computational domain studied is only a section of the actual domain and therefore requires the boundary conditions to be defined accordingly. The inlet and outlet conditions are specified using a zero-pressure condition with suppressed backflow (figure 3.5). The boundaries containing the flow are defined as illustrated in figure 3.6 with the upper surface approximated as a moving wall, the lower surface defined as a no slip wall and the sides as slip walls.

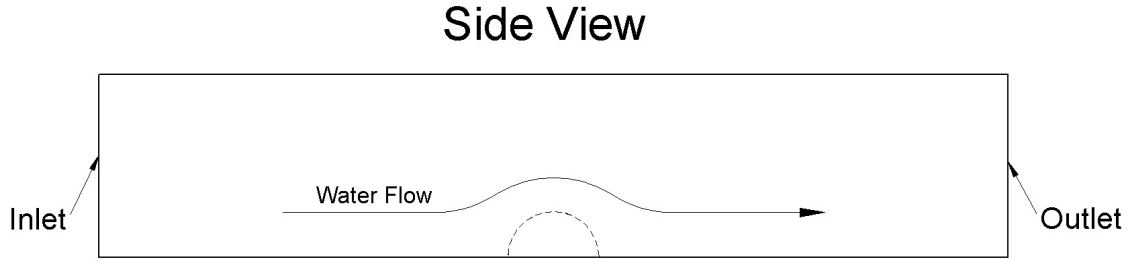


Figure 3.5: Inlet and outlet of domain.

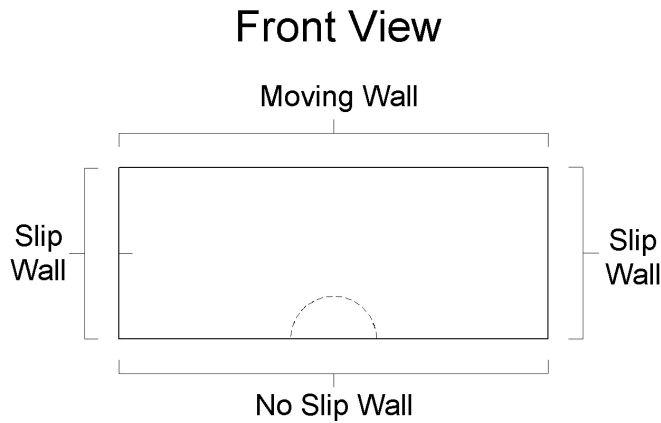


Figure 3.6: Flow containment boundary conditions.

The lower surface represents the actual surface of the flow cell and is therefore defined using the no slip condition. However, unlike the lower surface, the sides of the computational domain do not represent real boundaries but rather define a computational boundary within which the flow is to be studied. Therefore, the sides of the domain only represent partitions in fluid. The flow on either side of each of these pseudo-boundaries is the same and can therefore be defined using a zero-shear slip condition. Contrastingly, the upper surface of the computational domain does not possess the same symmetrical flow properties as the sides. The computational domain lies within the boundary layer of the flow cell present due to the no slip condition of the lower surface. Therefore, a velocity gradient exists in the z-direction across the upper surface of the computational domain. The flows above and below the upper surface differ meaning this boundary must be treated differently. The upper surface is defined using a moving wall condition to approximate the flow of Nitrogen over the droplets seen in the bead mobility technique. As mentioned,

this model uses a medium of water, rather than nitrogen as in the experiment. Although the size of the droplet and the medium in which it is placed has changed, it is important to match the velocity profile of the fluid surrounding the droplet. This ensures that the velocities seen by the droplet as a function of its height are the same as in the experiment. The Blasius Solution defines the approximate boundary layer thickness of a fluid as it moves over a flat plate:

$$\delta \approx 5.0 \sqrt{\frac{\nu x}{u_0}} \quad (3.1)$$

Where :

- δ is the thickness of the boundary layer⁶
- ν is the kinematic viscosity of the fluid
- x is the downstream length from the start of the boundary layer
- u_0 is the freestream velocity

For the purpose of this discussion, we will assume the boundary layers of Nitrogen and water over a flat plate. The kinematic viscosity of nitrogen is approximately 15 times higher than that of water. According to equation 3.1, holding all other factors constant, this results in a Nitrogen having a boundary layer approximately four times larger than that of water. We must define boundary conditions in the model so that the water behaves in the same manner as nitrogen as it approaches the droplet. The model of the flow cell detailed in section 2.3 can be used to evaluate the effectiveness of assuming the upper surface as a moving wall. The moving wall boundary condition places a no slip condition on a wall moving at a specified velocity. A velocity profile was taken from the center of the lower surface of the flow cell, modeled in section 2.3 up to a height of 0.8mm. This height is equal to 4 times that of the average droplet radii (20 μm) studied in the experiment, the same relative height of the computational domain defined in figure 3.4. This velocity profile therefore measures the velocity of the Nitrogen up to a height equal to the height of the computational domain. This velocity profile is used to evaluate the

⁶Defined as the height at which the flow velocity has reached 99% of the freestream velocity.

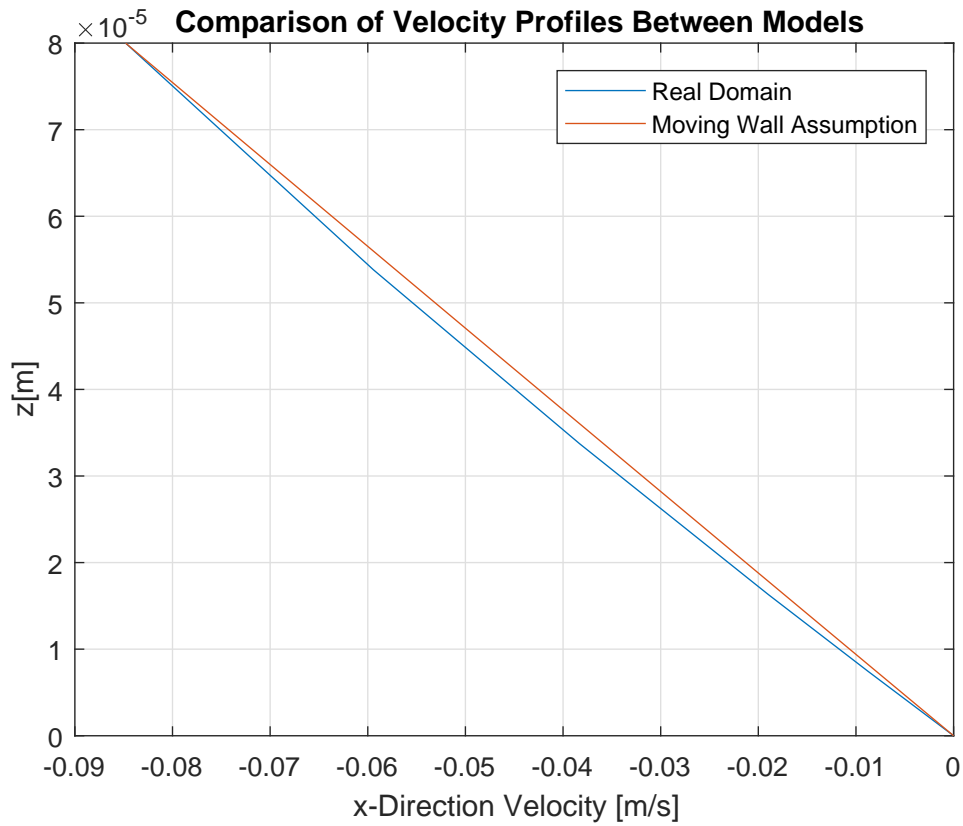


Figure 3.7: Velocity profile comparison between flow cell model and moving wall assumption

effectiveness in approximating the flow of nitrogen over the droplets in the experiment with water in our model. Figure 3.7 shows that if the velocity of the moving wall is set equal to the velocity of the gas phase at the top of the profile, the water phase follows the profile of gas with little deviation. The water profile differs by a maximum of $2.39 \times 10^{-3} \text{ms}^{-1}$, equal to 5.33%, occurring at $z = 0.4\text{mm}$. Placing a moving wall boundary condition on the upper surface of the domain is therefore considered accurate an approximation to the flow of gas over the droplets in the experiment. The moving wall is set at a velocity of 0.5ms^{-1} in the x-direction. This value was taken from the initial 2D model as it was seen to produce adequate shear on the droplet to induce recirculation of the droplet fluid.

3.1.5 Justification of Slip Condition over Symmetry

The sides of the computational domain were defined using slip conditions, rather than symmetry. In the case of modeling viscous flow, symmetry and zero-shear slip wall boundary conditions are essentially the same. Both conditions determine a zero flux across the boundary and no development of a boundary layer [66]. Typically, the symmetry condition is used to divide a flow domain into smaller computational domains along lines of symmetry. For example, flow through a square duct could be modeled as a quarter of the cross sectional area utilizing the two planes of symmetry as in figure 3.8. However, our computational domain is an isolation of the region surrounding the droplet which does not rely on symmetry planes. Although a symmetry boundary condition could have been implemented, a zero shear slip condition was deemed more suited to this application.

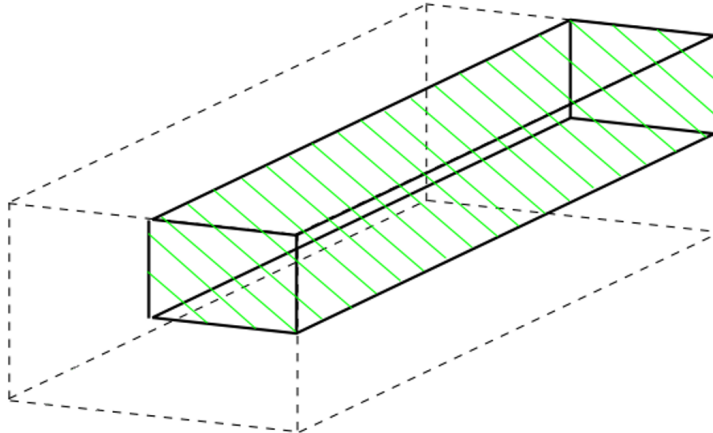


Figure 3.8: Use of symmetry in modelling flow through a duct. Taken from [67]. The white region represents the flow domain whilst the region shaded green represents the reduced computational domain with symmetry conditions on the internal boundaries.

Table 3.5: Time Dependent Solver Settings of the model.

Configuration Node	Solver Setting	Value/Option
General	Time (min, step, max)	(0, 0.1, 15) [seconds]
Absolute Tolerance	Global Method	Unscaled
	Tolerance	0.001
Time Stepping	Method	Generalized Alpha
	Steps Taken by Solver	Free
	Predictor	Linear
	Consistent Initialization	Backward Euler
	Initial Step Fraction	0.001
	Error Estimation	Exclude Algebraic
Fully Coupled	Nonlinear Method	Constant (Newton)
	Damping Factor	1
	Jacobian Update	Every Iteration
	Termination Technique	Tolerance
	Max Number of Iterations	8
	Tolerance Factor	1
Direct	Solver	PARADISO
	Preordering Algorithm	Nested Dissection
	Scheduling Method	Automatic
	Row Pre-ordering	Yes
	Pivoting Perturbation	1E-8

3.2 Mesh Study

A mesh study is to be performed in order to ensure that the results of the simulation are not subjected to errors stemming from the resolution of the mesh. A mesh is considered to be converged when the values of critical result parameters are seen to change less than an acceptable margin with a mesh refinement. Mesh refinement can be achieved by either increasing the order of discretization of the elements or decreasing the size of the elements. Increasing the order of discretization was found to create problems with the surface of the droplet in the form of highly irregular deformations. Therefore, the mesh convergence study was conducted by increasing the mesh density using the $P1 + P1$ discretization scheme. Early modeling efforts gave insight into the general flow characteristics of the model. On observation, it was seen that the water phase flows around the droplet with a region of recirculation forming behind the droplet. The water phase domain should therefore be straightforward to mesh as long as the non-uniform region resulting from flow separation is adequately resolved. It should be noted that the velocity of the droplet fluid was observed to be on the order of $\approx 10^{-4}ms^{-1}$, much slower than the water phase flow of $\approx 0.25ms^{-1}$ and is expected to contain recirculation as seen in experimental results. Therefore, the droplet phase is expected to require a finer mesh than the water phase. This suggests that an even mesh distribution throughout both domains will result in a mesh that is too coarse within the droplet to correctly resolve the flow. To achieve the required mesh distribution, a segregated approach to the mesh study will be conducted. The water and droplet domains will be treated as separate mesh studies to optimize both individually and then combined form a complete solution. Firstly, the water phase will undergo a mesh study whilst keeping the mesh within the droplet constant. Once a sufficient water domain mesh has been decided upon, the same will be conducted in reverse, holding the water domain mesh constant whilst refining the droplet domain until convergence is achieved.

3.2.1 Mesh Configuration

The mesh in the water phase will need to be fine enough to evaluate the region of recirculation downstream of the droplet. In addition to this, the mesh will need to capture the secondary boundary layer formed in the water phase as it passes over the droplet. The finer mesh within the droplet domain can be used to resolve the secondary boundary layer on its surface and the downstream recirculation through the growth rate setting. The growth rate places a limitation on size difference between two adjacent elements. Thus, the growth rate will allow the fine droplet meshing to extend part way into the gas phase. To satisfy the flow considerations, the mesh has been configured using mesh sizing conditions placed on each domain. COMSOL's built in size settings were utilized as they incorporate multiple mesh settings and can be optimized for fluid dynamics. The size settings are therefore defined simply as variations of fine or coarse. Figure 3.9 shows the range of sizing conditions given by COMSOL. The mesh study was carried out by refining the sizing condition of a domain by one increment (for example from 'fine' to 'finer') to create each new configuration.

3.2.2 Mesh Convergence Variables

In order to perform a mesh study, model variables need to be chosen in order to compare the results between meshes. A combination of derived values of points in 3D space, velocity profiles and the drag over the droplet were chosen as variables to quantify the level of convergence of a mesh configuration. A 3D line bounded by the origin and the upper surface of the domain was used to create velocity profiles for both the droplet and the gas phase. This line is used to record the x-direction velocity at each height defined by the mesh nodes. Figure 3.10 shows the location of the 3D line with figure 3.11 showing the velocity profile output. On inspection of the velocity profile, the flow within the droplet is much slower than that of the surrounding gas, represented by the vertical line up to the droplet apex at $z = 2.5\text{mm}$. A continuous line through both domains was used rather than individual lines in each domain as the distortion of the droplet surface due to the flow is currently unknown. The apex of the droplet may not lie at the position

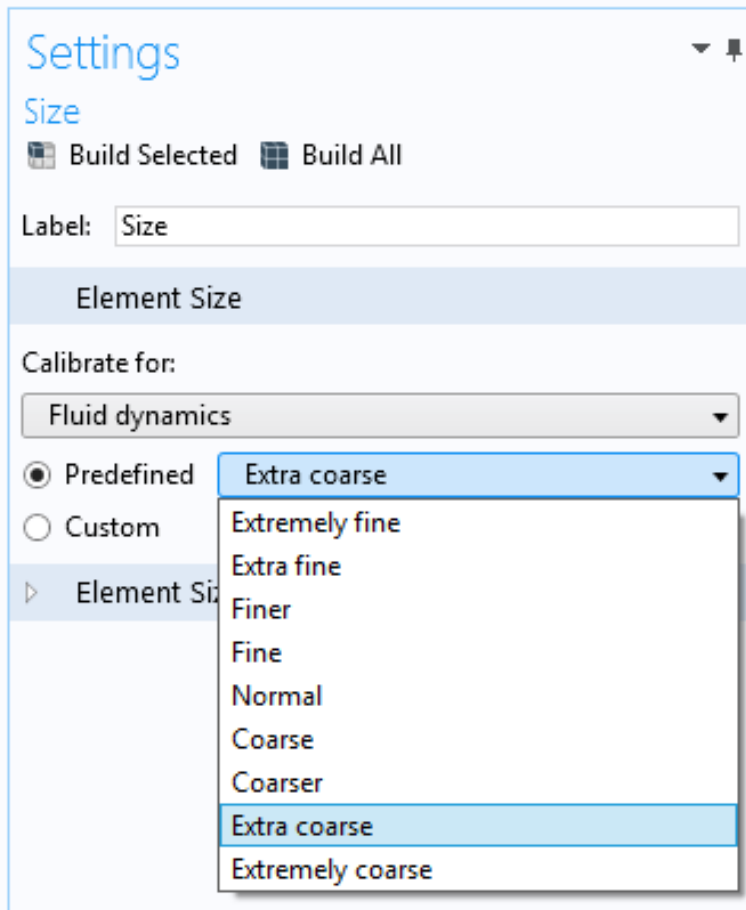


Figure 3.9: Built in COMSOL sizing options used to construct mesh design.

specified by the geometry. Therefore, the velocity profile is recorded continuously through both domains. Post-processing of this data was performed to split the continuous profile into the individual domains. The velocity profile was exported from COMSOL as a value at each node value along the length of the 3D line. The profile data was iterated through using a constant step size and linear interpolation to calculate the velocities for each mesh at each step height. The data was iterated through using a constant 'step' in the z-axis, hence the term 'step method' in the profile error plots. A large increase in gradient from the previous step was seen when the profile reached the water domain, as it exhibits a much higher velocity. This spike in gradient was used to separate the profiles of the two phases.

Convergence within the droplet is also measured using derived values. These

derived values were calculated as the velocity components evaluated at points placed within the droplet domain. For point five points shown in figure 3.12, velocities in the x,y and z directions (u,v,w respectively) were recorded. The position of the six points were chosen to provide insight into the dependence of the mesh on different regions within the droplet. The ' $+Y$ ' and ' $-Y$ ' points probe the smaller areas of recirculation toward the edges of the droplet, perpendicular to the direction of the water flow. Theoretically, these two points should record the same velocities and therefore provide a measure of the flow symmetry within the droplet. The ' $+X$ ', ' $-X$ ' and ' $+Z$ ' points are placed at different locations in the x-z plane to capture the flow at different points in the fluid's recirculation. The velocity at the droplet apex is taken from the velocity profile data measured by the 3D line. Convergence in the gas phase is measured using a single far field point measuring the velocity, and by calculating the velocity profile bounded by the apex of the droplet and the upper surface of the domain.

As the water flows over the droplet, viscous shear stress at the droplet's surface and pressure drag due to the flow separation create drag on the droplet. The stress on the droplet was calculated using the COMSOL '*tpfmm.Tstressx*' command which calculates the shear stress in the x-direction (the direction of flow). The drag force in the x-direction was then calculated through an integration of the shear over the droplet surface using COMSOL's built in commands. By selecting the surface of the droplet, COMSOL calculates the total stress on the surface of the droplet, due to both the droplet and water phases. It is more practical to consider these values separately however the individual effects from each phase were unable to be separated due to COMSOL solving for both phases. Therefore, the drag over the droplet as calculated represents a combined measure of the convergence of both phases. As discussed previously, the formation of the boundary layer of water near the surface of the droplet and the downstream recirculation will be resolved by extension of the mesh within the droplet. These factors are important in calculating the drag of the droplet, therefore the drag variable is measured during the droplet refinement study.

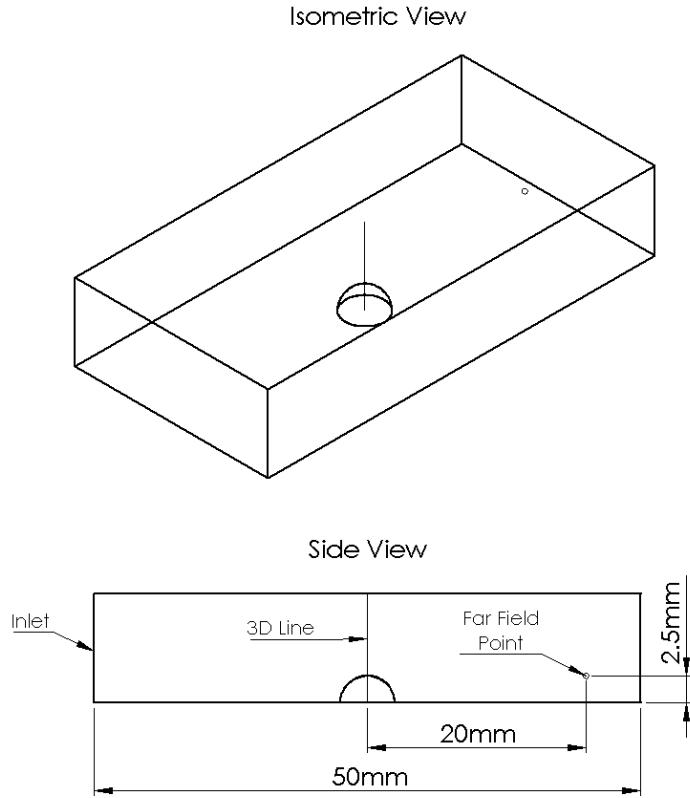


Figure 3.10: 3D line and far field point used to measure convergence of water domain.

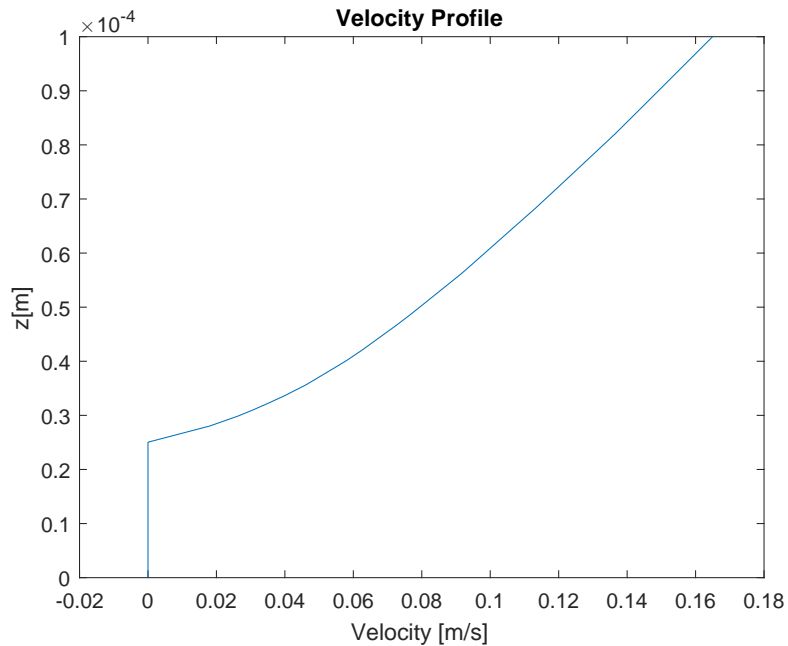


Figure 3.11: Velocity profile of 3D line from lower to upper surface.

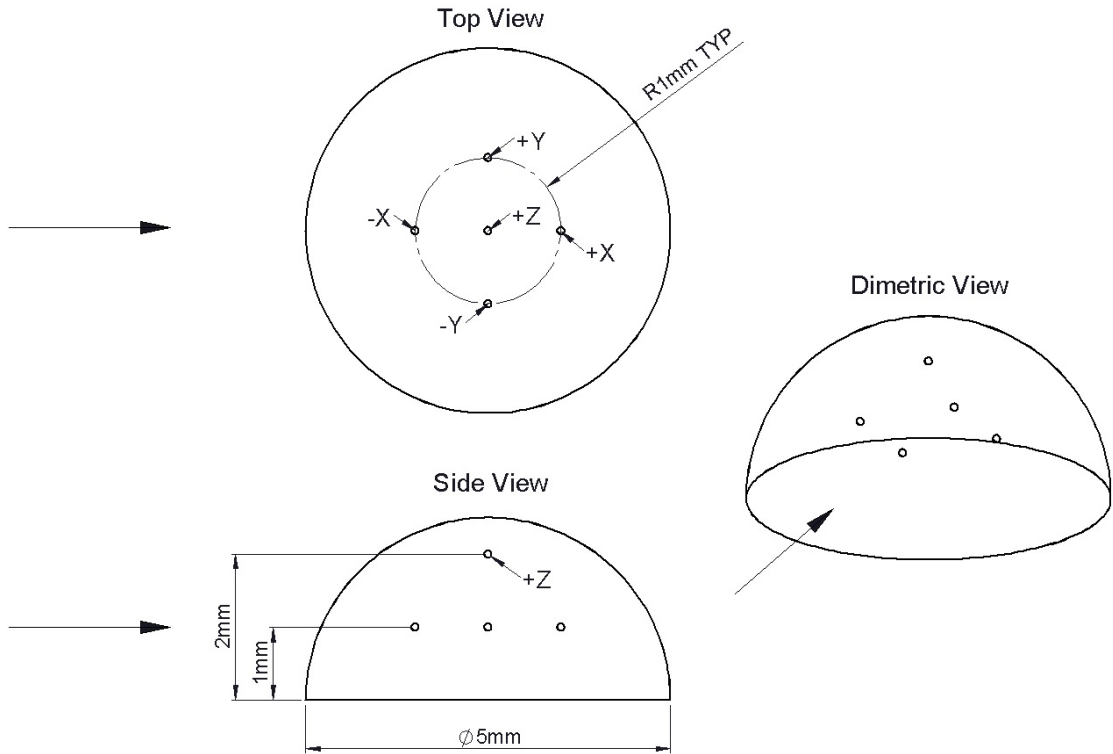


Figure 3.12: Location of points placed within the droplet to measure convergence of droplet domain with arrows indicating flow direction

3.2.3 Water Domain Study

Table 3.6 details the size settings used to define the distribution of elements in the study performed on the water domain. The meshing of the droplet domain is held constant at the 'normal' size setting whilst the water domain is refined from 'extremely coarse' to 'normal'. The resulting study data is given in figure 3.13. Figures 3.14 and 3.15 show the velocity profile of the water domain from the apex of the droplet to the upper surface of the computational domain. All meshes are defined by the same boundary conditions, therefore all profiles are bounded by the apex velocity of the droplet and the velocity of the moving wall. Within this region however, the velocity profiles vary considerably with maximum percentage errors of approximately 40%, 24%, 12% and -9% for meshes 1 through 4 respectively. This is due to the formation of the boundary layer over the surface of the droplet. The extent of this boundary layer causes some disparity between the meshes, as shown by the largest errors occurring near the droplet apex. The main error in the water

Table 3.6: Size setting applied to water domain mesh study

Mesh	Gas Domain	Droplet Domain
1	Extremely coarse	Normal
2	Extra coarse	Normal
3	Coarser	Normal
4	Coarse	Normal
5	Normal	Normal

domain therefore lies in the resolution of the secondary boundary layer around the droplet. This will be resolved in the second part of this mesh study when refining the droplet domain. Due to this reliance on the droplet domain refinement, these velocity profiles and associated errors are a poor measure of the accuracy water domain. Weighting will be placed on the velocity of the far field point to provide evidence of convergence of the water phase independent of the effects of the droplet. The far field velocity point of figure 3.16 is seen to converge steadily toward a stable solution in figure 3.16.

Due to inherent errors present in the water phase velocity profiles, a density of the mesh in the water domain is decided upon inspection of the far field velocity point. The more complex flow nearer the droplet will be resolved by the finer mesh inside the droplet extending into the water domain. Mesh 3 is deemed to produce an acceptable error of 3.69% defining the sizing condition to be placed on the water domain as 'coarser'.

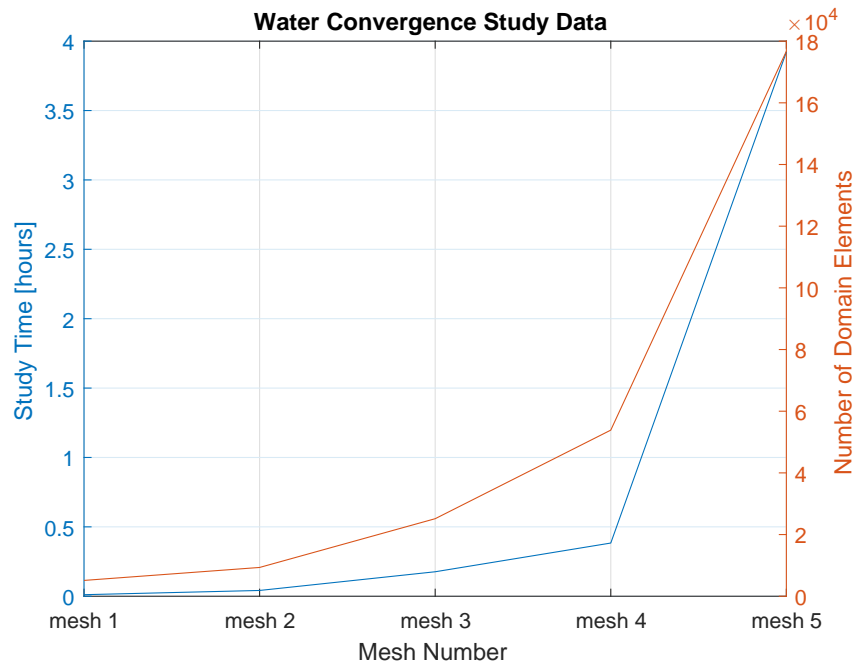


Figure 3.13: Solver time and corresponding number of mesh elements for each mesh configuration

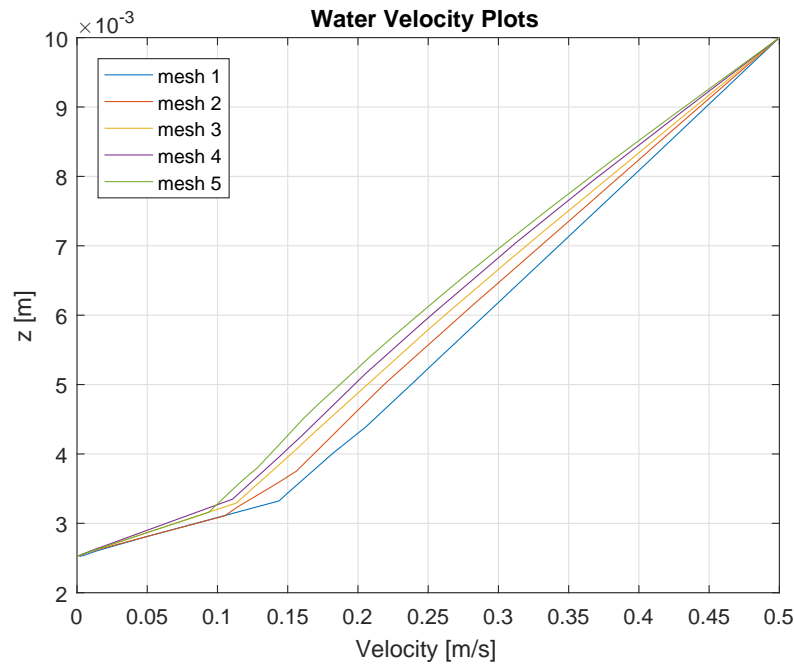


Figure 3.14: Velocity profiles of the water phase bounded by the droplet apex and upper boundary

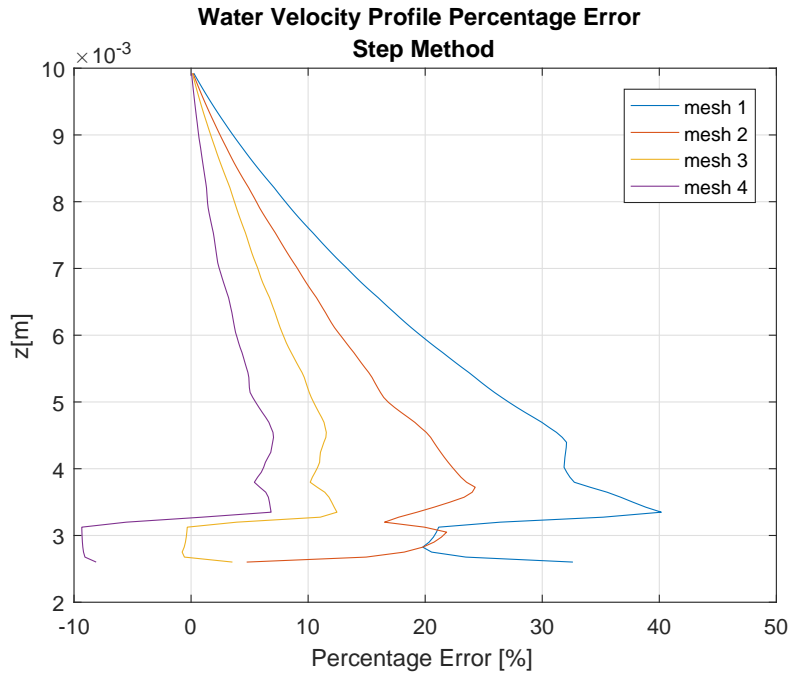


Figure 3.15: Percentage error of velocity profiles relative to the solution given by mesh 5

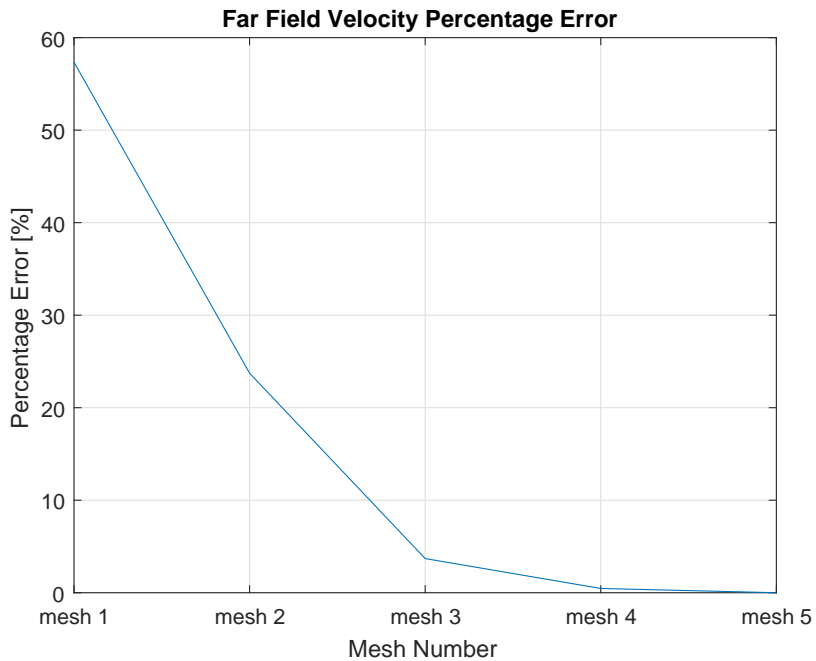


Figure 3.16: Decreasing percentage error exhibited by the far filed velocity point

3.2.4 Droplet Domain Study

Similarly to the water convergence study, the water domain is held at the previously determined size setting 'coarser' whilst the droplet domain is refined from 'finer' to a custom value. The predefined mesh settings provided by COMSOL do not provide a high enough resolution to complete the desired mesh study, so a custom mesh was defined by specifying a maximum element size, details of which can be found in appendix A2. The growth rate was kept reasonably high at 1.09 due to the presence of the thick boundary layer in the water domain as it passes over the droplet. This growth rate allows the finer mesh from inside the droplet domain to extend well into the water domain, ensuring all flow irregularities around the droplet are well resolved. The minimum element size, curvature factor and resolution were unchanged from the extremely fine setting. Similarly to the previous study, the water domain is held at the size setting previously determined whilst the droplet domain is refined. The droplet velocity profiles exhibit shapes which agree with the theoretical solution obtained in section 2. They are also seen to converge steadily with the two finest meshes agreeing reasonably well, varying by a maximum percentage error of 11.5% at the location of maximum negative velocity. Figure 3.19 plots the absolute error of each profile relative to the finest mesh. The relative error has been used instead of the preferred percentage error as the relative error spikes when the profiles cross over the zero velocity line as seen in appendix A2. Similarly to the velocity plots of the water domain, these plots are valuable in showing the features of the flow and checking for reasonable flow patterns, however points are relied on for a quantitative measurement of the convergence error.

Due to the systemic errors present in calculating the percentage errors of the droplet velocity profiles, a suitable mesh is based on the velocities at discrete points and the droplet drag. Figures 3.20 and 3.21 show the convergence of the velocities at the droplet apex and at the points within the droplet domain respectively. All points are seen to converge monotonically and at similar rates, dropping to errors between 9.3% and 13.8% by the third mesh configuration. As the location of the '+Y' and '-Y' points are symmetrical about the x-z plane through the droplet apex (see figure 3.12), they should theoretically record the same velocities. These

Table 3.7: Size setting applied to droplet domain mesh study

Mesh	Gas Domain	Droplet Domain
1	Coarser	Fine
2	Coarser	Finer
3	Coarser	Extra Fine
4	Coarser	Extremely Fine
5	Coarser	Custom

two points provide a measure of flow symmetry within the droplet. The difference in velocities between these two points has dropped to 4.51% by mesh 3, defining a fairly symmetrical flow regime. The droplet drag is also seen to converge in a stable manner in figure 3.22, converging toward a final value of $9.894 \times 10^{-4}N$.

It was decided that the third mesh configuration, producing a drag error of -1.95%, a maximum measured velocity error of 13.8% and a velocity symmetry error of 4.51%, produces a model that is within acceptable tolerance. With velocity being a key parameter for the study of this model, an error of 13.8% within the points studied is not insignificant. It must be judged however, based on the computational cost of improving the result. The solver time increases from 9 to 40 hours from mesh 3 to mesh 4 as seen in figure 3.17. This large increase in solver time was deemed too large a compromise in exchange for the increased accuracy. A study time of 40 hours renders the model impractical for analysis, particularly when considering parametric studies.

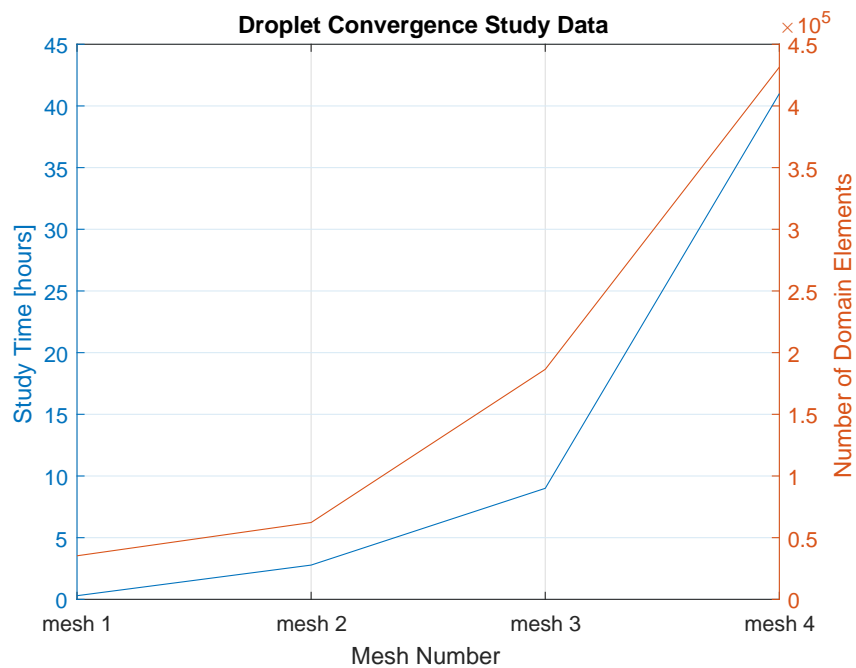


Figure 3.17: Solver time and corresponding number of mesh elements for each mesh configuration

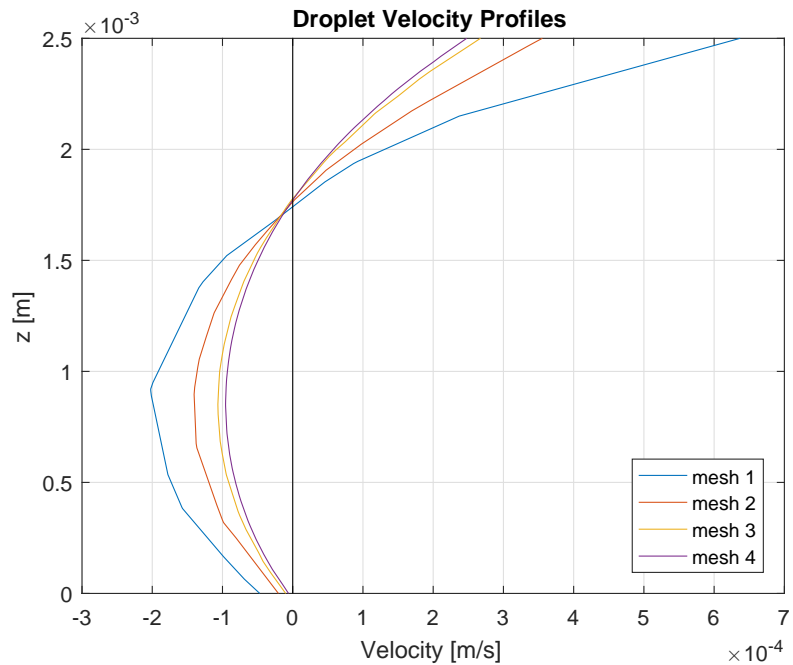


Figure 3.18: Velocity profiles of the droplet phase bounded by the lower surface and the droplet apex

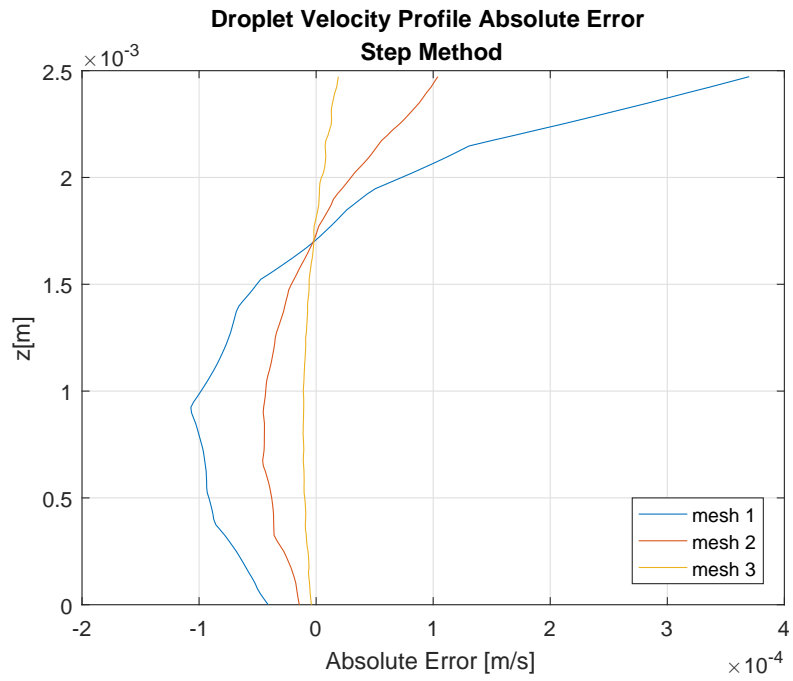


Figure 3.19: Absolute error of velocity profiles relative to the solution given by mesh 4

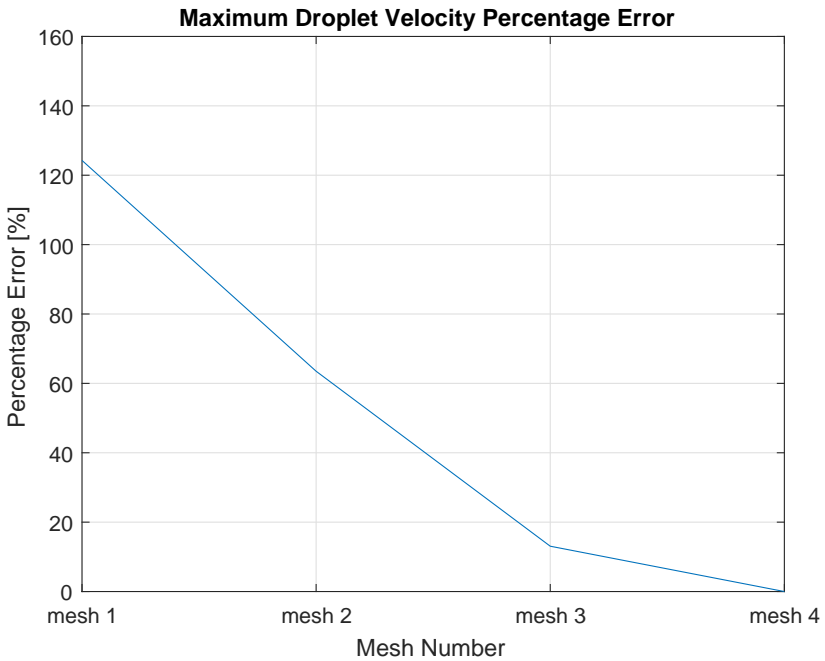


Figure 3.20: Decreasing percentage error of the velocity recorded at the droplet apex, taken as the last value of each droplet velocity profile

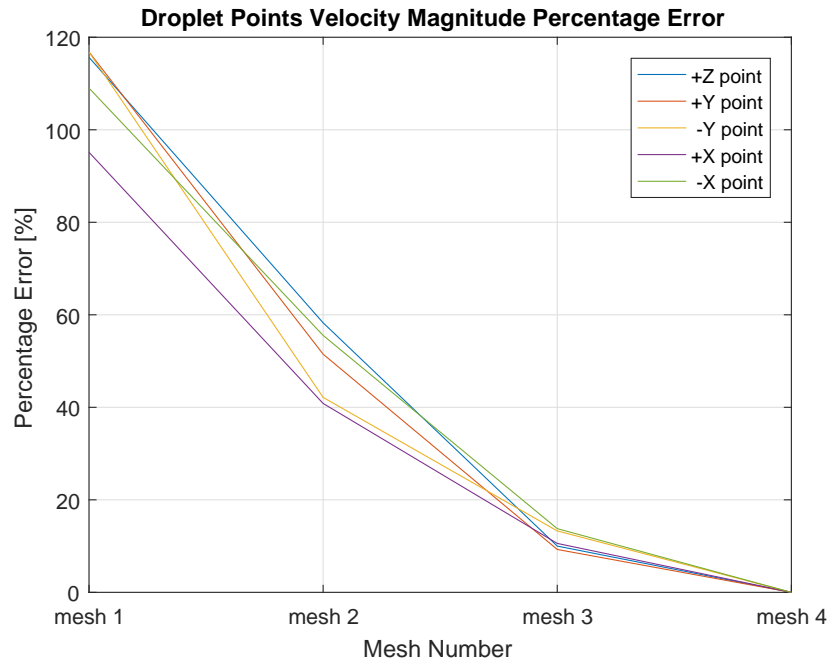


Figure 3.21: Percentage error of all droplet points decreasing at a similar rate.

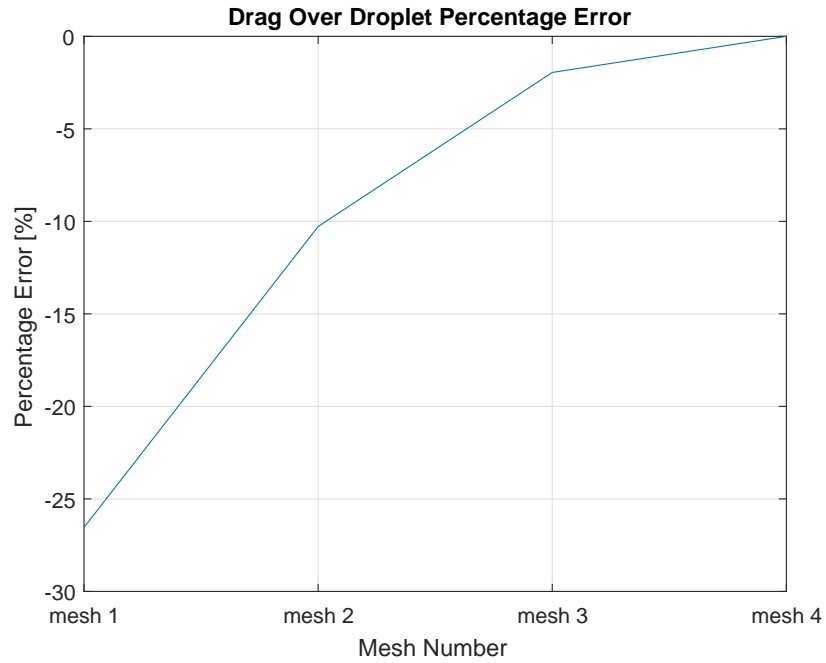


Figure 3.22: Percentage error of drag on the droplet is seen to increase toward a stable value

CHAPTER 4

Flow Analysis

4.1 Analytical Solution

The outcome of his model can first be used to calculate the analytical solution corresponding to the parameters used in the model, recalling the relevant properties of the water phase given in table 4.1. As in section 2, the shear stress over the droplet is assumed to be constant and equal to that at the lower boundary. The shear stress on the lower boundary was found to be a constant value of $0.5891 Nm^{-2}$ up to the forward stagnation point of the droplet. The value of the shear stress over the surface of the droplet was unable to be calculated due to its dependency on the movement of both phases, as discussed in section 3.2. The same methodology as detailed in section 2 can be used to calculate an analytical solution for the Reynolds number of the water phase immediately surrounding the droplet based on the wall shear stress. The droplet velocity profile and surface velocities are also calculated and are presented within the body of this section.

Table 4.1: Relevant physical properties of Water at 20°C [65]

Property	Symbol	Value	Unit
Density	ρ_w	998.23	kgm^{-3}
Dynamic Viscosity	μ_w	1.003×10^{-6}	Pas
Kinematic Viscosity	ν_w	1.002×10^{-3}	$m^2 s^{-1}$

Shear Stress :

$$\tau_s = \tau_w = 0.5891 Nm^{-1}$$

Frictional Velocity :

$$\begin{aligned}
 V_w &= \frac{\tau_w d_d}{\left(\frac{1}{2}\right) 14.227 \rho_w \nu_w} \\
 &= \frac{0.5891 \times 0.005}{0.5 \times 14.227 \times 998.23 \times (1.003 \times 10^{-6})} \\
 \therefore V_w &= 0.414 ms^{-1}
 \end{aligned}$$

Reynolds Number :

$$Re = \frac{V_w d_d}{\nu_w}$$

$$\frac{0.414 \times 0.005}{(1.003 \times 10^{-6})}$$

$$\therefore Re = 2062$$

4.2 Water Domain

As the motion of the droplet fluid is many times slower than that of the water phase, the flow of water over the droplet can be compared as a reasonable approximation to that of a solid sphere. Further simplifying the problem, we can analyze the data in 2 dimensions on an x-z plane through the center of the droplet and assume the droplet to be a half cylinder. According to Schlichting [68], a Reynolds number of 2062 places the flow within the subcritical regime for flow around a cylinder. This defines laminar incident flow with vortex street instabilities forming as a result of the droplet's presence. The drag coefficient of the subcritical regime is quoted as approximately 1.2, however as discussed in section 3.2, the viscous effects of the droplet and water phases were unable to be separated disallowing a value for the drag coefficient to be calculated. However, Schlichting does provide an approximate flow separation angle for this regime of 80° , a comparison to which will be made in this section. Briefly, the mechanism of flow separation will be explained assuming symmetric flow over a circular cylinder as presented by Schlichting with reference to figure 4.1. The condition for flow separation of viscous flow past a cylinder is when the wall shear stress is equal to zero, mathematically:

$$\tau_w = \mu \left(\frac{\delta V}{\delta r} \right) = 0 \quad (4.1)$$

Where :

- τ_w is the shear stress at the surface of the cylinders
- μ is the dynamic viscosity of the fluid
- V is the velocity of the fluid tangential to the surface of the cylinder
- r is the radial distance from the surface of the cylinder

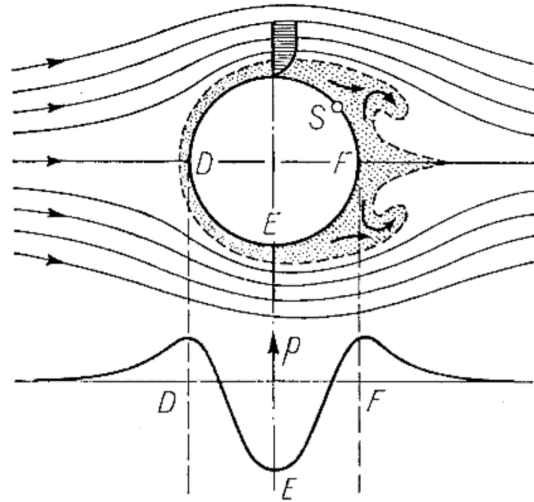


Figure 4.1: Flow shape and pressure plot of viscous flow over cylinder resulting in a recirculation region with point S designating the point of separation. Taken from [68].

This zero-wall shear condition can be explained through Bernoulli's theorem and the subsequent creation of an adverse pressure gradient. With reference to figure 4.1, the highest pressure exists at points D and F representing the forward and rear stagnation points respectively. The streamlines of the incident flow are curved as it moves around the surface. The flow accelerates to a maximum velocity at the apex of the cylinder to balance the centripetal forces caused by the curved streamlines. By applying Bernoulli's theorem, this results in a decrease in pressure from point D to point E. The reverse process occurs over the back of the cylinder from point E to point F causing the pressure to increase from point E to point F. A very thin frictional boundary layer exists very close to the surface of the cylinder. This is a region where the frictional forces caused by the no slip condition of the wall dominate the inertia forces resulting in very slow-moving laminar flow. A particle within this region does not possess enough kinetic energy to overcome the adverse pressure gradient that exists when moving from point E to point F. Therefore, the particle will eventually be stopped by the unfavorable pressure gradient. Particles further toward point E than the location of this stationary particle are pushed by the pressure gradient toward the front of the droplet and are therefore involved in back-flow. This causes a thickening of the boundary layer resulting in boundary

layer mass being transported away from the surface of the cylinder, designating the point of boundary layer separation.

The pressure distribution of the water phase over the surface of the droplet is presented in figures 4.2 and 4.3. The data of figure 4.3 was obtained by placing a series of points very close to the surface of the droplet (the same points as the r_1 curve used to calculate the motion of the viscous sublayer on page 70). The range of the surface plot in figure 4.2 showing the pressure distribution was manually adjusted to include only the pressure of the water phase. The highest pressure is seen to occur at an angle of 43.7° from the forward stagnation point. This differs from the

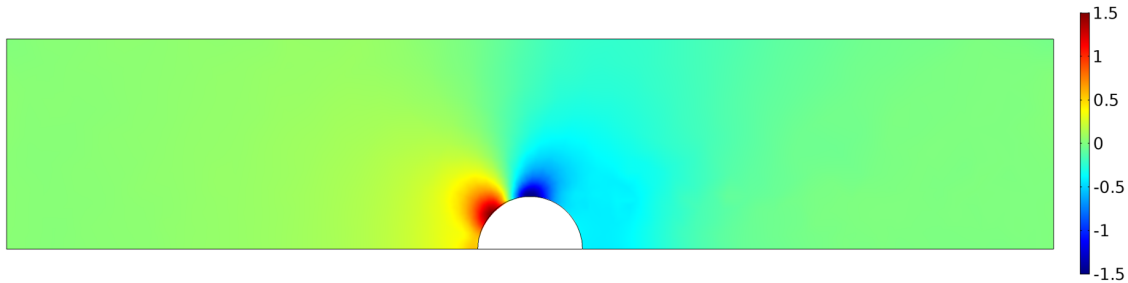


Figure 4.2: Surface pressure plot [Pa] of the water phase in the x-z plane

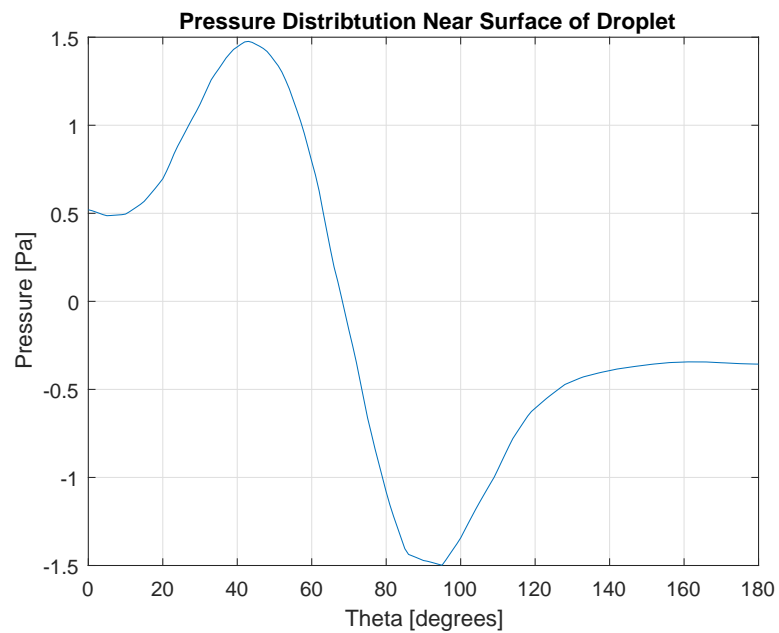


Figure 4.3: Distribution of water phase pressure close to droplet surface from the forward to rear stagnation point

symmetric flow around a cylinder due to the presence of the recirculation region at the front of the droplet (as can be seen in figure 4.6, page 73). The mainstream flow is diverted around this region of recirculation and only impacts the droplet surface further towards the droplet apex. In addition to this, the pressure distribution is not symmetrical about 90° as is presented by Schlichting. The pressure distribution of Schlichting is relevant to a lower Reynolds number as designated by the difference in streamlines between figure 4.1 and figure 4.6 on page 73. The region of flow behind Schlichting's cylinder is involved in flow recirculation, contrastingly, the flow behind the droplet is a region of unsteady flow. This unsteady flow is highly irregular and imposes less pressure on the surface of the droplet than more regular recirculation present in the flow over the cylinder.

We can locate the point of separation in the COMSOL model by applying equation 4.1. The velocity profile of the viscous sublayer perpendicular to the surface of the droplet can be closely approximated using two sets of points close to the surface of the droplet. The deformed radius of the droplet (R_{deform}) was used to create two sets of points very close to the surface of the droplet at radii denoted r_1 and r_2 . These points make up discretized curves positioned within the viscous boundary layer over the droplet.

$$r_1 = R_{deform} + (1 \times 10^{-12})$$

$$r_2 = R_{deform} + (2 \times 10^{-12})$$

Velocity vectors at each point in curves r_1 and r_2 were created by calculating the velocity components in the x and z directions (u and w respectively). Recalling equation 4.1, the separation point occurs when the velocity gradient perpendicular to the surface of the droplet is equal to zero. Therefore, the vectors from curves r_1 and r_2 are subtracted to approximate the value of the incremental change in velocity (δV). The value of δV is assumed to be equal to the change in velocities between curves r_1 and r_2 , with u_1 and w_1 representing the x and z direction velocity components of curve r_1 and u_2 and w_2 representing the x and z direction velocity components of curve r_2 .

$$\delta V \approx \Delta V$$

$$\Delta V = \begin{bmatrix} \Delta u \\ \Delta w \end{bmatrix} = \begin{bmatrix} u_2 - u_1 \\ w_2 - w_1 \end{bmatrix}$$

The component of these vectors acting tangential to the surface of the droplet was found by defining the surface of the droplet using a polar coordinate system. The definition of the angle θ remains the angle from the forward stagnation point. The directional vector representing the tangent to the surface is defined as:

$$e_\theta = \sin\theta i + \cos\theta j = \begin{bmatrix} \sin\theta \\ \cos\theta \end{bmatrix}$$

This directional vector can then be used to calculate the velocity component tangential to the surface of the droplet using a dot product, with subscript T denoting the tangential component:

$$\Delta V_T = \Delta V \cdot e_\theta$$

The tangential velocity at this distance from the surface of the droplet is assumed to be a representative value for the motion of the viscous sublayer over the droplet. The resulting curve of this data manipulation is shown in figure 4.4 and is seen to agree visually with the streamlines of the water phase shown in figure 4.6. Up to an angle of $\approx 20^\circ$ the flow near the surface is moving against the mainstream flow due to the region of recirculation at the front of the droplet (seen in figure 4.6). The viscous sublayer increases in momentum from $\approx 20^\circ$ up to $\approx 84^\circ$ as this section of the surface is exposed to the mainstream flow. The tangential velocity close to the surface is then seen to decrease sharply to $\approx 10^{-14} ms^{-1}$ which continues to the rear stagnation point. This region of very slow moving flow represents the section of the surface exposed to the unsteady flow resulting from the flow separation. The separation point is therefore defined by the location of very slow flow at this sharp change in the motion of the viscous sublayer, equal to an angle of 90.6° from the forward stagnation point. This value coincides with the velocity field and streamline

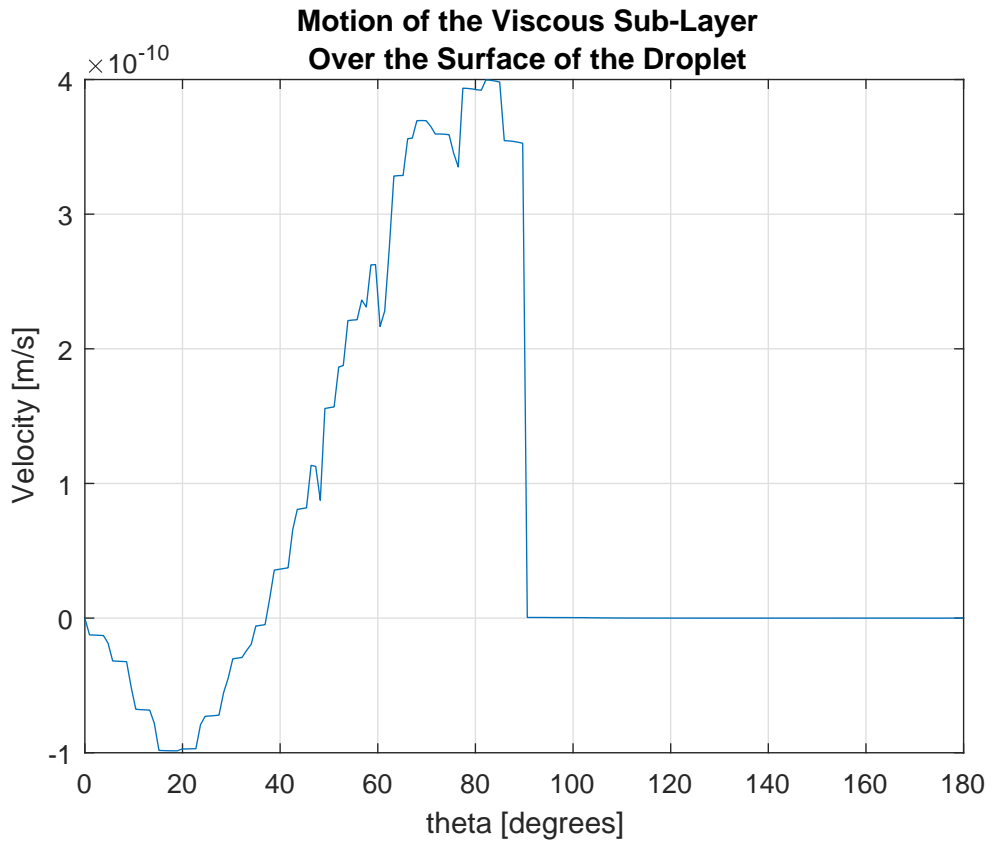


Figure 4.4: Tangential velocity of the water phase very close to the surface of the droplet used as a representation of the motion of the viscous sublayer over the droplet. The point of zero velocity occurring at 90.6 degrees represents the location of flow separation, measured from the forward stagnation point.

plots of figures 4.5 and 4.6, however is larger than the approximate value of 80° predicted by Schlitchling. It is proposed that the reason for this discrepancy is due to the fluid-fluid interface between the water and the droplet differing from the solid-fluid interface of flow over a cylinder. The droplet does not apply a no slip condition at the droplet surface, but rather a slip wall governed by shear continuity between the two phases. This provides the viscous sublayer with more momentum with which the particles travel further over the surface against the adverse pressure gradient thus resulting in a higher angle of flow separation.

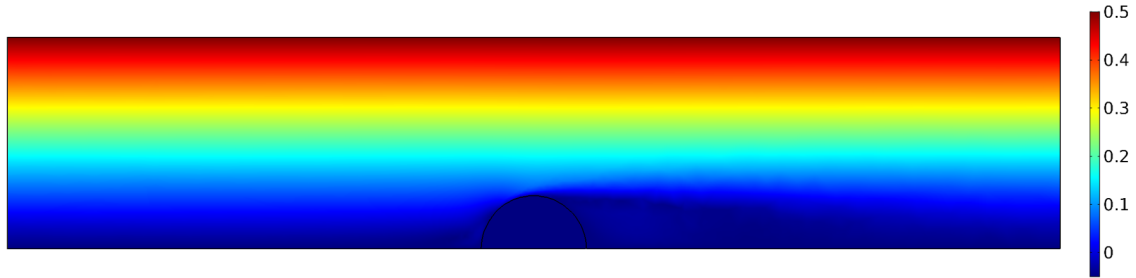


Figure 4.5: Surface x-direction velocity plot [ms^{-1}] in the x-z plane.

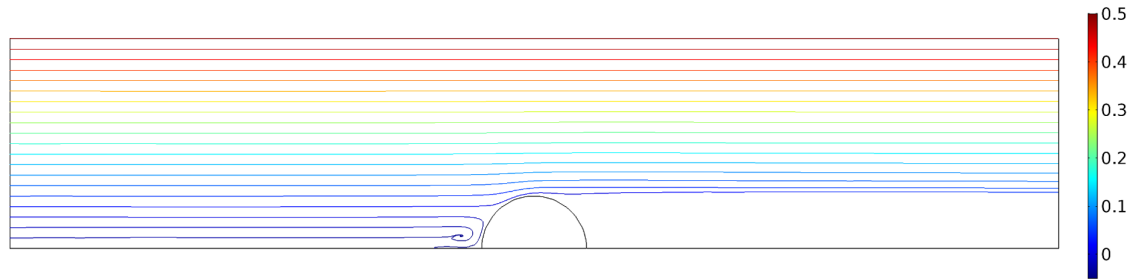


Figure 4.6: Water phase streamlines [ms^{-1}] over surface of droplet.

4.3 Droplet Domain

The driving force of the motion of the droplet fluid is the transfer of momentum from the water phase as it moves over the droplet. As discussed in section 4.2, the relatively high Reynolds number of 2062 of the water phase causes the flow to separate at an angle of $\approx 90^\circ$ from the forward stagnation point. This results in the driving force of the droplet fluid motion acting only up to the droplet apex. Past this, the water close to the surface of the droplet is moving very slowly ($\approx 10^{-14}\text{ms}^{-1}$), causing the droplet fluid to slow. The water phase also exhibits recirculation at the front of the droplet, acting to slow the motion of the droplet fluid in this region. Thus, the fluid accelerates up to a maximum velocity of $3.4 \times 10^{-4}\text{ms}^{-1}$ at angle of 76.2° from the forward stagnation point as illustrated in figure 4.7 and then decelerates as it continues toward the back of the droplet. The extent of this acceleration and deceleration can be seen in the distribution of tangential velocity over the surface of the droplet shown in figures 4.10 and 4.11 on pages 76 and 77. As expected, the location of minimum and maximum pressures at the surface of the droplet coincide with that of water phase seen in figure 4.3.

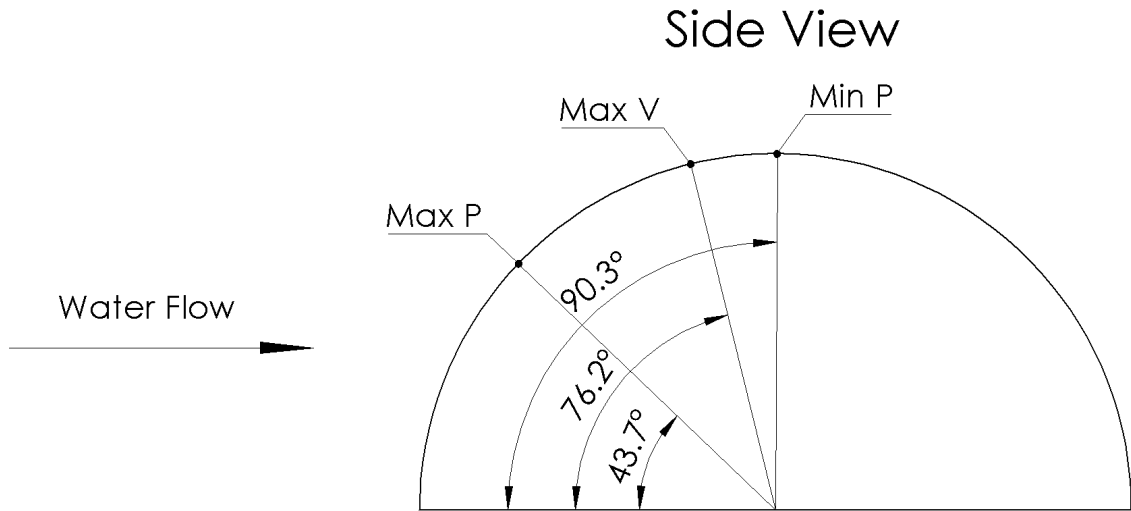


Figure 4.7: Locations of the maximum pressure and velocity and minimum pressure due to the incident water flow

The droplet fluid is contained by its surface and the lower boundary resulting in circulating flow. The flow moves in the positive x-direction (from the front to the rear of the droplet) near the surface as momentum is being transferred through the surface from the water phase. The flow then reaches the back of the droplet and is forced to circulate back towards the front near the lower boundary. The circulating behavior creates a vortex within the droplet as seen in the streamlines of figure 4.8. On inspection of figure 4.8 it can be seen that the location of the stagnation point of the primary vortex lies closest to the boundary exhibiting the highest velocity. This can be explained using the conservation of mass theory. If a line is drawn from the stagnation point to any point on the surfaces bounding the droplet, there is a specified mass flux passing through that line. This mass flux must be equal to the mass flux passing through any other line joining the stagnation point and a boundary due to the incompressibility of the flow and applying the conservation of mass. The flow at an angle of 76.2 degrees from the forward stagnation point has the highest velocity. Therefore, the shortest perpendicular distance between the center of the vortex and the boundary occurs at this location as a shorter distance is required to produce the same mass flux as any other line joining the center of the vortex and a boundary. Using the same reasoning, the lower right corner of

the droplet contains the lowest velocity flow and therefore requires a longer line to match the mass flux. Therefore, the vortex lies closer to a boundary with a higher velocity, resulting in the non-central location of the vortex stagnation point and the asymmetrical distribution of streamlines in figure 4.8.

4.3.1 Literature Comparison

The most relevant literature comparison to the droplet fluid motion found was a numerical study performed by Le Clair et al [69]. Le Clair studied the circulation inside water drops falling at terminal velocity through air. The maximum Reynolds number of the air flow in the study was 300, approximately one seventh of the Reynolds number in the COMSOL model, however the results still provide some level of comparison. The location of the stagnation point in Le Clair's droplet is more central in due to the increased symmetry of the flow over the droplet, defined by the Reynolds number. In addition to this, the lower boundary of the COMSOL model is a no slip wall, however the lower boundary of Le Clair's droplet as it has been illustrated in figure 4.9 essentially represents a symmetry boundary condition. Figure 4.9 only shows half the droplet; therefore, an identical half sphere exists forming a complete spherical droplet. Despite these differences the two models exhibit similar characteristics in terms of streamline shape. The tangential surface velocities of both models have been plotted in figure 4.10. Analogous to the location of the center of Le Clair's vortex occurring further to the right, the location of maximum velocity is also right shifted. Le Clair's surface velocity increases instantly from the forward stagnation point, as unlike the COMSOL model, Le Clair's model has no recirculation at the front of the droplet.

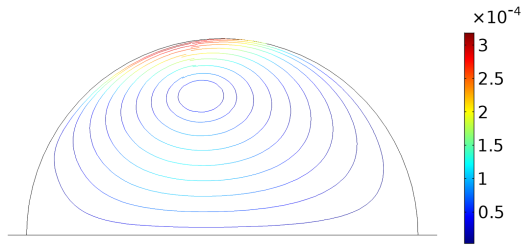


Figure 4.8: Streamlines [ms^{-1}] showing flow within droplet modeled using COMSOL. Maximum velocity occurring at 76.2 degrees from the forward stagnation point. It should be noted that the streamlines exhibit minor discontinuities due to movement in the y-z plane, as discussed in section 4.3.3.

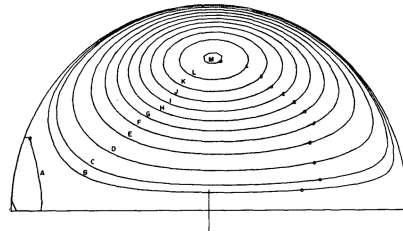


Figure 4.9: Streamlines showing flow within droplet as calculated by Le Clair et al [69]. Maximum velocity occurring at 84 degrees from the forward stagnation point.

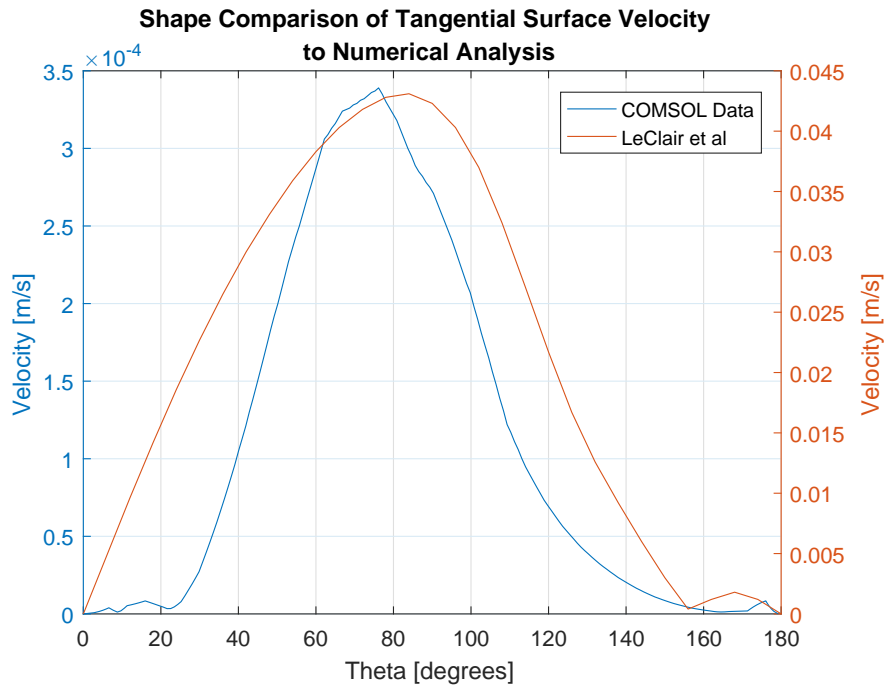


Figure 4.10: Tangential velocities over the surface of the droplet for the COMSOL data and the numerical solution provided by LeClair et al [69].

4.3.2 Analytical Comparison

The flow of the droplet can also be compared to the analytical model developed in section 2. The analytical solution is seen to over predict the result at all points on the surface in figure 4.11. The analytical model assumes creep flow resulting in the symmetrical ellipsoid form of the x-direction surface velocity with the maximum occurring at $x = 0$. The over prediction of velocity is believed to be the result of this creep flow assumption as the early flow separation of the water considerably decreases the velocity of the droplet fluid. Although the surface velocity plots vary considerably between the COMSOL and analytical results, the velocity profiles through the center of the droplet coincide comparatively well as seen in figure 4.12. The COMSOL model calculates the velocity at the droplet apex to be $2.673 \times 10^{-4} \text{ m s}^{-1}$ whilst the analytical solution predicts a velocity of $3.675 \times 10^{-4} \text{ m s}^{-1}$, a difference of 27.3%. This discrepancy is most likely caused by the shifted maximum velocity, as seen in figure 4.11, resulting from the flow separation of the water. However, other than this difference in apex velocities, the profiles follow similar shapes, differing by 12.7% at the location of maximum negative velocity.

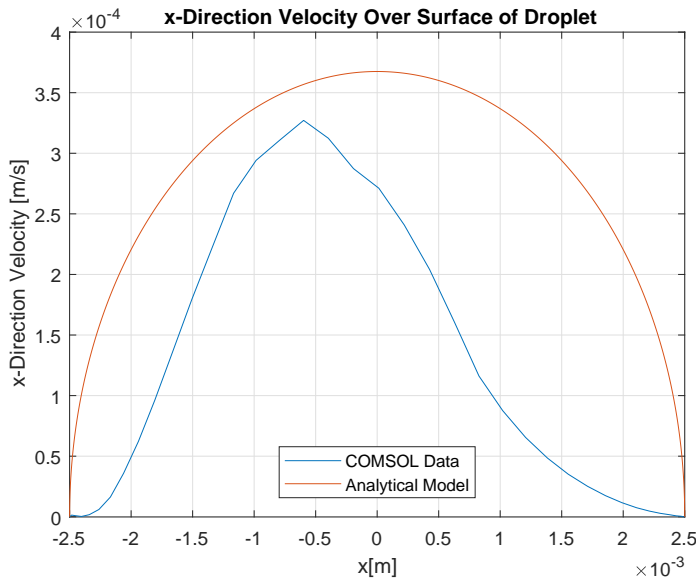


Figure 4.11: Comparison between COMSOL data and analytical solution of the x-direction velocities over the surface of the droplet

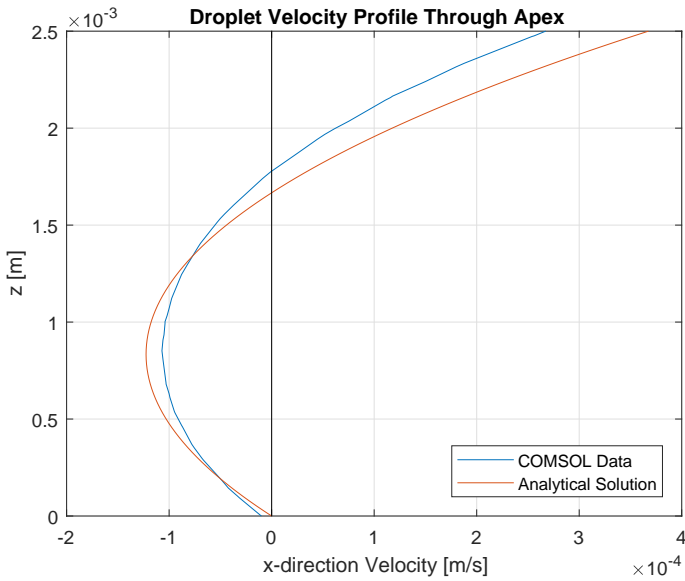


Figure 4.12: Comparison between COMSOL data and analytical solution of the velocity profile through the droplet apex

4.3.3 3D Analysis

Figure 4.13 shows the recirculation paths of 9 particles within the droplet. These paths are seen to follow a similar recirculation pattern as in the 2D plane analysis with the inclusion of some movement in the y direction. When viewed from the front, the circulation paths are tilted on an angle, away from the center of the droplet. When viewed from above, beads moving near the surface in the direction of the flow traverse across the droplet on the outsides and then recirculate back closer to the center. This periodic y-direction movement of the beads is also seen within droplets analyzed during the experiment which follow visually similar paths.

The streamlines shown in figure 4.13 exhibit some irregularities seen as straight lines joining two ends of a curved streamline, increasing in severity toward the sides if the droplet. These irregularities are due to the y-direction movement of particles, separate to that occurring within a recirculation path. This is due to the continuous movement of a particle in the y-direction, away from the center of the droplet. This effect can be seen in figure 4.14 showing two particles beginning at the center of the droplet propagating outward along continuous streamlines. This gradual movement of particles in the y-direction is due to the pressure gradient present within the body

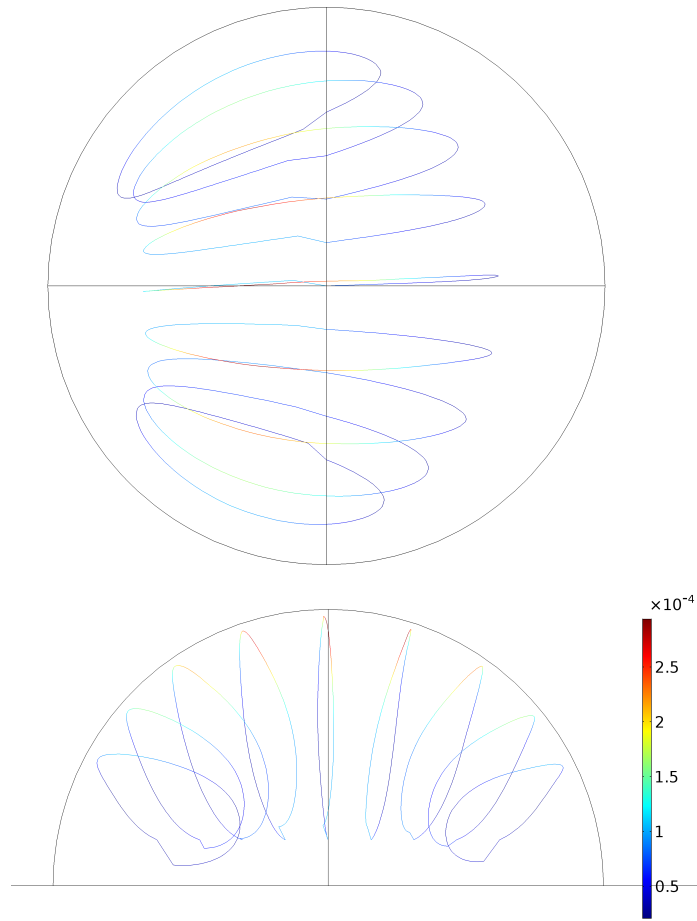


Figure 4.13: Streamlines [ms^{-1}] showing cyclical motion of 9 separate particles. Top view (above), flow moving from left to right. Front view (below), flow moving into page

of the droplet. The pressure distribution at the surface of the droplet is shown in figure 4.15. On inspection of this figure, the regions of maximum pressure on the front face and minimum pressure and near the droplet apex can be seen clearly. In addition to this, an intermediate pressure of approximately 27.6 Pas exists on the rear surface of the droplet caused by exposure to the region of unsteady flow after separation. It is proposed that the pressure gradient causing the streamlines to migrate toward the edges of the droplet is a result of the high momentum of the water flow being incident on the spherical shape of the droplet. The greatest pressure occurs at the front of the droplet, where the surface is most normal to the flow (this maximum pressure would occur at the stagnation point if it were not for the region

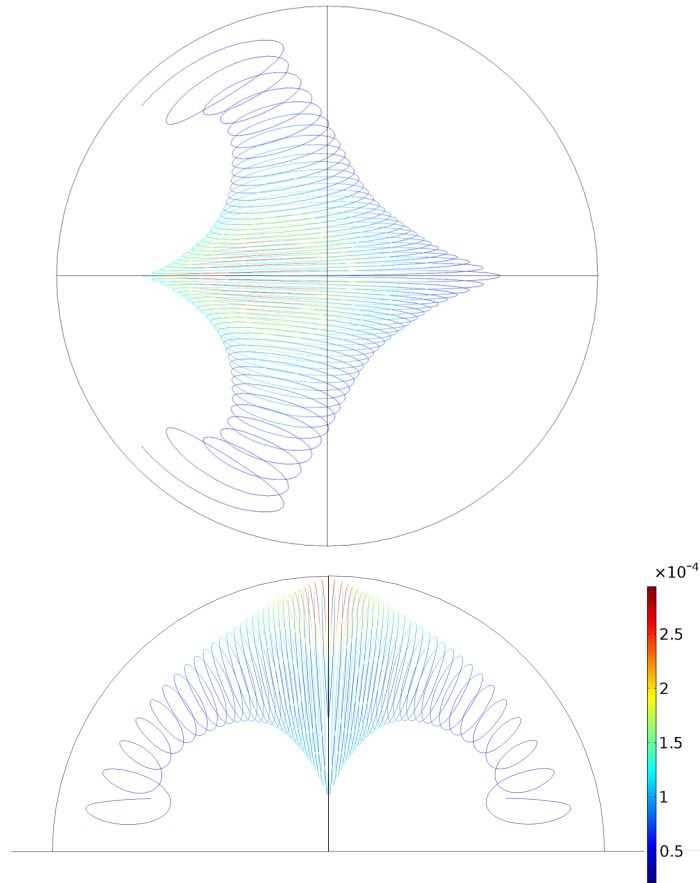


Figure 4.14: Streamlines [ms^{-1}] showing out of plane movement of two particles, originating at the center of the droplet and moving toward the edges. Top view (above), flow moving from left to right. Front view (below), flow moving into page.

of water recirculation at the front of the droplet). As we move toward the side of the droplet (in the y-direction), incident water meets a surface less normal to its current movement in the x direction and therefore exerts less pressure on the surface as it is diverted around the droplet. This decreasing pressure gradient from the center to the side of the droplet is transferred into the body of the droplet causing the vortex movement shown in figure 4.14. It follows that if this is correct, any droplet in a viscous flow will exhibit this out of plane movement toward the sides of the droplet. The effect seen here is pronounced due to the high momentum of the incident water flow, however it should theoretically be present under any conditions.

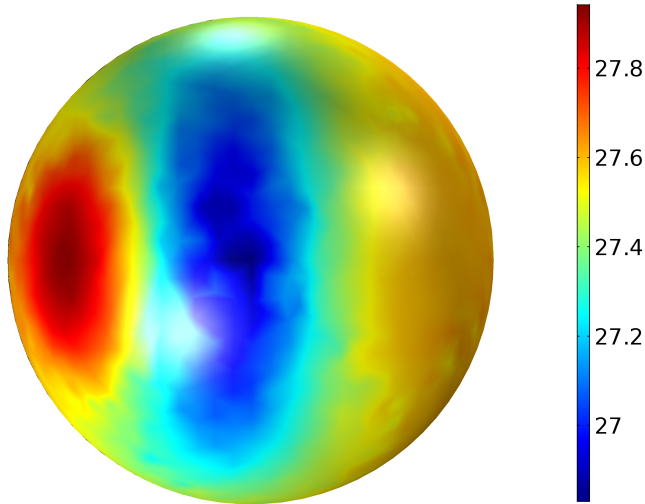


Figure 4.15: Droplet surface pressure distribution [Pa]. Flow moving from left to right

4.3.4 Droplet Shape

The shape of the droplet remained highly circular even with the relatively high density incident flow of water. Figure 4.16 shows the deformed droplet surface exported from COMSOL compared to a half circle of the same radius. The two surfaces vary by a maximum of 1.53% in the radial direction, occurring at the same location as the maximum surface pressure (43.7° from the forward stagnation point, $x = 1.889 \times 10^{-3}m$ in figure 4.16). The radius of the deformed droplet is plotted in figure 4.17 showing a compression of the front face and an extension of the rear face. The perturbations present in the data of figure 4.17 are a result of the linear interpolations performed by COMSOL in defining the droplet surface between mesh nodes. These fluctuations appear significant due to the minor deformation of the droplet however only represent a maximum perturbation of 0.08% in the radial direction. The apex of the deformed droplet is located at $z = 2.5105mm$, a difference of only 0.42% from the undeformed radius of $2.5mm$. As the deformed droplet apex is higher than the original circular geometry and by such a small margin, for the remainder of this study will simply assume the droplet velocity profile to extend from the origin up to $z = 2.5mm$.

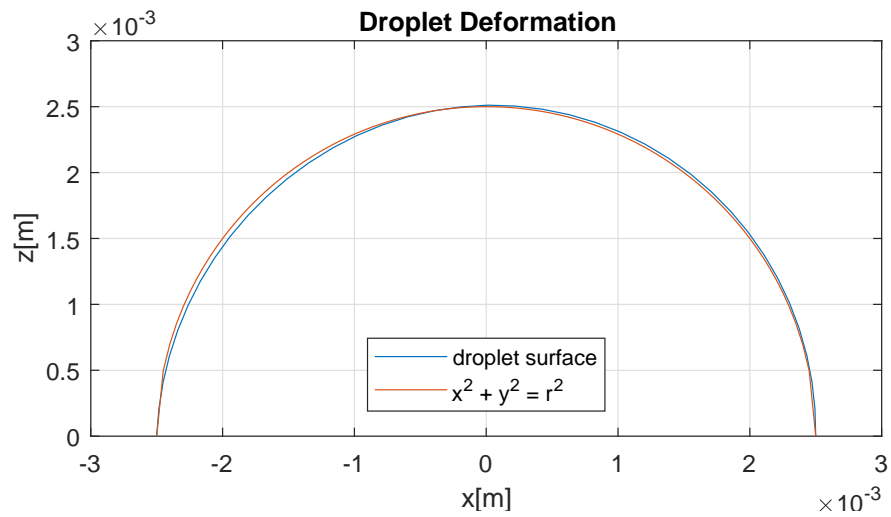


Figure 4.16: Comparison between original circular geometry and deformed droplet surface in the x-z plane

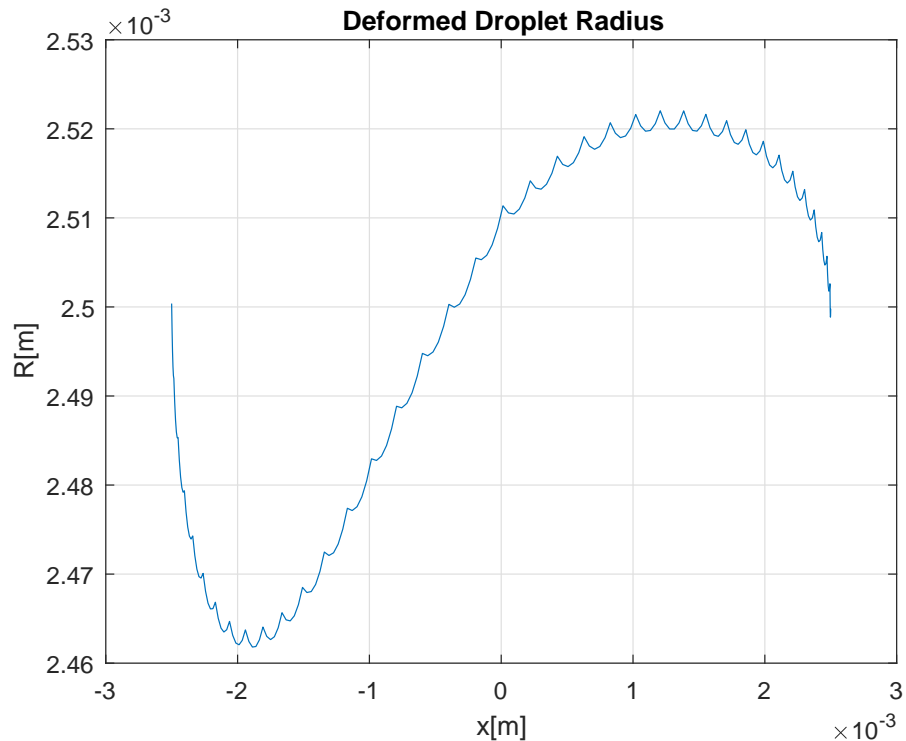


Figure 4.17: Deviation of the deformed droplet radius from the specified geometry of [2.5mm].

4.3.5 Bead Circulation

One of the objectives of this model was to analyze the error associated in the measurement of the beads circulating inside the droplet. The droplets seeded with tracer particles are observed from above through a microscope. The technique currently tracks particles as they traverse under the surface of the droplet, in the direction of flow. The velocity in the x-direction of the particle at several positions along its path is calculated by measuring time taken to travel between positions. The velocity of each particle is converted to a single value by averaging the range of measured velocities. However, not all particles are measured in this technique. Although there is no systematic methodology in place for selected particle to be measured, two conditions were implemented based on the current experimental techniques. These conditions were used to isolate the particles in the COMSOL model (screenshot of seeded droplet shown in figure 4.18) that would theoretically be chosen in the experiment.

Two spatial restrictions were placed on particle motion in order to select applicable particles. Firstly, only beads whose path, in the direction of the flow, moves within the central 25% of the droplet radius, illustrated in the top view of figure 4.19, with bead speeds only being measured within the 'ticked' region. This condition represents measurements not being taken from particles that circulate near the

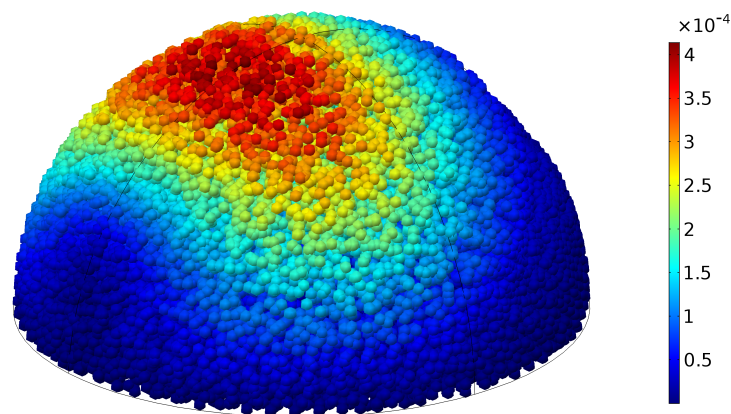


Figure 4.18: Screenshot from COMSOL of tracer particles seeded within droplet, flow moving from front left to back right. The beads are a visual representation generated by COMSOL and do not represent the actual size of the beads.

sides of the droplet. Secondly, the particles must traverse at least 60% of the length of the droplet, illustrated in the side view of figure 4.19. This matches the experimental selection of particles with a long recirculation path as particles circulating along tight paths are not considered. These two constraints were used to select 62 particles that would theoretically be chosen for measurement out of a total of 1000 particles placed within the droplet of the COMSOL model. This data was used to evaluate the effectiveness of measuring the velocity of the beads compared to measuring the recirculation time (the time taken for a bead to complete one revolution). Although the experiment records the average bead velocity, we can use the velocity at the droplet apex to determine the relative errors associated with measuring time and velocity. The recirculation time of the chosen particles was manually calculated by plotting the position of each particle over a study time of 250 seconds with a time step of 1 second, the number of points within one full circulation being equal to the recirculation time. The results of this analysis are presented in the box and whisker plots of figure 4.20 and in the data of table 4.2.

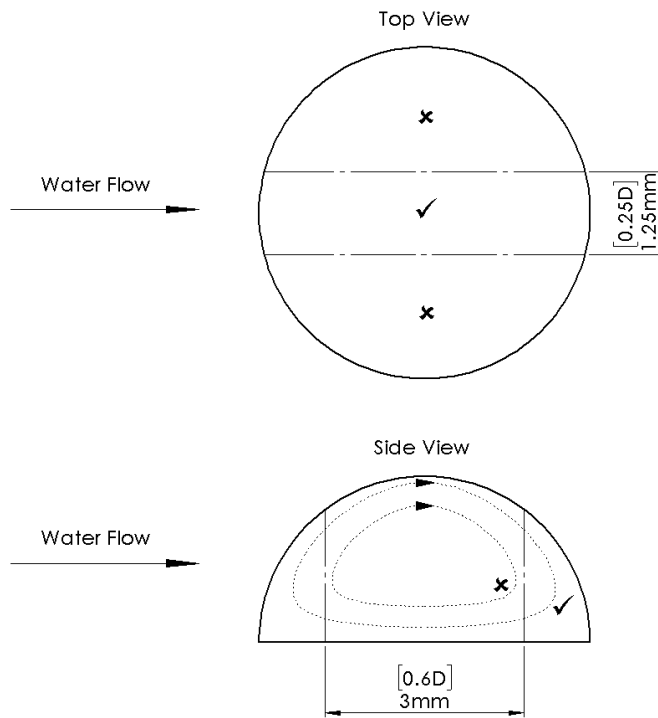


Figure 4.19: Constraints placed of the particles to select those that would theoretically be chosen for measurement in the experiment.

Table 4.2: Key parameters describing the range of data obtained

Statistic	Recirculation Time (secs)	Apex Velocity ($10^{-3}ms^{-1}$)
Minimum	55	2.380
Maximum	225	2.492
Range	170	0.112
Mean	122.1	2.445
Standard Deviation	43.7	0.003

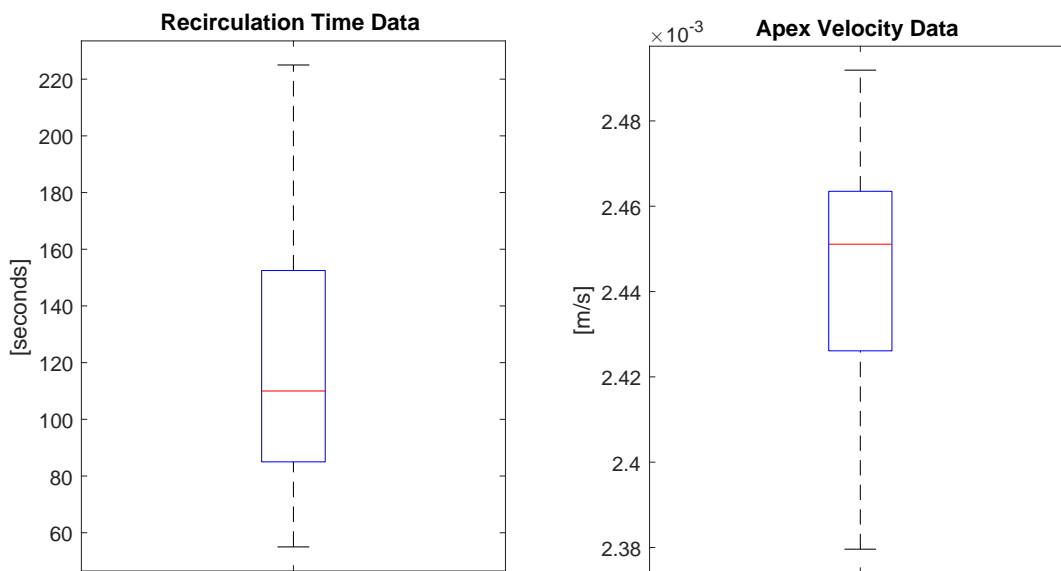


Figure 4.20: Box and Whisker plots showing the distribution of particles in terms of the recirculation time (left) and apex velocity (right).

Half range method error :

$$u_{apex} = 2.45 \times 10^{-3} ms^{-1} \pm 2.30\%$$

$$\tau_{circ} = 122 \text{ secs} \pm 69.6\%$$

This study showed that the error associated with measuring the apex velocity of a particle is 2.3%, compared to a much larger error of 75.8% when considering the recirculation time. An explanation for this large difference in errors is evident in figure 4.21 showing the path and x-direction velocity of two particles. As discussed in section 4.3, the flow within the droplet slows considerably toward the rear of the droplet. This can be seen by the separation of the particle paths as the bead is passing through this region of slow moving flow. The particle with the larger recirculation path ($circ = 166$) extends further into this region of slow flow than that particle with the shorter path ($circ = 96$). This results in the particle with the larger path spending much more time in the lower right quadrant of the droplet. The difference in paths however, lessens considerably at higher velocities resulting in similar measurements of velocity at the droplet apex.

It should be noted that the error calculated in measuring the recirculation time of a bead is likely larger than what would be seen in the experiment. This is due to the flow separation of the water causing the flow to slow considerably toward the rear of the droplet. This slowing of droplet fluid is expected to occur on a smaller scale due to the much lower Reynolds number of the Nitrogen in the experiment. In light of this however, these results still nominate the measurement of velocity as the more accurate method. Although the recirculation time error is overestimated, it is still larger than the error associated with velocity, proving that measuring the bead velocity incorporates less error into the measurement.

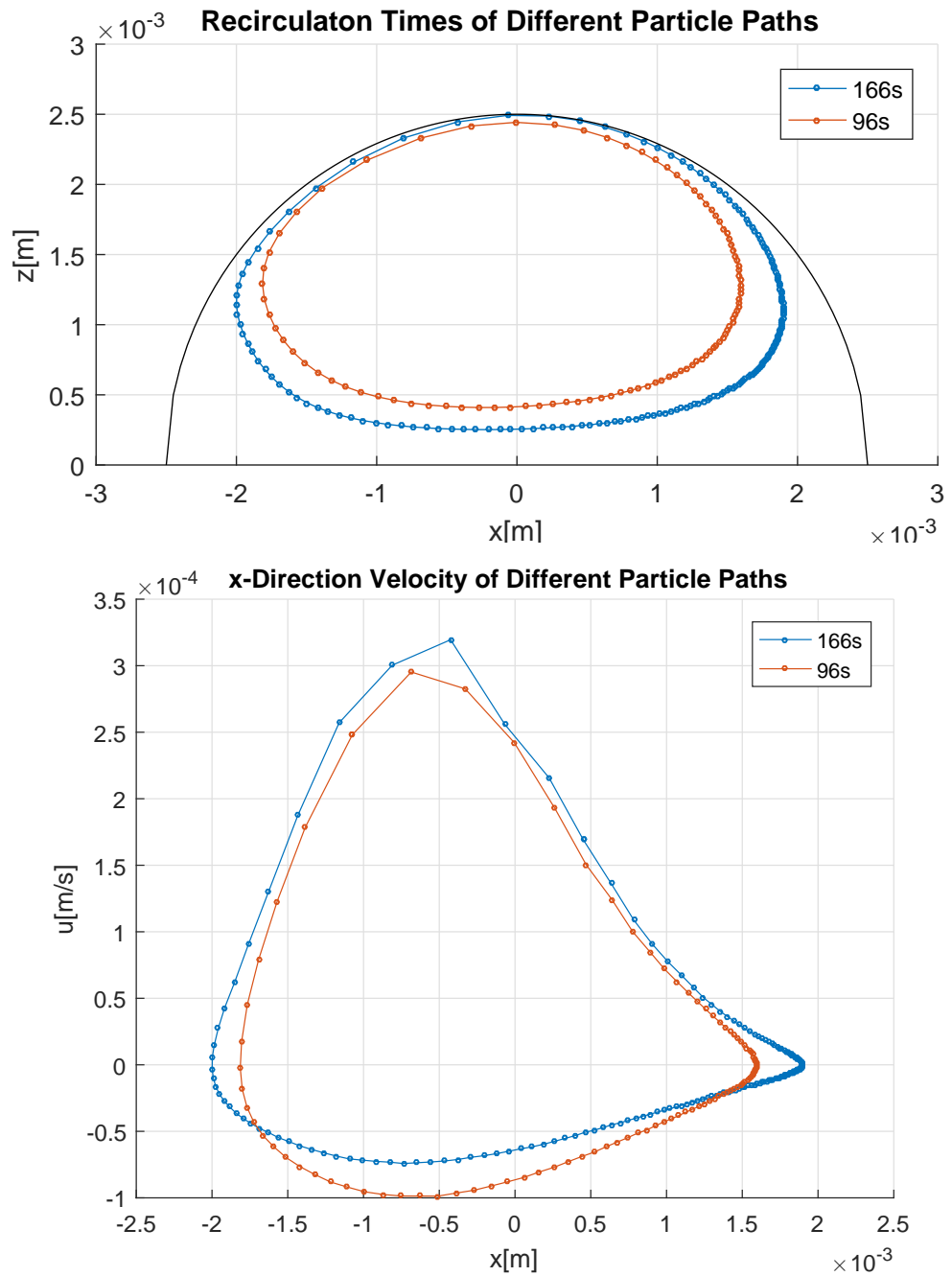


Figure 4.21: Recirculation paths (above) and corresponding path velocities (below) of two particles with recirculation times of 166 and 96 seconds.

Table 4.3: Values of bead velocity at points shown in figure 4.22

	Bead Location	Velocity ($10^{-4}ms^{-1}$)
Fastest Bead	Min 1	1.810
	Min 2	0.393
	Max	3.271
Slowest Bead	Min 1	1.391
	Min 2	0
	Max	2.398

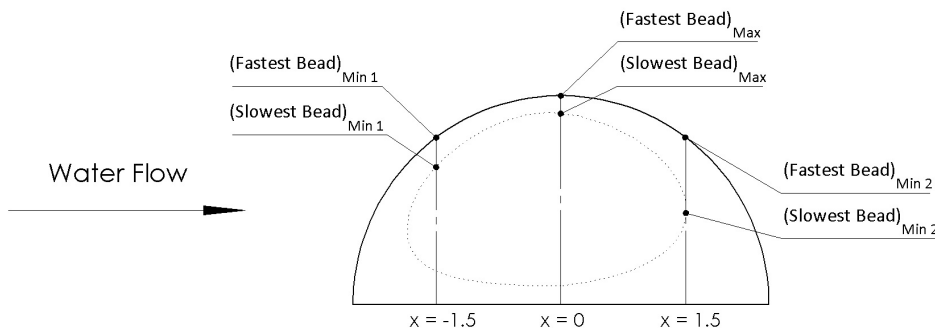


Figure 4.22: Locations of bead velocities used to calculate an equivalent average bead velocity based on the apex velocity.

4.3.6 Calculating a Measure of Average Bead Speed

As mentioned previously, the data presented by Renbaum-Wolff et al [3, 4] are average bead velocities. The velocity of the beads in the x-direction are recorded as the bead traverses across the droplet. In order to adjust the analytical solution to predict the average velocity of a bead, we need to rely on the results from the particle tracing study. The motion of the beads are non-uniform making a prediction of an average bead speed based solely on the analytical model very difficult. The particle tracing study provides data that can be used to define an average bead velocity as a percentage of the apex velocity of a droplet. This value can then be used to adjust the solution of the analytical model to allow a comparison to the experimental data.

The minimum transverse length of a bead is defined as 60% of the diameter of the droplet. The lowest apex velocity of a bead recorded in the particle tracing study was $2.38 \times 10^{-4}ms^{-1}$. This represents the apex velocity of the bead with the smallest recirculation path. The velocity of this same bead was recorded at $x = -1.5mm$

and $x = 1.5\text{mm}$, defining two values for the minimum velocity of the particle within the central 60% of the radius. Two values are recorded for the minimum velocity of this particle due to the different values of velocity at either end of the data collation region. The same measurement can be made of the surface velocity designating the upper bound for a particle's velocity within the data collation region. Figure 4.22 shows the values and locations of the velocities recorded in defining the upper and lower bounds of the particle velocities.

Within the central 60% of the diameter, the surface velocity of the COMSOL model ranges from a maximum of $3.27 \times 10^{-4}\text{ms}^{-1}$ to a minimum of $0.393 \times 10^{-4}\text{ms}^{-1}$, equivalent to a 88.0% variation. The COMSOL model has a high Reynolds number of 2062 resulting in a velocity distribution over the surface of the droplet that increases and decreases sharply, evident in the 88% variation within the data collation region. The analytical model however, assumes creep flow ($Re \ll 1$) resulting in a surface velocity that is symmetrical about $x = 0$ and varies by only 20.0% within the central 60% of the diameter. The analytical model is assumed to be a more reliable measure of the distribution of surface velocity relevant to the experiment as it assumes a much more similar Reynolds number. An adjustment factor is required to account for the effect of the differing surface velocity distributions between the COMSOL and analytical models. Assuming that the beads within the droplet increase and decrease in velocity in the same manner as the surface velocity, we can use the surface velocity of the analytical model to adjust the minimum velocity of the beads in the COMSOL model shown in figure 4.22 to more relevant values. The assumption that the surface velocity distribution is equal to the bead velocity distribution is considered reasonably accurate due to the relatively small distance between the bead and the droplet surface within the data collation region. However, this assumption becomes less valid as a particle moves closer to the 60% bound. The range of surface velocities over the central 60% of the data predicted by the analytical model is equal to:

$$\frac{\text{Surface Velocity at } x = 0.3R}{\text{Surface Velocity at } x = 0} = \frac{7.29 \times 10^{-8}}{9.11 \times 10^{-8}} = 0.80$$

Assuming this relationship extends into the body of the droplet carrying the beads:

$$\therefore (\text{Bead Speed})_{Min} = 0.80(\text{Bead Speed})_{Max}$$

Updating the minimum bead velocities:

$$(\text{Fastest Bead})_{Min} = 0.80(\text{Fastest Bead})_{Max}$$

$$= 0.80(3.271 \times 10^{-4})$$

$$= 2.617 \times 10^{-4}$$

$$(\text{Slowest Bead})_{Min} = 0.80(\text{Slowest Bead})_{Max}$$

$$= 0.80(2.398 \times 10^{-4})$$

$$= 1.918 \times 10^{-4}$$

We now have a minimum and maximum bead velocity for the fastest and slowest measured beads (upper and lower bounds respectively). These can be used to define an average velocity for the fastest and slowest beads:

$$(\text{Fastest Bead})_{Average} = \frac{(\text{Fastest Bead})_{Min} + (\text{Fastest Bead})_{Max}}{2}$$

$$= \frac{(2.617 \times 10^{-4}) + (3.271 \times 10^{-4})}{2}$$

$$= 2.944 \times 10^{-4}$$

$$(\text{Slowest Bead})_{Average} = \frac{(\text{Slowest Bead})_{Min} + (\text{Slowest Bead})_{Max}}{2}$$

$$= \frac{(1.918 \times 10^{-4}) + (2.398 \times 10^{-4})}{2}$$

$$= 2.158 \times 10^{-4}$$

Lastly, the average values for the upper and lower bounds can be used to calculate a representative average velocity of a bead:

$$\begin{aligned} \text{Average Bead Velocity} &= \frac{(\text{Fastest Bead})_{\text{Average}} + (\text{Slowest Bead})_{\text{Average}}}{2} \\ &= \frac{(2.944 \times 10^{-4}) + (2.158 \times 10^{-4})}{2} \\ &= 2.551 \times 10^{-4} \end{aligned}$$

We will define this velocity as a ratio of the surface apex velocity. This ratio will then be used to convert the apex surface velocity of the analytical model into an approximate average velocity:

$$\begin{aligned} \text{Velocity Ratio} &= \frac{\text{Average Bead Velocity}}{\text{Surface Velocity at Apex}} \\ &= \frac{2.551 \times 10^{-4}}{3.271 \times 10^{-4}} \\ &= 0.780 \end{aligned}$$

The average bead speed can therefore be approximated as 78.0% of the surface apex velocity. This value is used in section 2 to allow a comparison between by data presented by Renbaum-Wolff [3, 4] and the proposed analytical solution.

CHAPTER 5

Parametric Studies

The purpose of this project was to investigate potential sources of error that could be contributing to the large uncertainties present in experimental results. The model that has been developed can now be used to perform parametric studies in an attempt to quantify the relative effects of changing certain variables. Namely, this section studies the effect of droplet drafting, surface tension, size, and contact angle. The results of each study have been presented relative to the current parameters of the model, with the results summarized over the range of each study in section 5.6.

5.1 Droplet Drafting

The production of the droplets involves nebulizing the fluid and then depositing the droplets onto a hydrophobic slide which is placed inside the flow cell [4]. This results in droplets randomly arranged on the surface of the slide. Multiple droplets are studied during the experiment, some of which may be subject to disturbances in the flow resulting from upstream droplets. It was therefore decided that the effect of droplet drafting in the form of flow shielding from an upstream droplet was to be investigated. Two identical droplets were placed in the domain with a separation of one droplet radius ($R = 2.5\text{mm}$) parallel to the direction of the flow. The inlet and outlet boundaries were extended to ensure the droplets are positioned at the same distance from the boundaries as in all other studies. The resulting geometry can be seen in figure 5.1. A parametric study was not performed related to the effect of drafting due to the dissimilarities between the Reynolds number of the simulation compared to that in the experiment (2062 compared to 0.017). As can be seen in figure 5.2, the downstream droplet lies almost entirely within the wake of the upstream droplet. The flow around the actual droplets is not expected to produce this region of unsteady flow due to a much lower Reynolds number. This simulation will therefore be used to define an upper limit on the potential error due to droplet drafting.

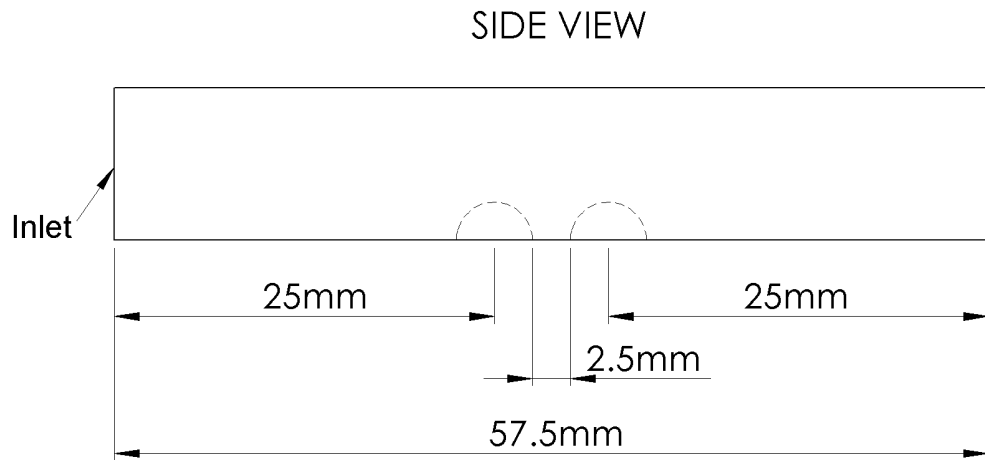


Figure 5.1: Relative positioning of droplets and boundaries in drafting formation.

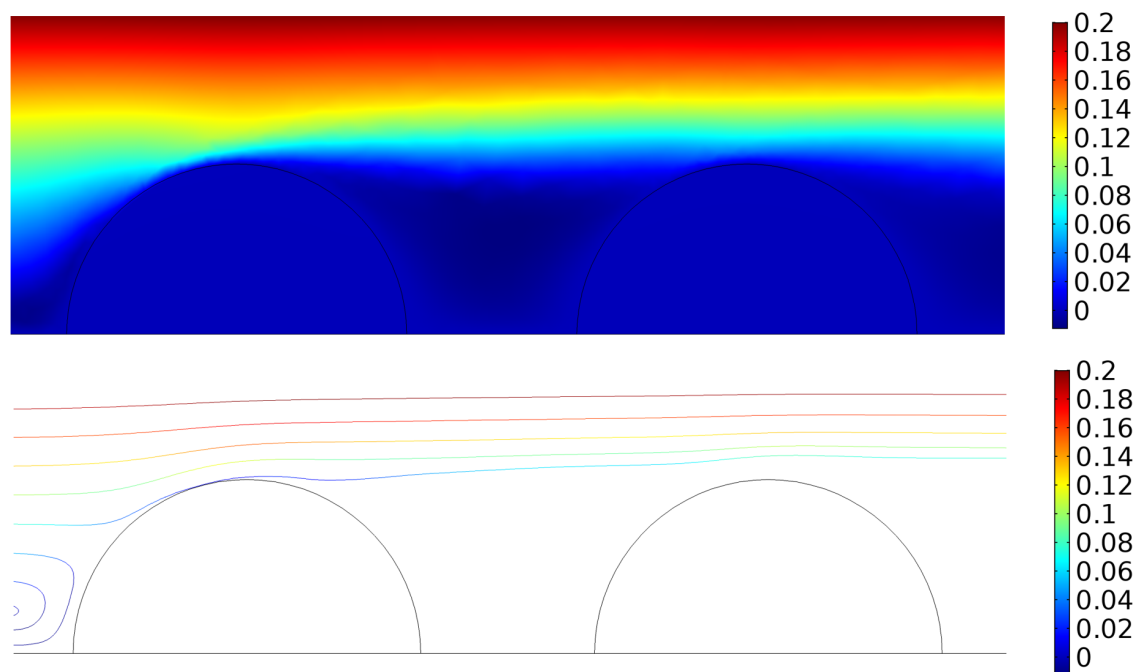


Figure 5.2: Surface velocity plot (above) and streamlines (below) in ms^{-1} in x-z plane showing the downstream droplet largely within the wake of the upstream droplet.

As expected, the upstream droplet exhibits much higher velocities than the downstream droplet due to its exposure to higher velocity flow. The velocity field is seen to only partially recover by the time it reaches the surface of the second droplet resulting in the rear droplet being largely influenced by the region of unsteady flow produced by the upstream droplet. Figures 5.3 and 5.4 show the velocity profiles through the droplet apexes and the tangential surface velocities respectively. The apex and surface velocities of the rear droplet are 47.7% and 58.1% lower than that of the upstream droplet respectively, as shown in table 5.1. It should also be noted that the location of the maximum surface velocity moves further back for the downstream droplet (66.6° compared to 80.7° degrees from the forward stagnation point). This is due to the change in the incident water flow resulting from the upstream droplet's wake. The upstream droplet is exposed to the fully developed velocity profile present in the domain, incurring a large amount of momentum transfer from the water domain. The downstream droplet however, only sees a portion of this mainstream flow and only near the apex of the droplet. Thus, the driving force of the flow has decreased and shifted higher on the droplet resulting in the shifted location and magnitude of the maximum surface velocity of the downstream droplet seen in figure 5.4.

Another outcome of this study is the fact that the upstream droplet exhibits higher velocities than the original singular droplet, with the apex and surface velocities having increased by 13.6% and 16.9% respectively. It is proposed that this is due to the presence of the downstream droplet disrupting the region of unsteady flow behind the upstream droplet, causing the flow of droplet fluid past the rear surface to slow by a lesser extent. The droplet fluid in the upstream droplet therefore retains more momentum through the rear of the droplet, increasing the measured velocities.

Table 5.1: Relative velocities of upstream and downstream droplets

	Apex Velocity	Max Surface Velocity
Upstream Droplet [$10^{-4}ms^{-1}$]	3.03	3.96
Downstream Droplet [$10^{-4}ms^{-1}$]	1.59	1.66
Percentage Change	47.7%	58.1%

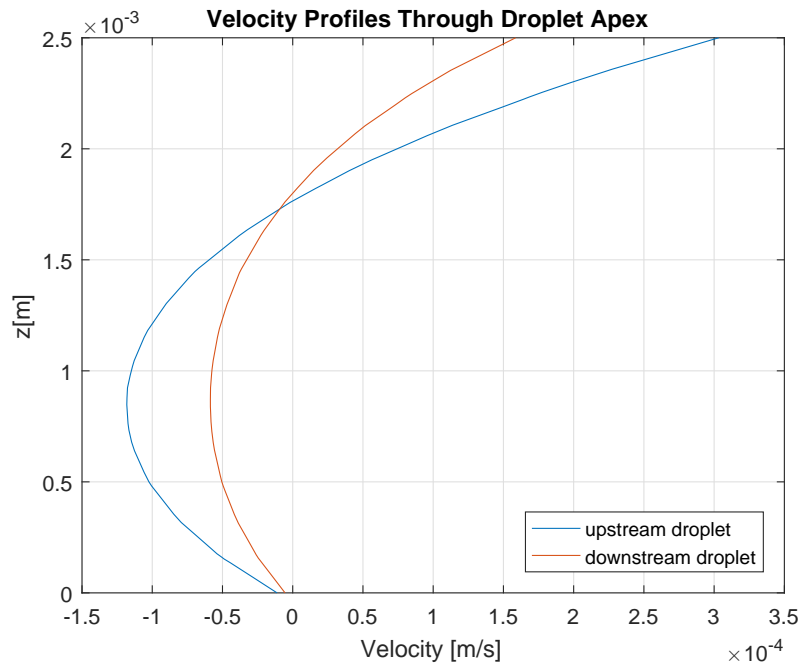


Figure 5.3: Droplet velocity profiles of Upstream and Downstream Droplets.

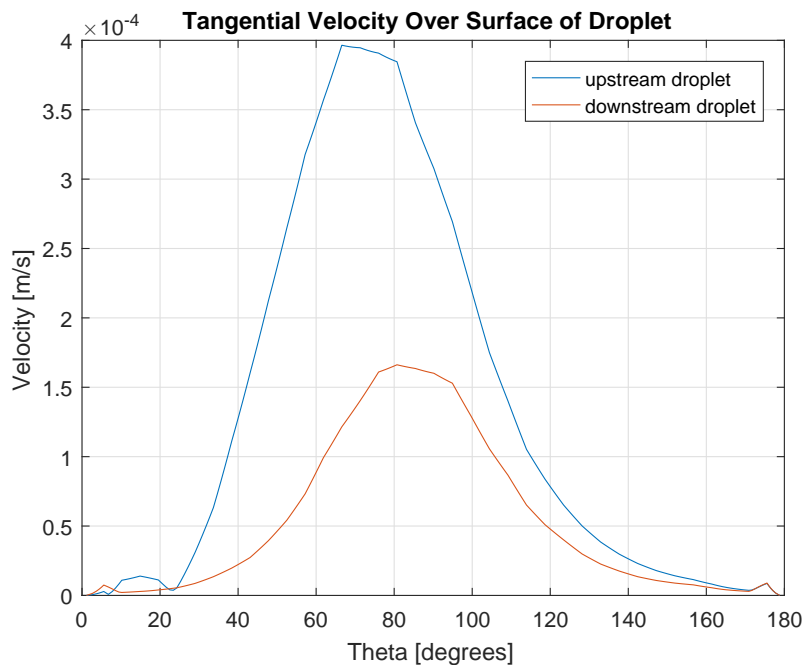


Figure 5.4: Surface Velocities of Upstream and Downstream Droplets.

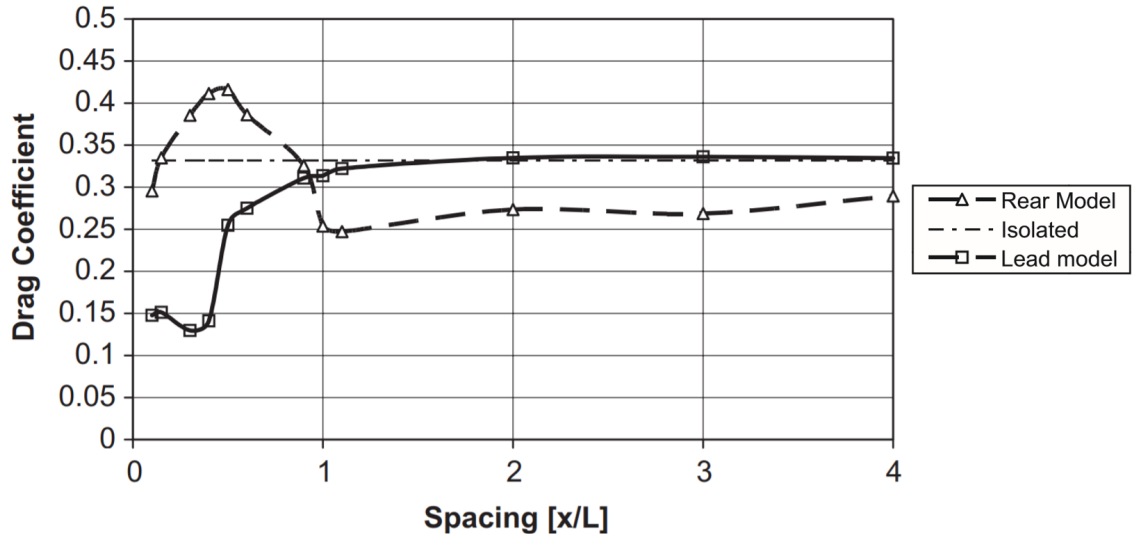


Figure 5.5: Drafting coefficients of Ahmed bodies presented by Watkins and Vino [70].

This disruption of the unsteady flow behind the upstream droplet is evident a study of the effects of drafting by Watkins and Vino (ref). Watkins and Vino studied the effect of car spacing on highways by studying the drag on Ahmed bodies. As shown in figure 5.5, the drag coefficient of the lead model was found to be less than that of the rear and isolated models for spacing less than approximately 1. The Reynolds number of this study was very high (2.3×10^{-6}), however, the spacing of droplets in the COMSOL model equates to 0.5 placing it well within the drafting zone of figure 5.5. For low spacing, the presence of the rear body disrupts the unsteady flow behind the front body, decreasing the pressure drag. This is evident in the lower drag coefficient of the lead model. This same effect is occurring in the COMSOL model, although drag calculations are unable to be made for reasons discussed in section 3.2, page 52.

5.2 Surface Tension

The surface tension of the droplet was varied to isolate potential discrepancies in the data that may arise from the varying surface tensions of the known standards used to construct the calibration curve [4]. The surface tension was ranged from 0.001Nm^{-1} to 0.13Nm^{-1} as seen in table 5.2. This range was based on a central value of the current surface tension of the droplet, set at 0.007Nm^{-1} , approximately equal to that of water. As a general sense of scale, ethanol has a relatively low surface tension of approximately 0.002Nm^{-1} and mercury has a very high value of approximately 0.4Nm^{-1} [71].

An increasing surface tension is seen to produce lower velocities within the droplet as seen in table 5.2. The shape of the velocity profiles and surface velocities plots, shown in figures 5.6 and 5.8 respectively, are seen to remain fairly constant. As discussed in section 4.3.4, the droplet shape is highly spherical resulting in no change in the shape of the droplet surface due to its surface tension, even when the value is dropped as low as 0.01Nm^{-1} . It is proposed that high values of surface tension results in the droplet surface acting as a 'shell' between the water and droplet phases, decreasing the amount of momentum transfer resulting in the lower observed droplet velocities.

Table 5.2: Variations in apex and maximum surface velocities resulting from altering the surface tension of the droplet.

Surface Tension [Nm^{-1}]	Apex Velocity		Max Surface Velocity	
	Velocity [10^{-4}ms^{-1}]	Percentage Change	Velocity [10^{-4}ms^{-1}]	Percentage Change
0.01	3.27	22.2%	3.75	10.7%
0.03	2.83	6.0%	3.49	2.9%
0.07	2.67	0%	3.39	0%
0.13	2.54	-4.8%	3.25	-4.3%

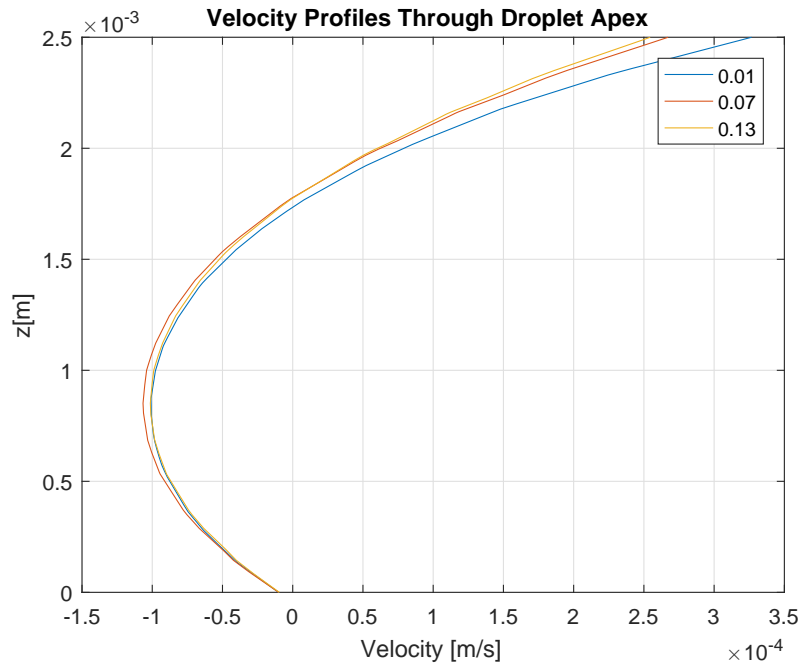


Figure 5.6: Variation in droplet profiles resulting from altering the surface tension of the droplet.

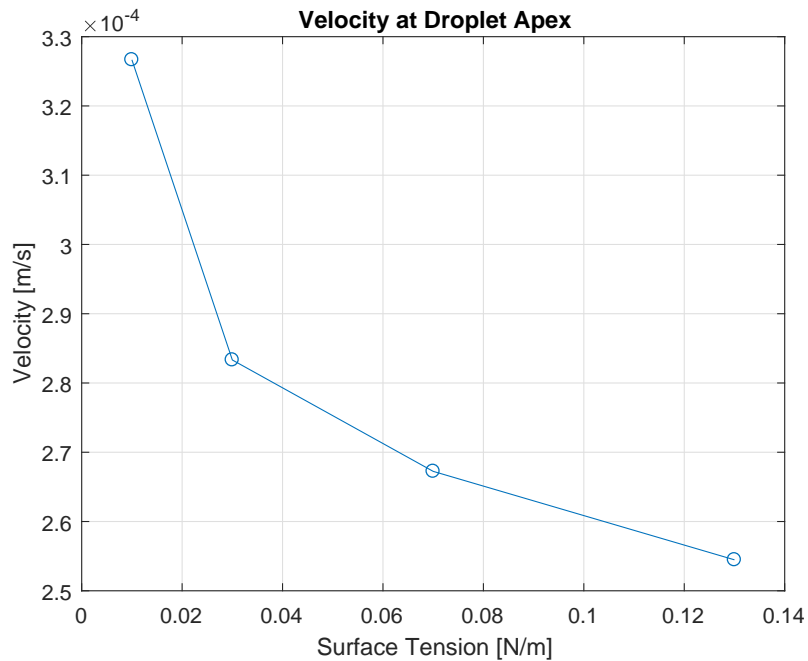


Figure 5.7: Variation in apex velocity resulting from altering the surface tension of the droplet.

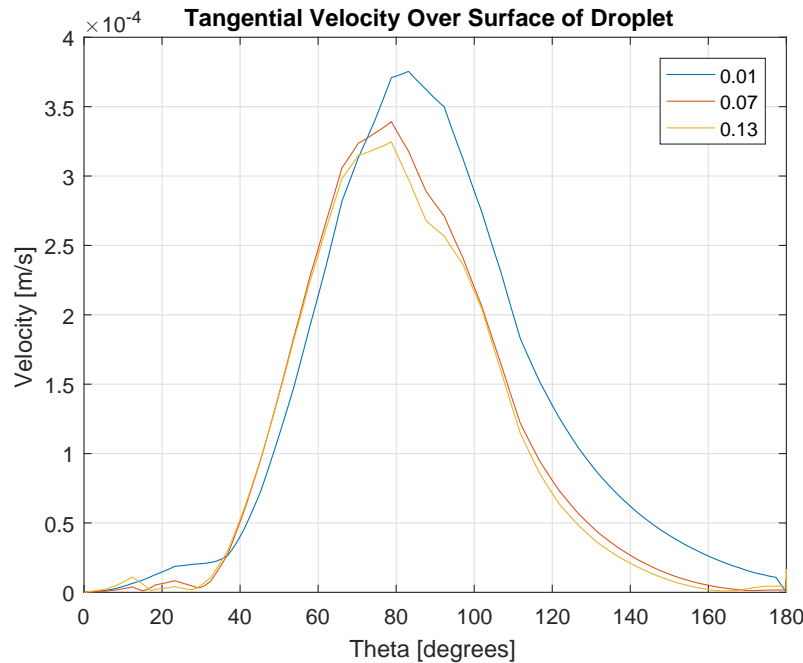


Figure 5.8: Variation in surface velocity resulting from altering the surface tension of the droplet.

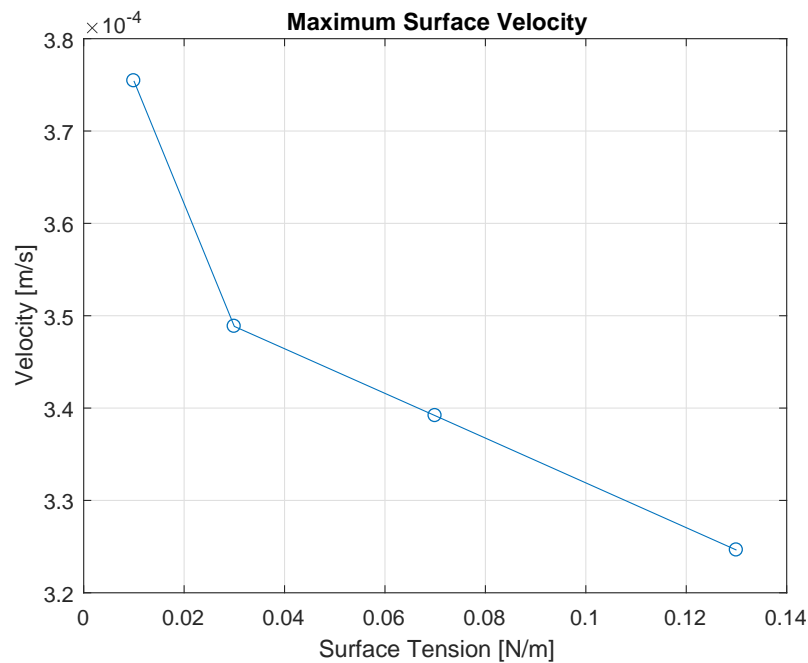


Figure 5.9: Variation in maximum surface velocity resulting from altering the surface tension of the droplet.

5.3 Size

Renbaum Wolff [4] reported a droplet diameter range between $30\mu m$ and $50\mu m$. The range studied here represents a slightly broader relative variation with the diameter ranging from $2mm$ to $5mm$ as shown in figure 5.10. The computational domain was extended to encompass the central droplet by the same relative dimension with each study, ensuring each droplet is exposed to the same flow. The normalized plot of the velocity profiles in figure 5.12 shows there is no visible change in the shape of the profiles between droplet sizes, with the exception of the small deviation made by the $1mm$ radius droplet. The normalized surface velocity plots of figure 5.15 however, show that as the radius is decreased, the relative velocity increases on either side of the maximum value. This is due to the larger droplets extending further into the mainstream flow, causing the higher velocities seen in figures 5.11 and 5.14. However, the lower section of the larger droplet is still exposed to the slower moving flow close to the lower boundary. Therefore, relative to its maximum velocity, a larger droplet will exhibit lower velocities on its faces upstream and downstream of the location of maximum surface velocity.

The apex and maximum surface velocity plots of figures 5.13 and 5.16 respectively are seen to produce a reasonably linear relationship and have therefore been fitted using single degree polynomials. The analytical solution for the velocity at the droplet apex has been included in both figures 5.13 and 5.16 as the analytical model predicts the apex and maximum surface velocities to be equal, effectively predicting both values. As consistent with the analytical results discussed in section 2, the analytical solution over predicts the both sets of velocity data given by the COMSOL. The polynomials are presented in the form $V = aR - b$ with V and R representing the relevant velocity and droplet radius respectively whilst a and b represent constants. The values of these constants and are given in table 5.4. The velocities are seen to increase linearly due to the shape of the velocity profile of the surrounding fluid. As shown in section 3.1.4, page 46, the profile of the fluid immediately surrounding the droplets increases almost linearly as we move away from the boundary. This is due to the small relative size of the droplets placing them well within the boundary layer of the flow through the flow cell. Therefore, increasing

the droplet diameter exposes the apex of the droplet to a linearly increasing flow velocity. Thus, the effective incident velocity on the droplet also increases linearly, resulting in the relationships seen in figure 5.13 and 5.16.

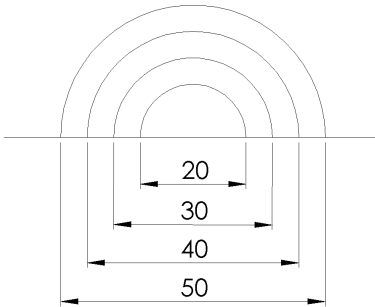


Figure 5.10: Droplet sizes studied.

Table 5.3: Variations in apex and maximum surface velocities resulting from altering the size of the droplet.

Droplet Radius [mm]	Apex Velocity		Max Surface Velocity	
	Velocity $[10^{-4} \text{ms}^{-1}]$	Percentage Change	Velocity $[10^{-4} \text{ms}^{-1}]$	Percentage Change
1	1.01	-62.1%	1.15	-66.2%
1.5	1.69	-36.8%	2.01	-40.6%
2	2.41	-10.0%	3.00	-11.5%
2.5	2.67	0%	3.39	0%

Table 5.4: Comparison of fitted polynomial function constants between analytical solution and experimental results. Recalling the function to be in the form $V = aR - b$. The R^2 value given is the coefficient of determination.

	Velocity	a	b	R^2 value
COMSOL Data	Apex	0.1139	4.875×10^{-6}	0.9677
COMSOL Data	Max Surface	0.1544	3.127×10^{-6}	0.9731
Analytical Solution	Max,Apex	0.1470	1.782×10^{-19}	1

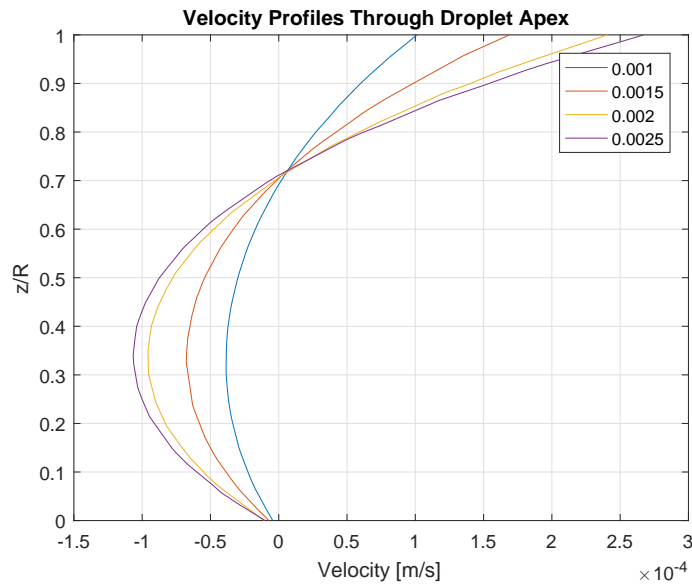


Figure 5.11: Variation in droplet profiles resulting from altering the radius of the droplet noting that the y axis is a ratio of the droplet radius.

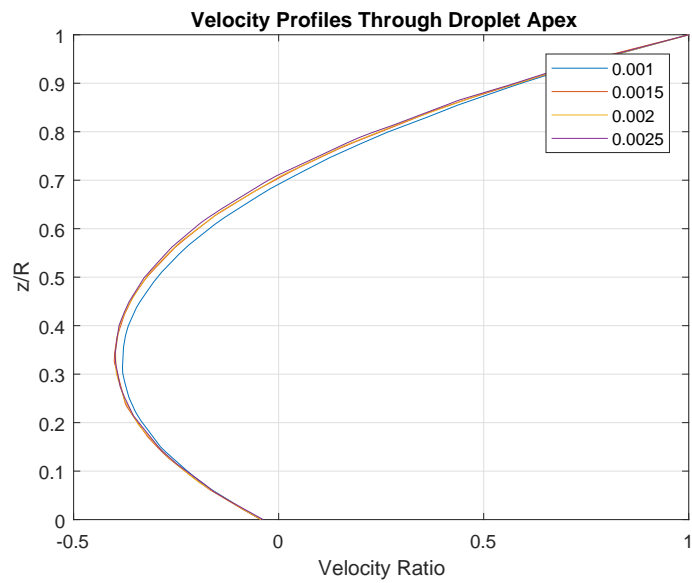


Figure 5.12: Variation in shape droplet profiles resulting from altering the radius of the droplet noting that the y axis is a ratio of the droplet radius and the x axis is a ratio of the apex velocity.

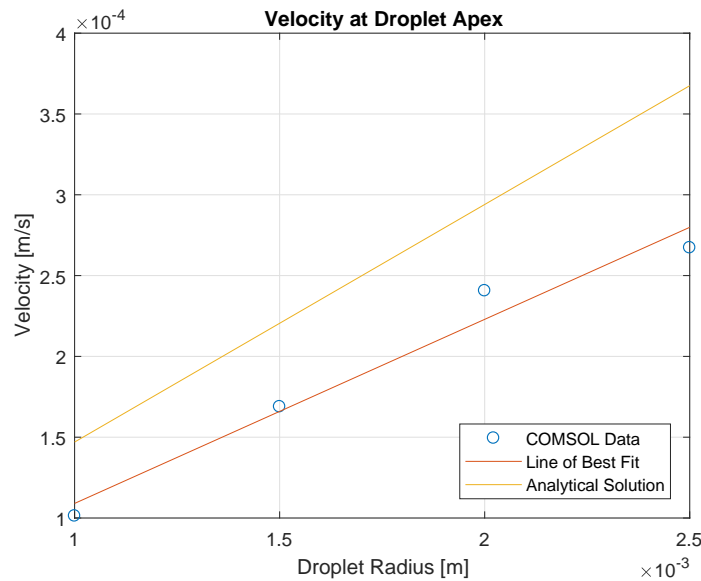


Figure 5.13: Droplet apex velocity as a function of the radius fitted using a single degree polynomial and the prediction made by the analytical solution.

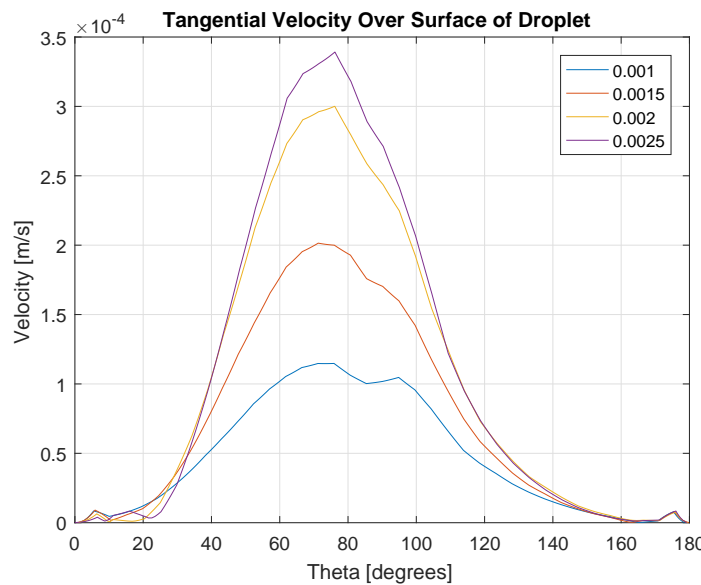


Figure 5.14: Variation in tangential surface velocity resulting from altering the radius of the droplet .

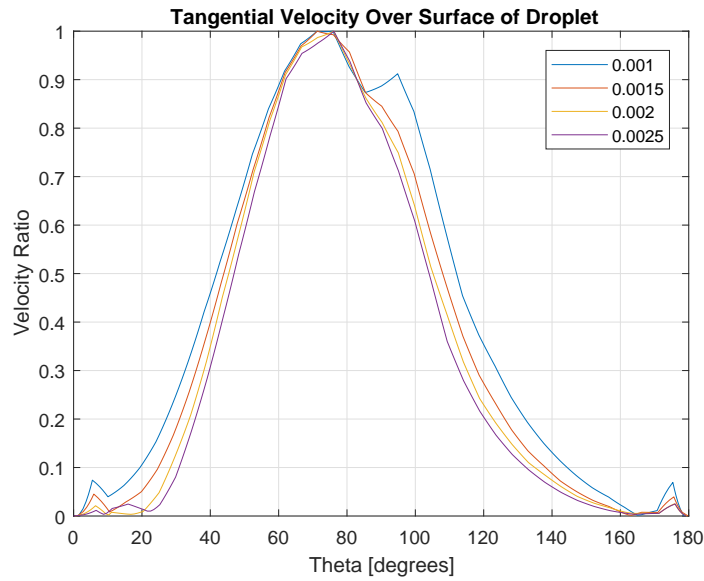


Figure 5.15: Variation in shape of tangential surface velocities resulting from altering the radius of the droplet noting that the y axis is a ratio of the maximum velocity.

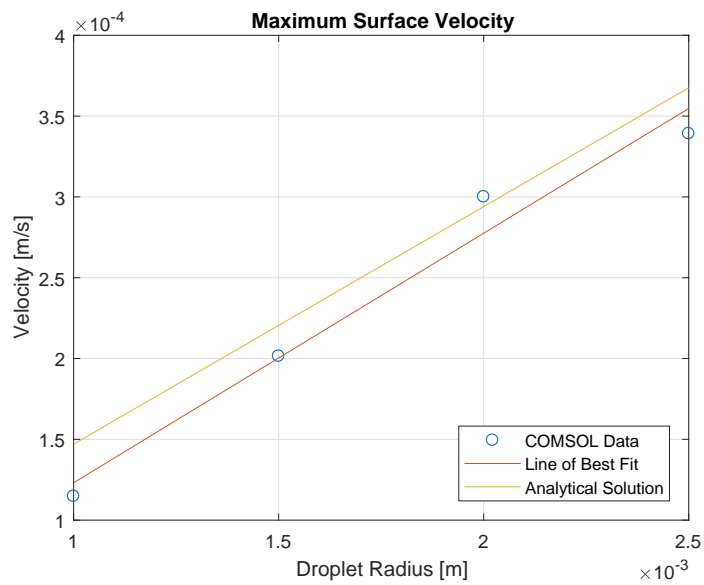


Figure 5.16: Maximum surface velocity as a function of the radius fitted using a single degree polynomial and the prediction made by the analytical solution.

5.4 Contact Angle

The study of the effect on the contact angle between the droplet surface and the lower boundary has been divided into two sections; study A and study B. Study A varies the contact angle whilst holding the position of the droplet apex constant in order to eliminate the effects caused by increasing droplet height, as can be seen in figure 5.23. Study B varies the contact angle of the droplet whilst holding the diameter of the droplet constant as seen by the observer from above, specifying a the droplet span as 5mm. As discussed previously, the droplets are viewed from above through a microscope. Therefore, the observer sees a diameter equal to the widest point of the droplet. As seen in figure 5.23, for droplets with a contact angle larger than 90° degrees this viewed diameter does not equal the diameter at the lower surface. The same range of contact angles of 50°, 70°, 90° and 110° were analyzed in both studies. As the flow dynamics of these two studies are very similar, flow patterns of studies A and B will be discussed together, followed by the results study A and the results of study B. Increasing the contact angle of the droplet alters both the water a droplet fluid flows. Tables 5.7 and 5.8 show the increase in non-uniform flow of the water phase at the front and rear of the droplet. Firstly, a higher contact angle results in a larger region of recirculation at the front of the droplet. This occurs as the front face of the droplet becomes steeper, increasing its imposition of the flow. As the contact angle increases, the rear of the droplet also becomes steeper, resulting in a larger region of unsteady flow behind the droplet caused by flow separation. Increasing the contact angle therefore creates a body that becomes less streamlined and more bluff bodied. The droplet fluid is seen to exhibit more circular motion with an increasing contact angle, corresponding to the more circular boundary of the droplet flow. As expected, the more circular shape of the droplet allows the droplet fluid to rotate more regularly and also provides less space for the regions of recirculation in the lower corners of the droplet. These observations hold true for both study A and B. The results differ between the two studies due to the increasing contact angle in study B causing an increasing in droplet height resulting from the diameter constraint. Analogously droplet size, this exposes the droplet to higher velocity flow which increases the droplet fluid velocity.

5.4.1 Study A

Figure 5.17 shows the resulting diameters of the droplets for the contact angles studied. There are two sets of competitive mechanisms present when considering the effect of the droplet geometry on the water and droplet phase flows. Firstly, the bodies are becoming less streamlined as the contact angle is increased. This stimulates flow within the droplet due to the steeper front face of the droplet causing more opposition to the flow of water, resulting in more momentum transfer into the droplet phase. This is counteracted however, by the fact that a higher contact angle creates a larger region of flow recirculation at the front of the droplet and a larger region of unsteady flow at the rear of the droplet. Secondly, due to the height constraint, a decreasing contact angle results in an increased droplet length. This provides the water flow with a larger surface area though which momentum transfer can occur.

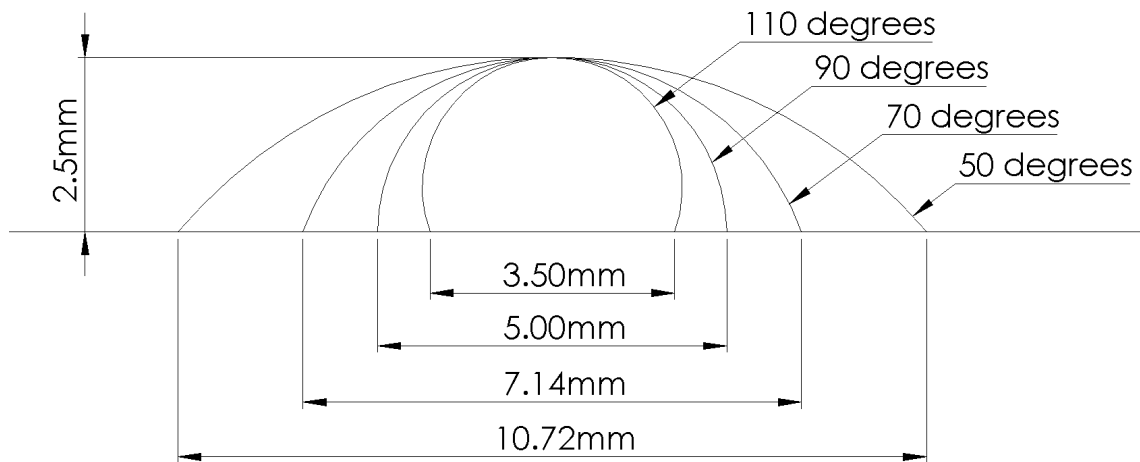


Figure 5.17: Geometry of contact angles studied with a constant droplet height.

Figures 5.19 and 5.21 show the apex and maximum surface velocities increase from angles 50° through to 90° , and then decrease to the value at 110° . This suggests that between the contact angles of 70° and 110° , there exists a droplet shape of maximum efficiency in terms of droplet flow. The velocities seen in droplets of contact angles 50° and 70° show that at low angles, the effects of the increased area available for momentum transfer and smaller regions on non-uniform flow are outweighed by the lack of opposition of the surface to the water phase flow. The water is able to flow easily over droplets at low angles as indicated by the small deformation in the streamlines seen in table 5.7. Contrastingly, the velocities present within the droplet with a contact angle of 110° shows that the large regions of non-uniform water flow at the front and rear of the droplet and decreased droplet surface area are more detrimental to the momentum transfer from the water phase than the effect of the highly curved water streamlines. Between the contact angles 70° and 110° , a droplet geometry possesses the most efficient combination of these competitive mechanisms. The result of these flow dynamics are velocities that increase to a maximum value and then decrease as the contact angle continues to increase. In addition to the varying values of velocities, the location of the maximum surface velocity moves further back on the droplet as shown by figure 5.22. This is a result of the diversion of the mainstream flow around the larger regions of flow recirculation at the front of the droplet present at higher contact angles. This means the mainstream flow acts on a smaller area of the droplet, closer to the apex, moving the location of the maximum surface velocity further back. Thus, the driving force of the flow is shifted further towards the apex producing a more centrally located droplet vortex stagnation point as can be seen in table 5.6.

Table 5.5: Variations in apex and maximum surface velocities resulting from altering the contact angle whilst holding the height of the droplet constant.

Contact Angle [degrees]	Apex Velocity		Max Surface Velocity	
	Velocity $[10^{-4}ms^{-1}]$	Percentage Change	Velocity $[10^{-4}ms^{-1}]$	Percentage Change
50	1.55	-42.0%	2.03	-40.3%
70	2.20	-17.6%	2.79	-17.7%
90	2.67	0%	3.39	0%
110	2.08	-22.2%	2.36	-30.3%

Table 5.6: Streamlines of droplet phase over droplet with varying contact angle whilst holding the height of the droplet constant

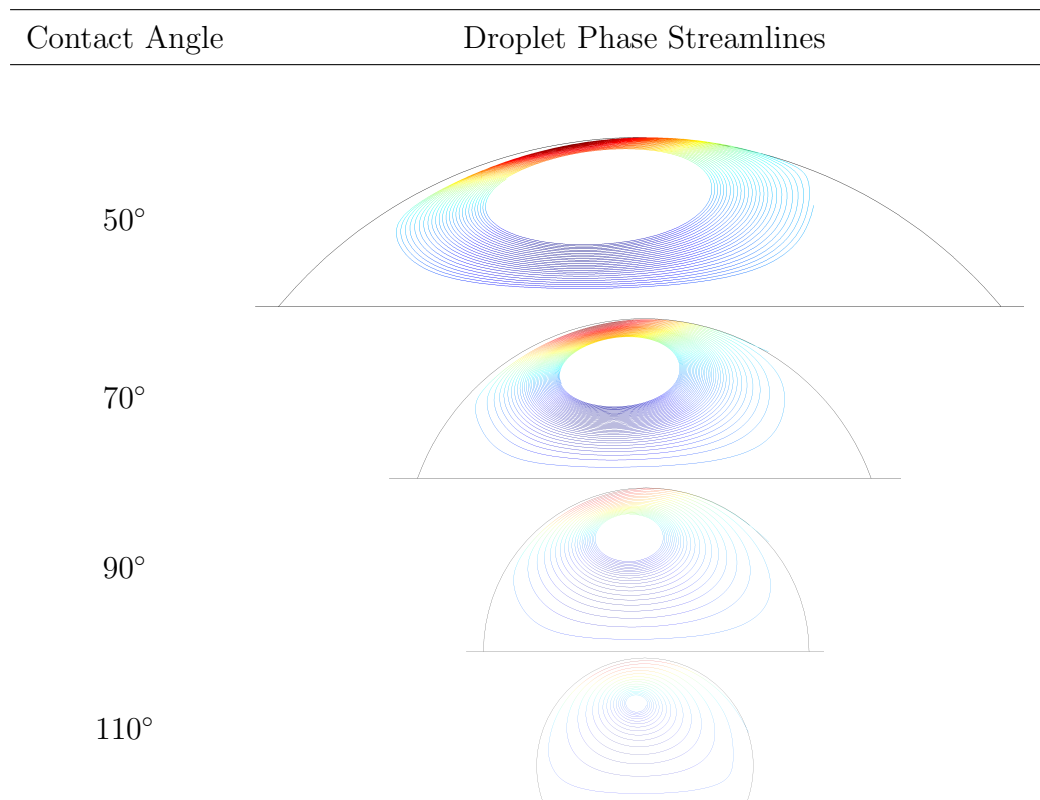
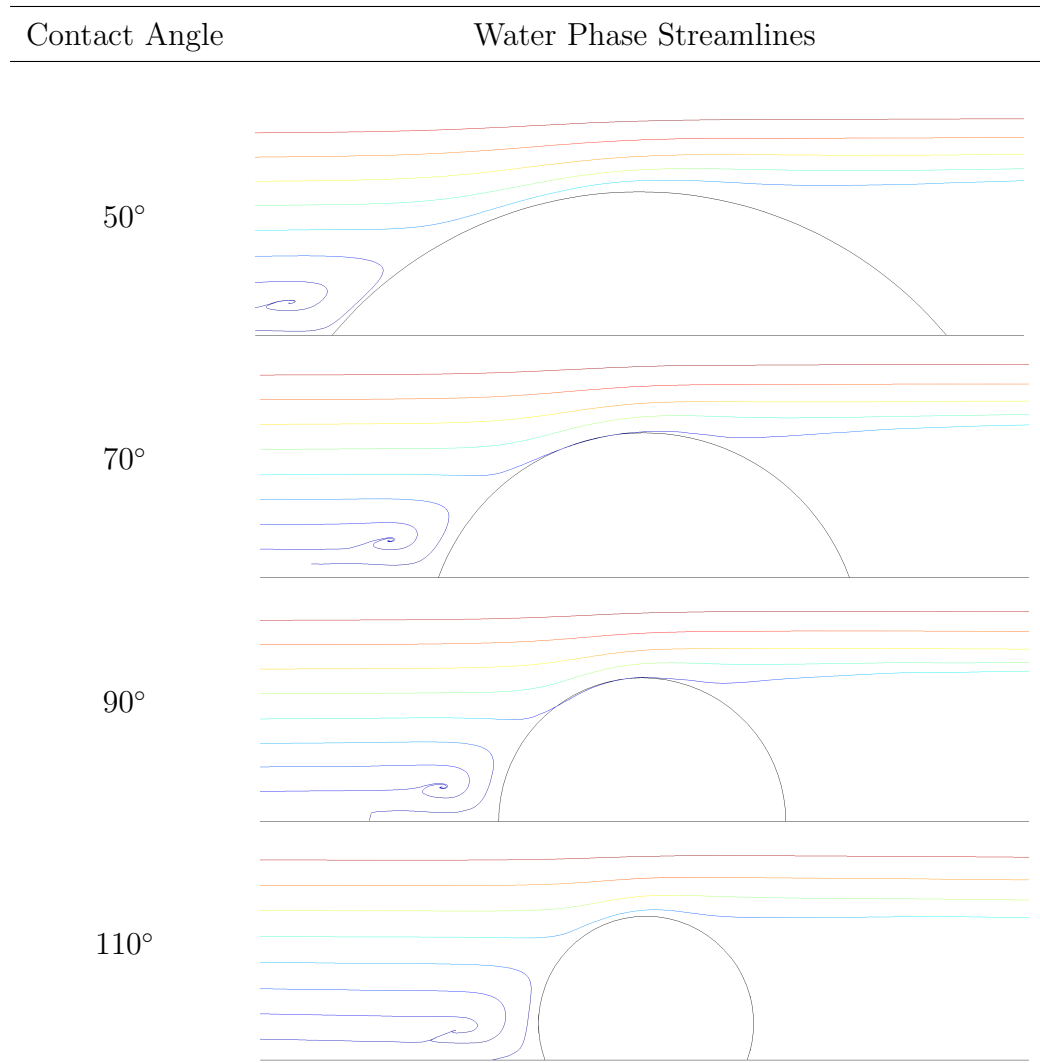


Table 5.7: Streamlines of water phase over droplet with varying contact angle whilst holding the height of the droplet constant



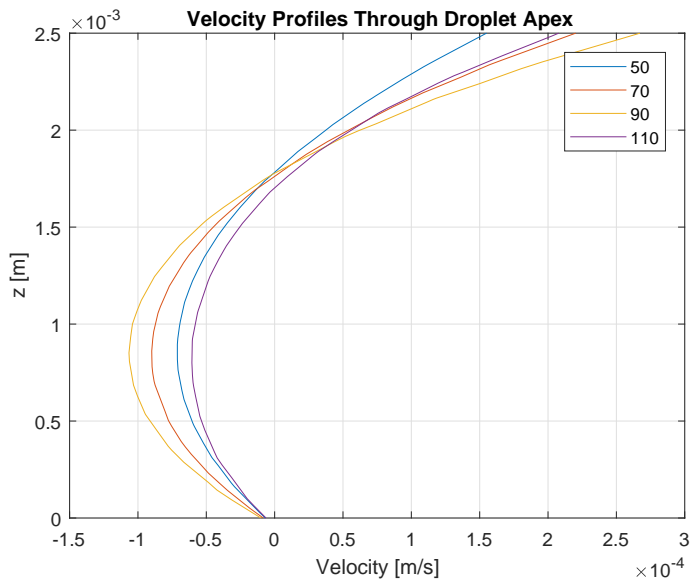


Figure 5.18: Variation in droplet profiles resulting from altering the contact angle of the droplet whilst holding the droplet height constant.

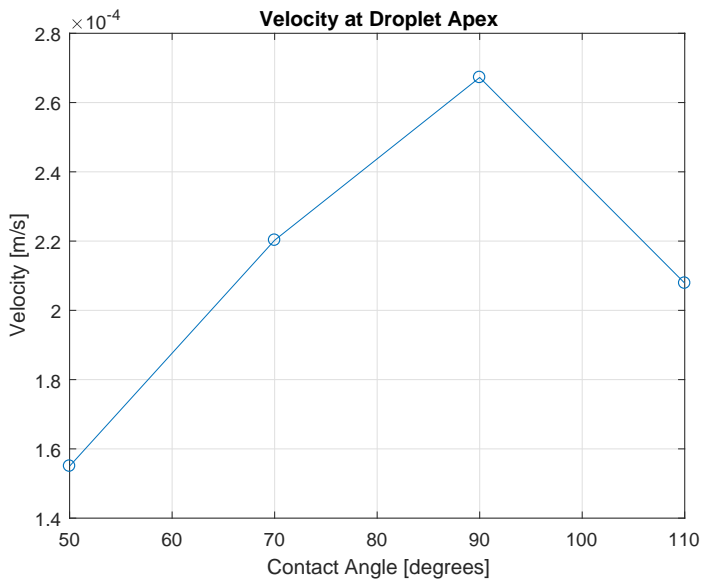


Figure 5.19: Variation in apex velocity resulting from altering the contact angle of the droplet whilst holding the droplet height constant.

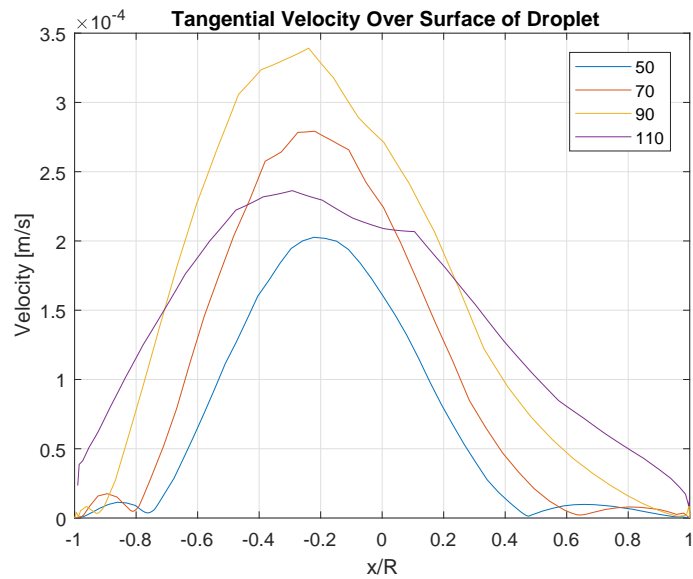


Figure 5.20: Variation in surface velocity resulting from altering the contact angle of the droplet whilst holding the droplet height constant.

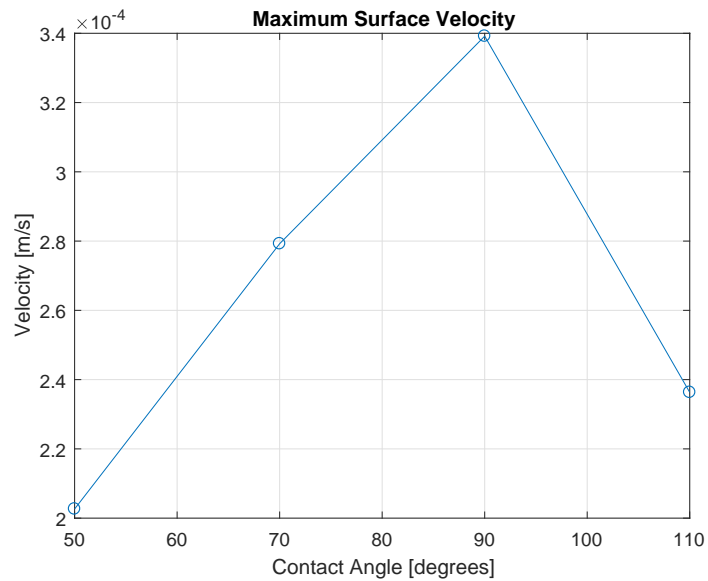


Figure 5.21: Variation in maximum surface velocity resulting from altering the contact angle of the droplet whilst holding the droplet height constant.

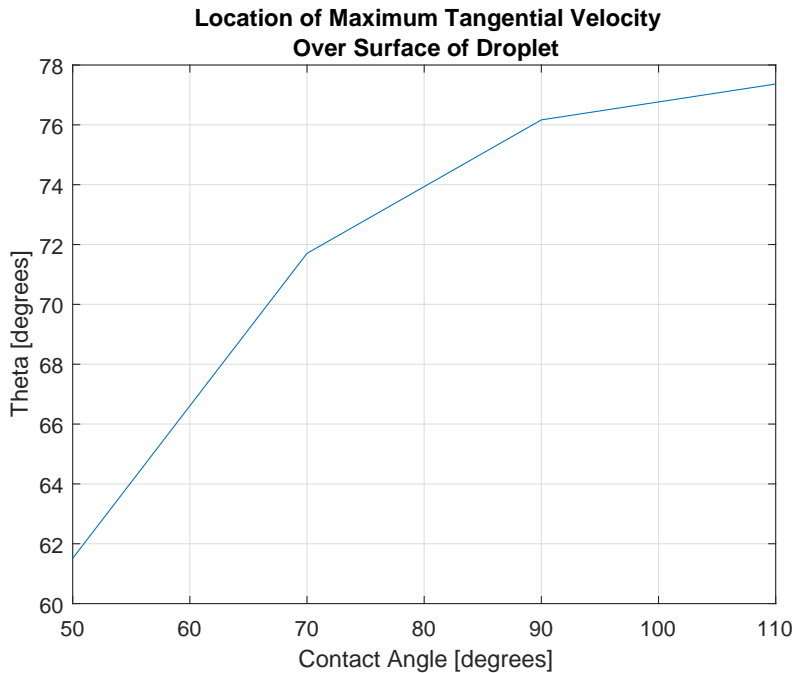


Figure 5.22: Variation in location of maximum surface velocity resulting from altering the contact angle of the droplet whilst holding the droplet height constant.

5.4.2 Study B

Study B maintains a constant droplet width whilst varying the contact angle resulting in droplets of varying height as seen in figure 5.23. This study simulates a varying contact angle as viewed by the observer. Similar competitive mechanisms to study A exist in these droplets as they are the same shape as those previously analyzed. The difference between the studies is that droplets of lower contact angle no longer possess a larger area and droplets at higher contact angles extend further into the mainstream flow, resulting in exposure to higher velocity flow. As can be seen in figures 5.24 through 5.27, droplets of with higher contact angles exhibit higher velocity flow. This suggests that the combined effect of exposure to higher velocity flow and more pronounced water phase streamline curvatures outweighs the formation of larger regions of unsteady flow at the front and rear of the droplet. The gradients of figures 5.25 and 5.27 increase with an increasing contact angle with the velocities between angles 50° and 70° differing by approximately 20%, whilst velocities between angles 90° and 110° differ by approximately 120%. This

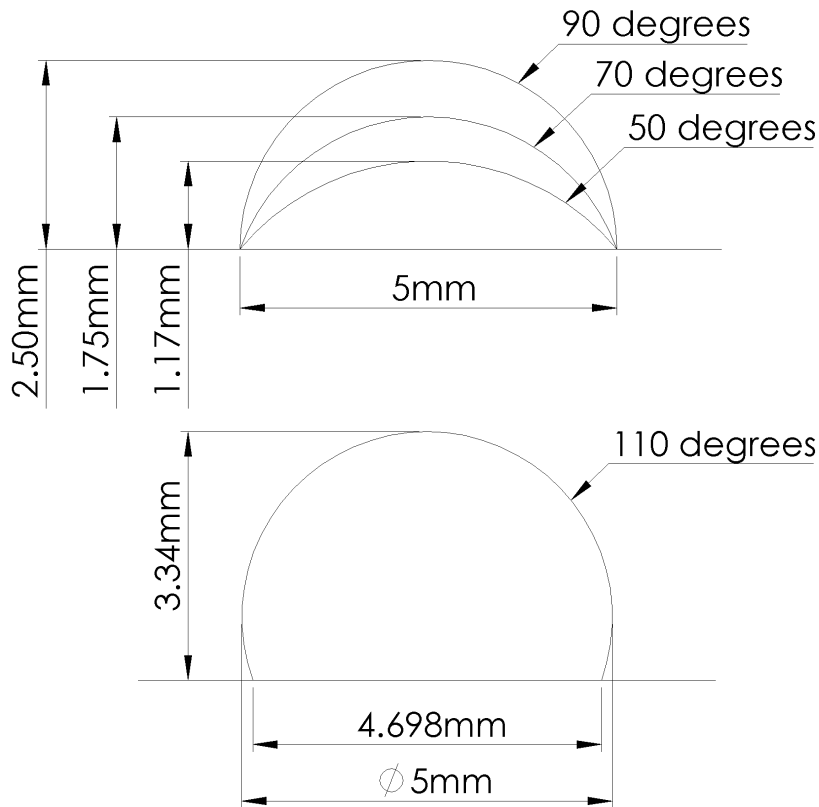


Figure 5.23: Geometry of contact angles studied with a constant droplet width.

is due to the droplet height increasing by larger increments as the contact angle increases linearly. A similar movement of the location of the maximum surface velocity as in study A is also seen, although to a lesser extent. On observation of figure 5.28, a large drop in the location of the maximum surface velocity is seen due to the uncharacteristically deformed surface velocity plot for a contact angle of 70° . However, if this value is regarded as an outlier and not considered, a gradual increase in the location of the maximum surface velocity, measured as θ , from the forward stagnation point is seen.

Table 5.8: Streamlines of water phase over droplet with varying contact angle whilst holding the width of the droplet constant

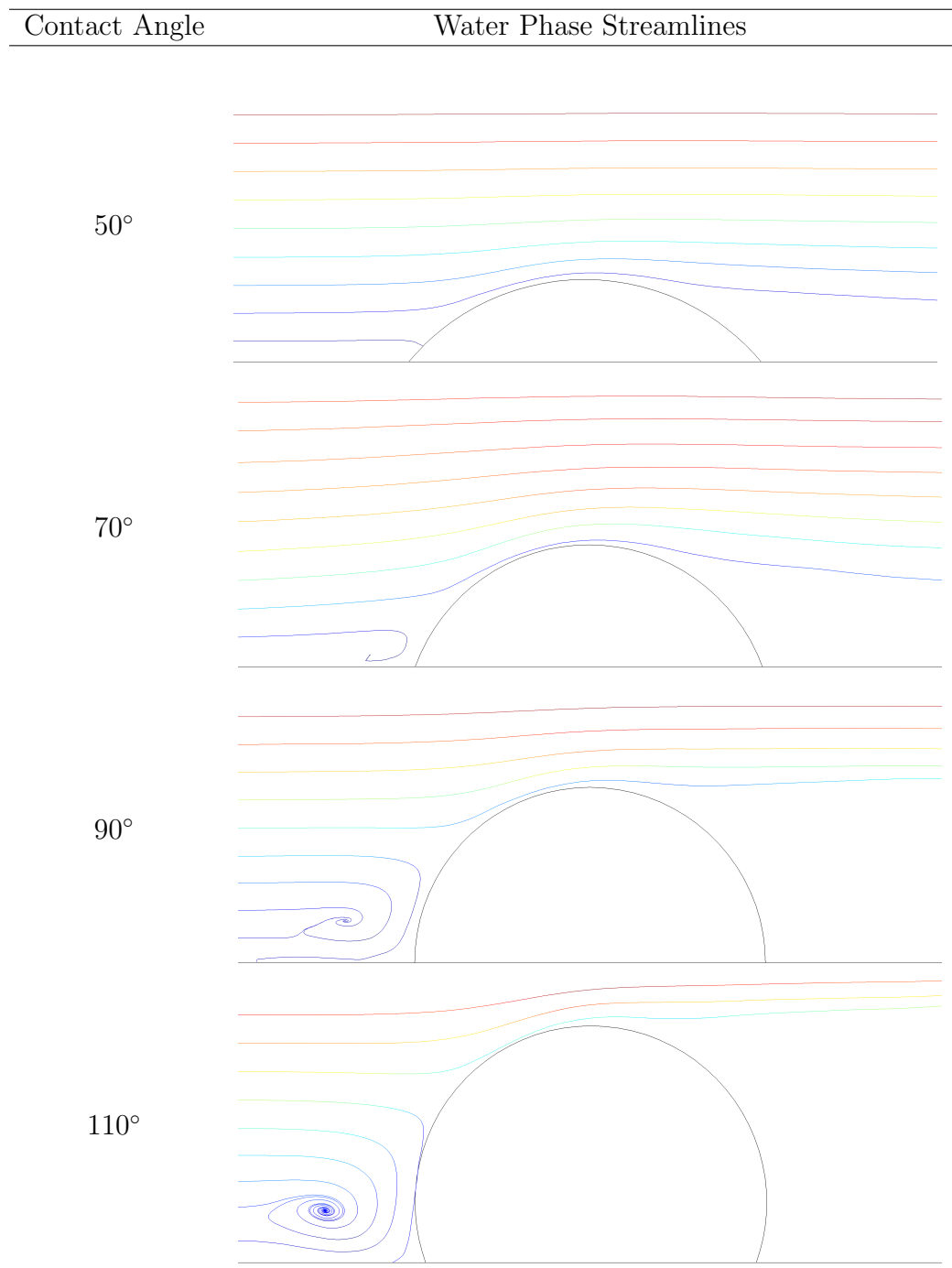


Table 5.9: Streamlines of droplet phase over droplet with varying contact angle whilst holding the width of the droplet constant

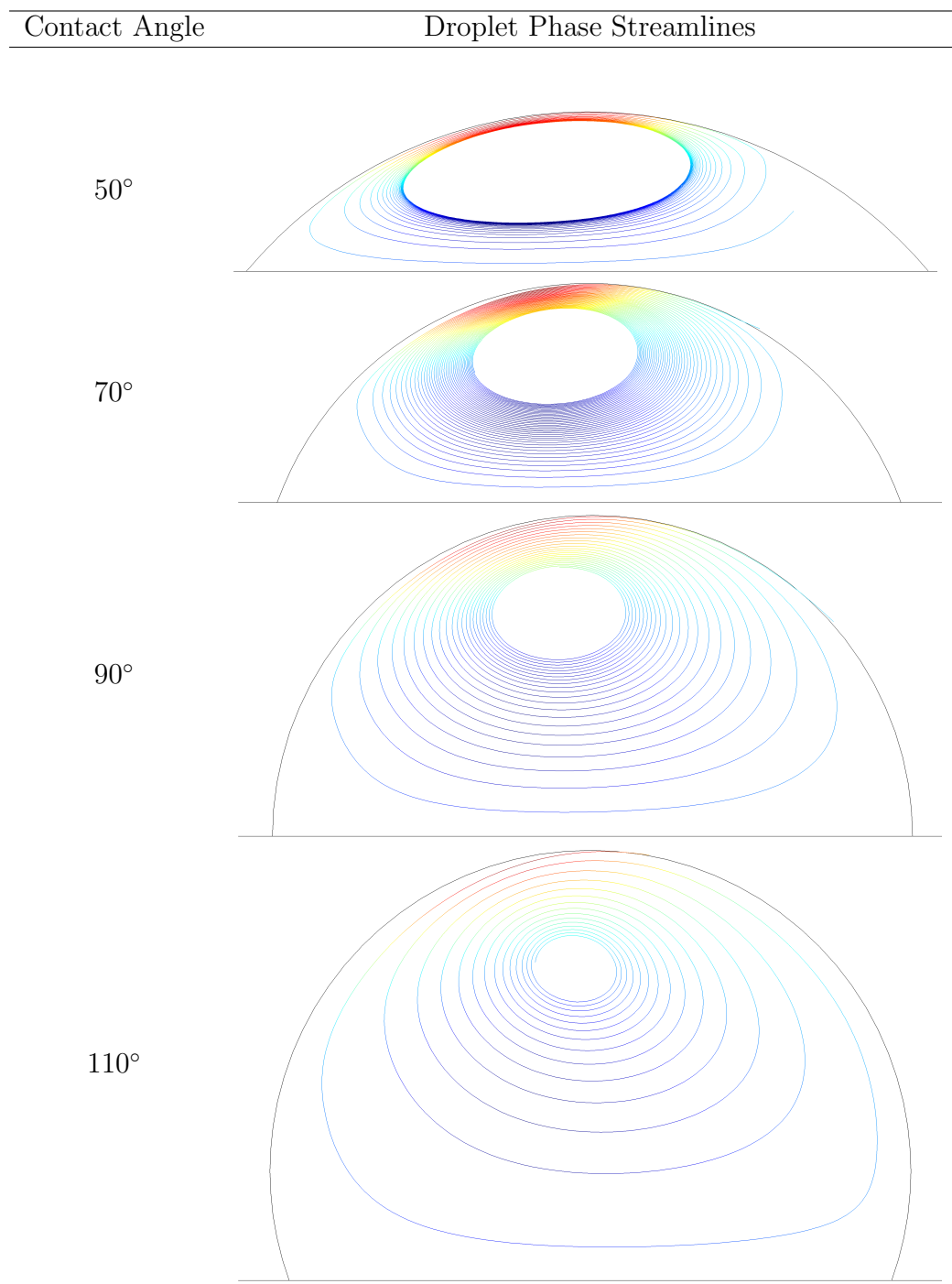


Table 5.10: Variations in apex and maximum surface velocities resulting from altering the contact angle whilst holding the droplet width constant.

Contact Angle [degrees]	Apex Velocity		Max Surface Velocity	
	Velocity $[10^{-4} \text{ms}^{-1}]$	Percentage Change	Velocity $[10^{-4} \text{ms}^{-1}]$	Percentage Change
50	0.054	-79.8%	0.063	-81.5%
70	0.065	-75.6%	0.080	-76.3%
90	2.67	0%	3.39	0%
110	5.75	115%	7.70	127%

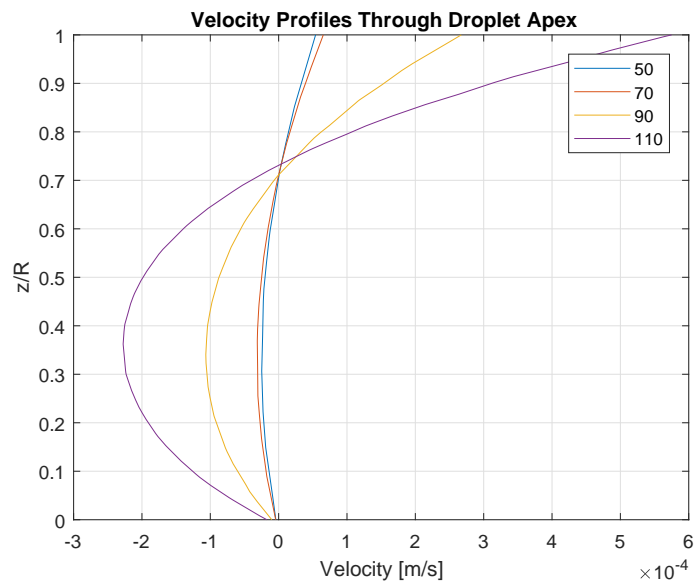


Figure 5.24: Variation in droplet profiles resulting from altering the contact angle of the droplet whilst holding the droplet width constant.

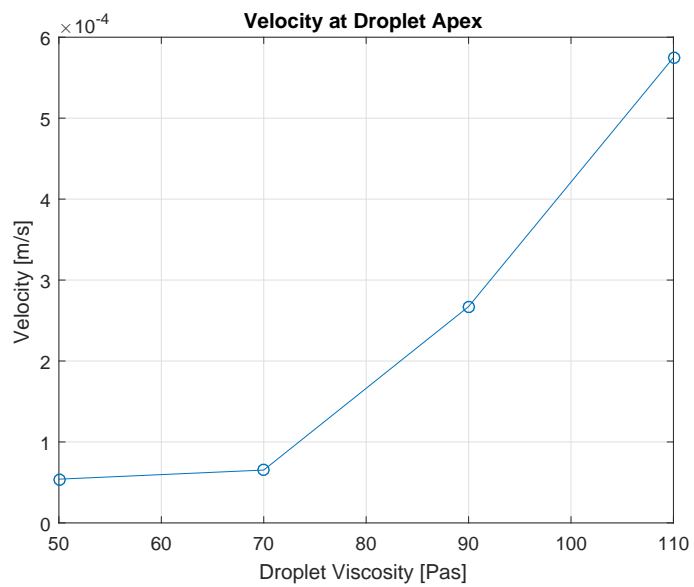


Figure 5.25: Variation in apex velocity resulting from altering the contact angle of the droplet whilst holding the droplet width constant.

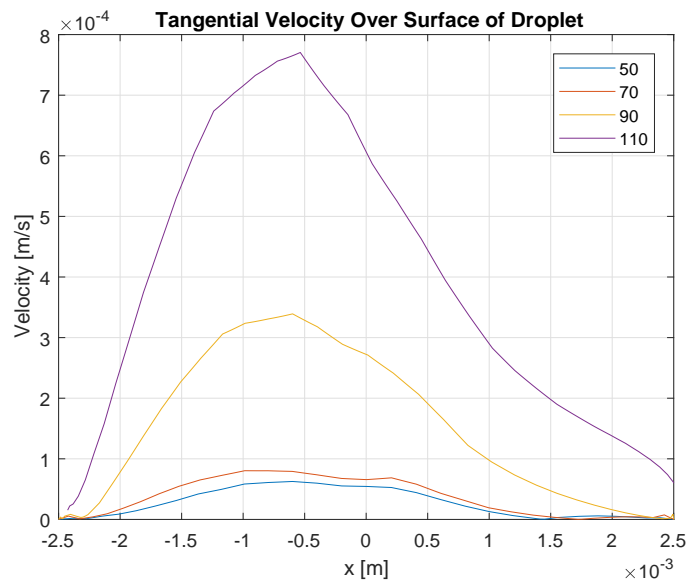


Figure 5.26: Variation in surface velocity resulting from altering the contact angle of the droplet whilst holding the droplet width constant.

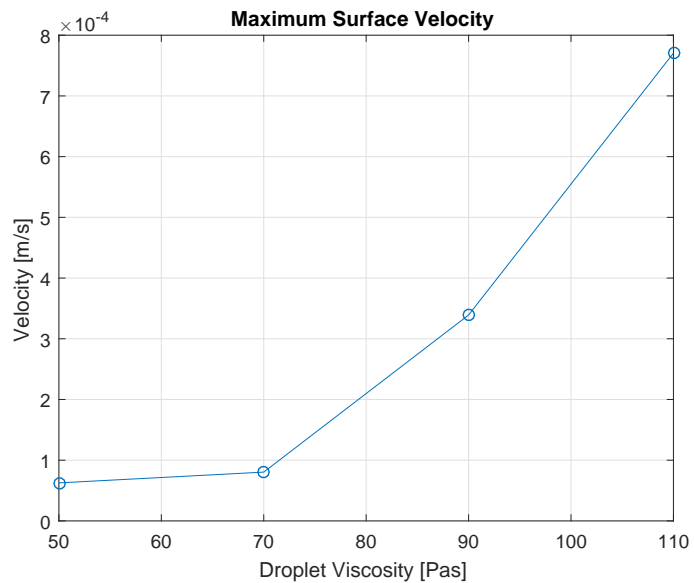


Figure 5.27: Variation in maximum surface velocity resulting from altering the contact angle of the droplet whilst holding the droplet width constant.

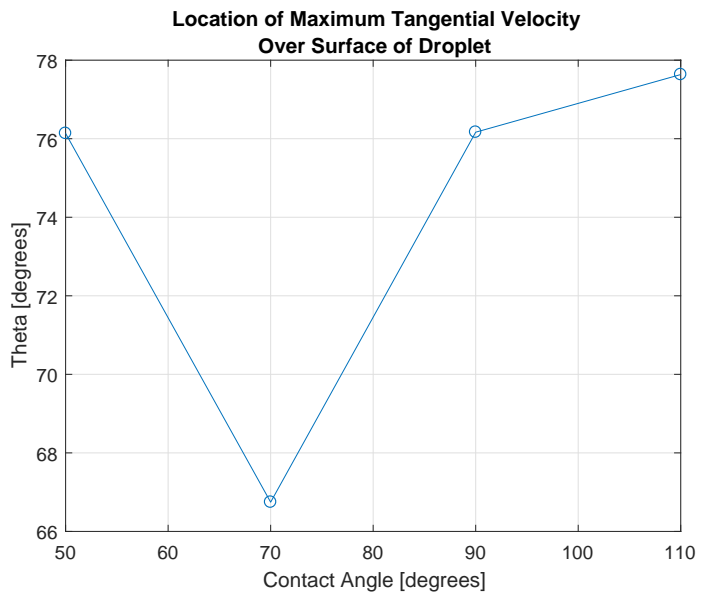


Figure 5.28: Variation in location of maximum surface velocity resulting from altering the contact angle of the droplet whilst holding the droplet width constant.

5.5 Viscosity

The effect of altering the relative humidity of the Nitrogen passing over the droplets is seen to range the measured viscosities from 16Pas to 791Pas [3]. In addition to this, the calibration curve constructed used particle viscosities in the range $10^{-3} < \mu < 10^3 \text{ Pas}$. The droplet viscosity of the COMSOL model was ranged from the current value of 1Pas up to 1000Pas to consider a similar range as in the experiment. In order to accurately model a droplet at steady state after increasing its viscosity, the timescale of the simulation must be lengthened. This is due to the slower rate of growth of the viscous diffusion length. The particles of the water and droplet fluids at the droplet surface move at the same velocity as designated by shear continuity. As the elapsed time of the experiment increases, the region of droplet fluid affected by the motion of the surface increases toward the center. In other words, the distance away from the surface that particles begin to move increases as the droplet moves towards steady state. The perpendicular distance from the surface to the first zero velocity particle is known as the viscous diffusion length. The relationship between the rate of growth of the viscous diffusion length and the increasing droplet viscosity was approximated using the analytical solution. The ratio of droplet velocities predicted by the analytical model at two different viscosities was calculated. The timescale required was then assumed to change by the same ratio. As the analytical solution predicts the droplet fluid velocity to be inversely proportional to the viscosity, the ratio between timescale is equal to the ratio of viscosities. The resulting timescales applied to the study are given in table 5.11.

Figures 5.30 and 5.32 show that increasing the viscosity of the droplet does not change the flow patterns within the droplet (with tolerance of minor variations), instead only decreasing the velocity. The location of maximum surface velocity remains constant at 76.2° from the forward stagnation point. The relationship between the velocity within the droplet and the viscosity was investigated in figures 5.33 and 5.34 with the corresponding data shown in table 5.12. When plotted on a log scale, the relationship is seen to be linear for both the maximum tangential surface velocity and the velocity at the droplet apex. The experimental data presented by

Table 5.11: Variations in apex and maximum surface velocities resulting from altering the droplet viscosity.

Droplet Viscosity [Pas]	Timescale (start,step,stop) [secs]
1	(0,0.1,15)
5	(0,0.5,75)
10	(0,1,150)
50	(0.5,750)
100	(0,10,1500)
500	(0.5,7500)
1000	(0,100,15000)

Renbaum-Wolff et al [4] are also seen to from a similar relationship. Renbaum-Wolff et al fitted the data using a single term power law of the form $u = a\mu^b$ where u is the average bead speed, μ is the droplet viscosity and a and b represent constants. The same parameters are used to fit the apex and maximum surface velocity data from COMSOL. The resulting power law curves are shown in figures 5.33 and 5.34 with comparison to the analytical model predictions. The values of the constants of these curves are given in table 5.13.

When considering a log scale, the analytical and numerical results agree fairly well with each other with the apex and maximum surface velocities varying by 26.8% and 7.8% respectively from the analytical result for constant 'a' and 6.5% and 5.7% respectively from the analytical result for constant 'b'. The relationship formed by Renbaum-Wolff et al, under experimental conditions and measuring the average bead speed was $u = (2.73 \times 10^{-7})\mu^{-0.955}$ in meters per second. The value of the constant 'a' varies considerably to the results of table 5.13 due to its dependency on various parameters. The exponent however, defines the slope of the log plot of bead speed against viscosity. The values of the constant 'b' should equal one another as they are a measure of the relationship between viscosity and droplet motion. The COMSOL data produces 'b' values 2.10% and 1.20% higher (less negative) than the value found by Renbaum-Wolff. This close result, combined with the very close proximity of these values to the analytical solution of -1, validates both the COMSOL model and the analytical solution to a high degree.

Table 5.12: Variations in apex and maximum surface velocities resulting from altering the droplet viscosity.

Viscosity [Pas]	Apex Velocity		Max Surface Velocity	
	Velocity [ms ⁻¹]	Percentage Change	Velocity [ms ⁻¹]	Percentage Change
1	2.67×10^{-4}	0%	3.39×10^{-4}	0%
5	6.61×10^{-5}	-75.3%	7.08×10^{-5}	-79.1%
10	3.31×10^{-4}	-87.6%	4.39×10^{-5}	-87.1%
50	6.61×10^{-6}	-97.5%	8.78×10^{-6}	-97.4%
100	3.31×10^{-6}	-98.8%	4.39×10^{-6}	-98.7%
500	6.62×10^{-7}	-99.8%	8.78×10^{-7}	-99.7%
1000	3.31×10^{-7}	-99.9%	4.39×10^{-7}	-99.9%

Table 5.13: Comparison of fitted power law function constants between COMSOL data and analytical solution. Recalling the function to be in the form $u = a\eta^b$.

	Velocity	a	b	R^2 value
COMSOL Data	Apex	2.689×10^{-4}	-0.9349	0.9992
COMSOL Data	Max Surface	3.390×10^{-4}	-0.9435	0.9996
Analytical Solution	Max,Apex	3.675×10^{-4}	-1	1

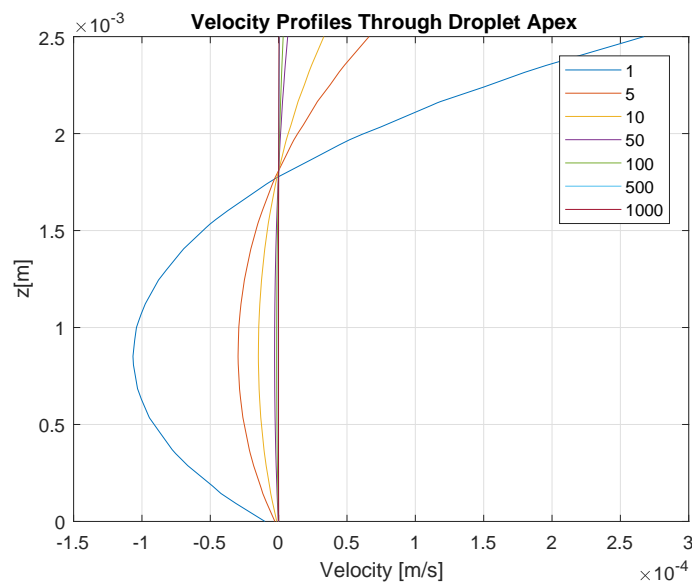


Figure 5.29: Variation in droplet profiles resulting from altering the viscosity of the droplet.

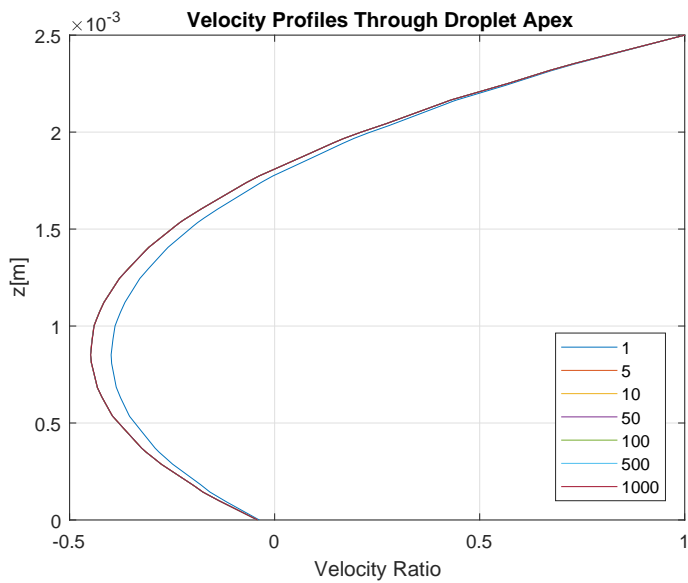


Figure 5.30: Variation in shape of droplet profiles resulting from altering the viscosity of the droplet noting that the x axis is a ratio of the apex velocity.

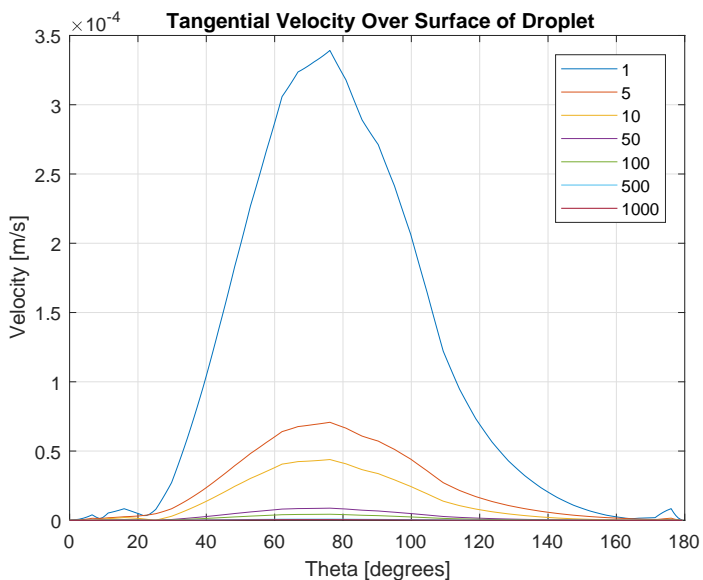


Figure 5.31: Variation in tangential surface velocity resulting from altering the viscosity of the droplet.

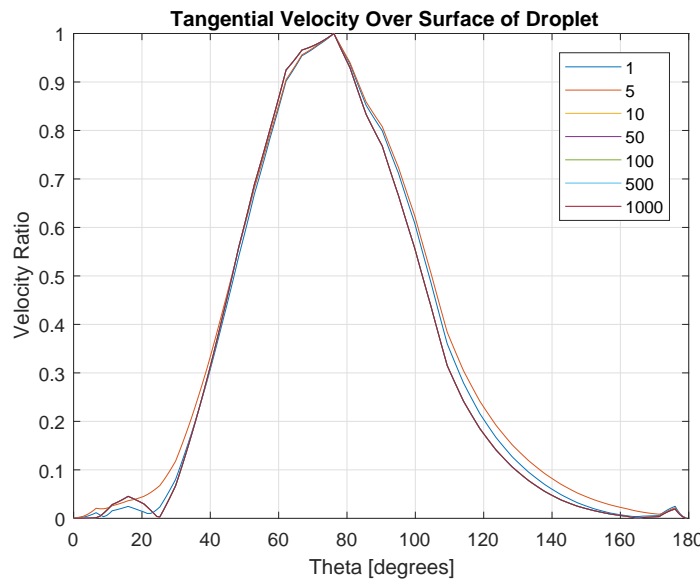


Figure 5.32: Variation in shape of tangential surface velocities resulting from altering the viscosity of the droplet noting that the y axis is a ratio of the maximum velocity.

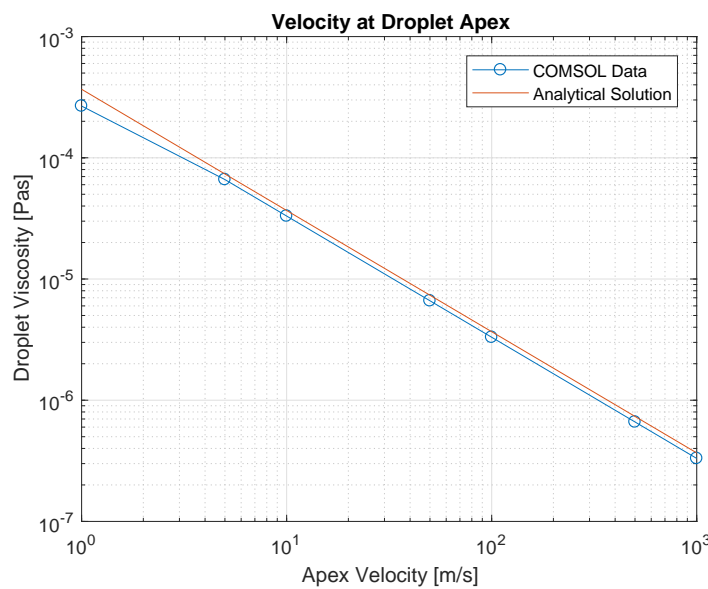


Figure 5.33: Droplet apex velocity as a function of the droplet viscosity, fitted using a single term power function and the prediction made by the analytical solution.

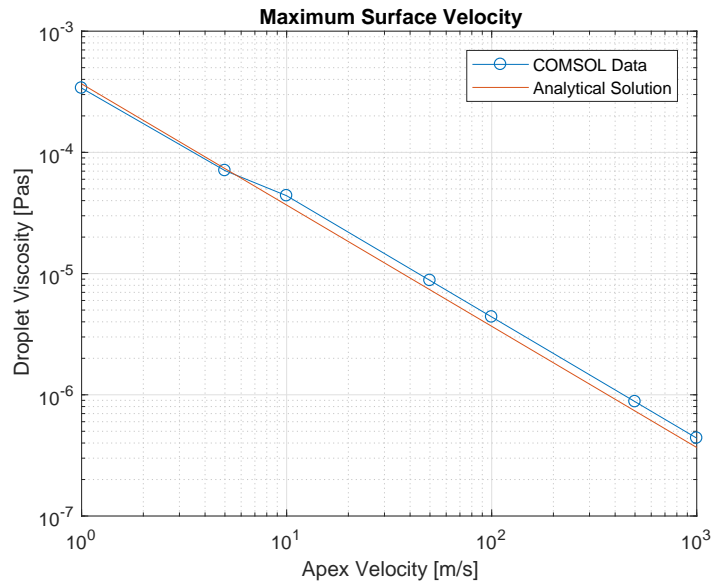


Figure 5.34: Maximum surface velocity as a function of the droplet viscosity, fitted using a single term power function and the prediction made by the analytical solution.

5.6 Summary of Parametric Studies

Table 5.14 summarizes the effect of altering the parameters studied on the apex and maximum surface velocities of the droplet fluid. The minimum and maximum velocities of table 5.14 are the lower and upper values recorded within the range each study. These values do not necessarily correspond to the upper and lower limits of the parameter range as discussed for the case of the contact angle study with a constant droplet height in section 5.4.2. The study resulting in the highest variation was the study of droplet viscosity. This was to be expected as the droplet viscosity is the independent variable of the experiment and therefore does not represent variation due to errors. Altering the viscosity from 1 Pas to 1000 Pas resulted in a change in measured velocities by a factor of approximately 800. The highest contribution of error seen in the parametric studies performed was due to the variation present in contact angle study B (holding the width of the droplet constant, as seen by the observer from above). This is due to the combined effect of contact angle and droplet height increasing simultaneously due to the width constraint placed on the droplet. Ranging the contact angle from 50° to 110° results in

an increase in droplet height from 1.17mm to 3.34mm . This produced an increase in apex and maximum surface velocities by a factor of 10.6 and 12.3 respectively, much larger than the individual ranges of the contributing factors exhibited by contact angle study A and droplet radius studies. Increasing the droplet radius from 1mm to 2.5mm was seen to produce an increase in velocities by a factor of approximately 3. Placing one droplet behind another in the drafting study resulted in variations in droplet apex and maximum surface velocities of approximately 1.9 and 2.4 respectively. The effect of droplet drafting in the experiment is expected to be much less due to the difference in Reynolds numbers of the COMSOL model and that of the flow cell (2062 compared to approximately 0.017). This value therefore represents an upper bound for the potential error that may arise from droplet drafting. Ranging the contact angle from 50 to 110 whilst holding the height of the droplet constant in contact angle study A resulted in droplet velocities increasing by a factor of approximately 1.7. This shows the contact angle of the droplet is less of a contributing factor to experimental error compared to the effect of droplet size, however is still large enough to be given consideration. The surface tension study produced the smallest variation in velocities of approximately 1.2. It should also be noted that the range of surface tensions studied ranged by a factor of 130, much larger than the studies of other potential errors. The surface tension is therefore the least influential parameter of the droplet.

The results of this study show that varying the contact angle whilst holding the width of the droplet constant (contact angle study B) is the most influential source of experimental error by a large margin. This large error is a combination of the effects of varying the height of the droplet as well as the contact angle. These individual contributions are represented by the study of droplet radii and the study of varying the contact angle whilst holding the height of the droplet constant (contact angle study A). The variation present in the droplet drafting study is also large, however it is not considered an accurate measurement the experimental error. Therefore, the errors present in the results can be greatly reduced by restricting the height and contact angles of the droplets studied. The contact angle of the droplet is a material constant with some variation arising from the hydrophobic substrate

used. Therefore, the control over the contact angle of the droplets is minimal. In the construction of the calibration curve presented by Renbaum-Wolff et al [4], the contact angle of the known standards ranged from 55° ato 95° , representing almost the full range of contact angle study A. The associated error of approximately 25% (using the half range error method) due to variations in the contact angle must therefore be incorporated into the results. Contrastingly, the height of the droplet can be controlled indirectly through measuring the droplet width and using the known contact angle of the fluid. The large variation factor of ≈ 2.8 seen in the study of droplet radii can therefore be reduced. The technique currently measures the average velocity of 3-10 beads within 3-5 separate droplets. It is proposed that an effective method of reducing the variation in droplet height is to select a singular droplet based on an experimentally practical tolerance of the droplet width and to increase the number of tracer particles in each droplet. The width constraint of the droplet can be defined as a function of the known contact angle of the material and used to select a droplet that conforms to a predefined height tolerance. This singular droplet, containing many tracer particles, can be studied to produce an average bead speed. This isolation of a single droplet allows for a tighter tolerance to be placed on the allowable droplet height, whilst increasing the tracer particles in the droplets to as many as practicable provides a suitable sample size from which the average velocity can be calculated.

Table 5.14: Variation in droplet fluid velocity over ranges of parameters studied in order from most to least variation in results. 'Contact angle A' represents contact angle study A, where a width constraint was placed on the droplet. 'Contact angle B' represents contact angle study B, where a height constraint was placed on the droplet.

Study Parameter	Parameter Range	Apex Velocity			Max Surface Velocity		
		Min [ms ⁻¹]	Max [ms ⁻¹]	Max Min	Min [ms ⁻¹]	Max [ms ⁻¹]	Max Min
Viscosity	(1-1000) Pas	3.31E-7	2.67E-5	808	4.39E-7	3.39E-4	773
Contact Angle B	(50-110)°	5.40E-5	5.75E-4	10.6	6.26E-5	7.70E-4	12.3
Radius	(1-2.5) mm	1.01E-4	2.67E-4	2.64	1.15E-4	3.39E-4	2.96
Drafting	-	1.59E-4	3.03E-4	1.91	1.66E-4	3.96E-4	2.39
Contact Angle A	(50-110)°	1.55E-4	2.67E-4	1.72	2.03E-4	3.39E-4	1.67
Surface Tension	(0.01-0.13) Nm ⁻¹	2.54E-4	3.27E-4	1.28	3.25E-4	3.75E-4	1.16

REFERENCES

- [1] S. Solomon, D. Qin, M. Manning, Z. Chen, M. Marquis, K.B. Averyt, M. Tignor, and H.L. Miller. *Climate Change 2007: The Physical Science Basis. Contribution of Working Group I to the Fourth Assessment Report of the Intergovernmental Panel on Climate Change*, book section 1: Historical Overview of Climate Change Science, pages 118–121. Cambridge University Press, Cambridge, United Kingdom and New York, NY, USA, 2007. ISBN:978-0-521-88009-1.
- [2] S. Solomon, D. Qin, M. Manning, Z. Chen, M. Marquis, K.B. Averyt, M. Tignor, and H.L. Miller. *Climate Change 2007: The Physical Science Basis. Contribution of Working Group I to the Fourth Assessment Report of the Intergovernmental Panel on Climate Change*, book section 2: Changes in Atmospheric Constituents and in Radiative Forcing, pages 131–216. Cambridge University Press, Cambridge, United Kingdom and New York, NY, USA, 2007. ISBN:978-0-521-88009-1.
- [3] L. Renbaum-Wolff, J. W. Grayson, A. P. Bateman, M. Kuwata, M. Sellier, B. J. Murray, J. E. Shilling, S. T. Martin, and A. K. Bertram. Viscosity of Alpha-Pinene Secondary Organic Material and Implications for Particle Growth and Reactivity. *Proceedings of the National Academy of Sciences of the United States of America*, 110(20):8014–8019, April 25 2013. doi:10.1073/pnas.1219548110. ISSN:0027-8424.
- [4] L. Renbaum-Wolff, J. W. Grayson, and A. K. Bertram. Technical Note: New Methodology for Measuring Viscosities in Small Volumes Characteristic of Environmental Chamber Particle Samples. *Atmospheric Chemistry and Physics*, 13(2):791–802, January 22 2013. doi:10.5194/acp-13-791-2013. ISSN:1680-7324.
- [5] Daniel J. Jacob. *Aerosols*, book section 8, pages 144–148. Princeton University Press, Princeton, New Jersey, United States, January 1999. ISBN:9780691001852.
- [6] E. Saukko, A. T. Lambe, P. Massoli, T. Koop, J. P. Wright, D. R. Croasdale, D. A. Pedernera, T. B. Onasch, A. Laaksonen, P. Davidovits, D. R. Worsnop, and A. Virtanen. Humidity-Dependent Phase State of SOA Particles from Biogenic and Anthropogenic Precursors. *Atmospheric Chemistry and Physics*, 12(16), August 17 2012. doi:10.5194/acp-12-7517-2012. ISSN:1680-7324.
- [7] A. Voiland. Aerosols: Tiny Particles, Big Impact. November 2 2010.

- <http://earthobservatory.nasa.gov/Features/Aerosols/>. Accessed March 15 2016.
- [8] J. De Gouw and J. L. Jimenez. Organic Aerosols in the Earth's Atmosphere. *Environmental Science and Technology*, 43(20):7614–7618, September 16 2009. doi:10.1021/es9006004. ISSN:0013-936X (Print) 0013-936X (Linking).
 - [9] J. T. Houghton, Y. Ding, D. J. Griggs, M. Noguer, P. J. van der Linden, X. Dai, K. Maskell, and C. A. Johnson. *IPCC, 2001: Climate Change 2001: the scientific basis. Contribution of Working Group 1 to the Third Assessment Report of the Intergovernmental Panel on Climate Change*, book section 5: Aerosols, their Direct and Indirect Effects, pages 289–348. Cambridge University Press, Cambridge, United Kingdom and New York, NY, USA, 2001. ISBN:0521 80767 0.
 - [10] M. Kanakidou, J. H. Seinfeld, S. N. Pandis, I. Barnes, F. J. Dentener, M. C. Facchini, R. Van Dingenen, B. Ervens, A. Nenes, C. J. Nielsen, E. Swietlicki, J. P. Putaud, Y. Balkanski, S. Fuzzi, J. Horth, G. K. Moortgat, R. Winterhalter, C. E. L. Myhre, K. Tsagaridis, E. Vignati, E. G. Stephanou, and J. Wilson. Organic Aerosol and Global Climate Modelling: A Review. *Atmospheric Chemistry and Physics*, 5(4):1053–1123, March 30 2005. doi:10.5194/acp-5-1053-2005. ISSN:1680-7324.
 - [11] B. Allen. Atmospheric Aerosols: What Are They, and Why Are They So Important?. July 13 2015. <https://www.nasa.gov/centers/langley/news/factsheets/Aerosols.html>. Accessed March 15 2016.
 - [12] J. A. de Gouw, A. M. Middlebrook, C. Warneke, P. D. Goldan, W. C. Kuster, J. M. Roberts, F. C. Fehsenfeld, D. R. Worsnop, M. R. Canagaratna, A. A P Pszenny, W. C. Keene, M. Marchewka, S. B. Bertman, and T. S. Bates. Budget of Organic Carbon in a Polluted Atmosphere: Results from the New England Air Quality Study in 2002. *Atmospheric Chemistry and Physics*, 110(6):1–22, August 27 2005. doi:10.1029/2004JD005623. ISSN:0148-0227.
 - [13] Scott C. Herndon, Timothy B. Onasch, Ezra C. Wood, Jesse H. Kroll, Manjula R. Canagaratna, John T. Jayne, Miguel A. Zavala, W. Berk Knighton, Claudio Mazzoleni, Manvendra K. Dubey, Ingrid M. Ulbrich, Jose L. Jimenez, Robert Seila, Joost A. de Gouw, Benjamin de Foy, Jerome Fast, Luisa T. Molina, Charles E. Kolb, and Douglas R. Worsnop. Correlation of Secondary Organic Aerosol with Odd Oxygen in Mexico City. *Geophysical Research Letters*, 35(15):1–6, June 7 2008. doi:10.1029/2008GL034058. ISSN:1944-8007.
 - [14] R. J. Weber, A. P. Sullivan, R. E. Peltier, A. Russell, B. Yan, M. Zheng, J. de Gouw, C. Warneke, C. Brock, J. S. Holloway, E. L. Atlas, and

- E. Edgerton. A Study of Secondary Organic Aerosol Formation in the Anthropogenic-Influenced Southeastern United States. *Journal of Geophysical Research: Atmospheres*, 112(D13), July 6 2007. doi:10.1029/2007JD008408. ISSN:2156-2202.
- [15] N. Takegawa, T. Miyakawa, Y. Kondo, D. R. Blake, Y. Kanaya, M. Koike, M. Fukuda, Y. Komazaki, Y. Miyazaki, A. Shimono, and T. Takeuchi. Evolution of Submicron Organic Aerosol in Polluted Air Exported From Tokyo. *Geophysical Research Letters*, 33(15), August 9 2006. doi:10.1029/2006GL025815. ISSN:1944-8007.
- [16] L. I. Kleinman, S. R. Springston, J. Wang, P. H. Daum, Y. N. Lee, L. J. Nunnermacker, G. I. Senum, J. Weinstein-Lloyd, M. L. Alexander, J. Hubbe, J. Ortega, R. A. Zaveri, M. R. Canagaratna, and J. Jayne. The Time Evolution of Aerosol Size Distribution Over the Mexico City Plateau. *Atmospheric Chemistry and Physics*, 9(13):4261–4278, July 3 2009. doi:10.5194/acp-9-4261-2009. ISSN:1680-7316.
- [17] T. Novakov and C. E. Corrigan. Cloud Condensation Nucleus Activity of the Organic Component of Biomass Smoke Particles. *Geophysical Research Letters*, 23(16):2141–2144, August 1 1996. doi:10.1029/96GL01971. ISSN:1944-8007.
- [18] J. Heintzenberg. Fine Particles in the Global Troposphere: A Review. *Tellus Series B: Chemical and Physical Meteorology*, 41B(2):149–160, April 1989. doi:10.1111/j.1600-0889.1989.tb00132.x. ISSN:1600-0889.
- [19] I. Riipinen, J. R. Pierce, T. Yli-Juuti, T. Nieminen, S. Hakkinen, M. Ehn, H. Junninen, K. Lehtipalo, T. Petaja, J. Slowik, R. Chang, N. C. Shantz, J. Abbatt, W. R. Leaitch, V. M. Kerminen, D. R. Worsnop, S. N. Pandis, N. M. Donahue, and M. Kulmala. Organic Condensation: a Vital Link Connecting Aerosol Formation to Cloud Condensation Nuclei (CCN) Concentrations. *Atmospheric Chemistry and Physics*, 11(8):3865–3878, April 27 2011. doi:10.5194/acp-11-3865-2011. ISSN:1680-7324.
- [20] I. Lagzi, R. Meszaros, G. Gelybo, and A. Leelossy. *Atmospheric Chemistry*, book section 9: Aerosol Particles, pages 89–101. Eötvös Loránd University Faculty of Science Institute of Geography and Earth Science, Budapest, Egyetem tr 1-3, Hungary, 2013.
- [21] P. Zannetti. *Air Pollution Modelling: Theories, Computational Methods and Available Software*, book section 10: Dry and Wet Deposition, pages 250–262. Springer US, Boston, MA, 1990. doi:10.1007/978-1-4757-4465-1-10. ISBN:978-1-4757-4465-1.
- [22] Daniel J. Jacob. *Chemical Transport Models*, book section 5: Deposition Processes, pages 1–7. Harvard University, Cambridge, USA, 2006.

- [23] M. Amodio, S. Catino, P. R. Dambruoso, et al. Atmospheric deposition: Sampling procedures, analytical methods, and main recent findings from the scientific literature. *Advances in Meteorology*, 2014:1–27, June 22 2014. doi:10.1155/2014/161730. ISSN:1687-9309.
- [24] E. Morabito, D. Contini, F. Belosi, A. M. Stortini, L. Manodori, and A. Gambaro. Atmospheric deposition of inorganic elements and organic compounds at the inlets of the venice lagoon. *Advances in Meteorology*, 2014:1–10, July 7 2014. doi:10.1155/2014/158902. ISSN:1687-9309.
- [25] M. Langner, T. Draheim, and W. Endlicher. *Perspectives in Urban Ecology: Ecosystems and Interactions between Humans and Nature in the Metropolis of Berlin*, volume 1, book section 2: Particulate Matter in the Urban Atmosphere: Concentration, Distribution, Reduction Results of Studies in the Berlin Metropolitan Area, pages 15–39. Springer Berlin Heidelberg, Heidelberg, Berlin, 2011. doi:10.1007/978-3-642-17731-6. ISBN:978-3-642-17731-6.
- [26] F. Giorgi. Dry Deposition Velocities of Atmospheric Aerosols as Inferred by Applying a Particle Dry Deposition Parameterization to a General Circulation Model. *Tellus B*, 40B(1):23–41, February 1988. doi:10.1111/j.1600-0889.1988.tb00210.x. ISSN:1600-0889.
- [27] W. Ruijrok, C. I. Davidson, W. Nicholson, et al. Dry deposition of particles: Implications and recommendations for mapping of deposition over europe. *Chemical and Physical Meteorology*, 47B(5):587–601, 1995. doi:10.3402/tellusb.v47i5.16074. ISSN:0280-6509.
- [28] M. L. Wesely and B. B. Hicks. A Review of the Current Status of Knowledge on Dry Deposition. *Atmospheric Environment*, 34(12-14):2261–2282, September 11 1999. doi:10.1016/S1352-2310(99)00467-7. ISSN:1352-2310.
- [29] G. A Sehmel and W. H Hogson. A Model for Predicting Dry Deposition of Particles and Gases to Environmental Surfaces. In *85th American Institute of Chemical Engineers National Meeting*, AIChE symposium, Philadelphia, PA, USA, January 1978. Battelle: Pacific Northwest Laboratories. PNL-SA-6721. CONF-780611-10.
- [30] C. Andronache. Estimates of Sulfate Aerosol Wet Scavenging Coefficient for Locations in the Eastern United States. *Atmospheric Environment*, 38(6):795–804, February 1 2004. doi:10.1016/j.atmosenv.2003.10.035. ISSN:1352-2310.
- [31] Global Climate Change. Chapter 6.6.1. Sources and Sinks of Aerosols. <http://www.global-climate-change.org.uk/contents.php>, 1999.

- [32] J. Davies. All About Aerosol. Chapter 1.1:Aerosol in the Atmosphere. 2014. <http://allaboutaerosol.com/aerosol-in-the-atmosphere/>. Accessed March 12 2016.
- [33] S. Solomon, D. Qin, M. Manning, Z. Chen, M. Marquis, K.B. Averyt, M. Tignor, and H.L. Miller. *Climate Change 2007: The Physical Science Basis. Contribution of Working Group I to the Fourth Assessment Report of the Intergovernmental Panel on Climate Change*, book section 7.2.1.1:Water Vapour Feedback, page 505. Cambridge University Press, Cambridge, United Kingdom and New York, NY, USA, 2007. ISBN:978-0-521-88009-1.
- [34] J. P. Putaud, F. Raes, R. Van Dingenen, E. Briggemann, et al. A European Aerosol Phenomenology 2: Chemical Characteristics of Particulate Matter at Kerbside, Urban, Rural and Background Sites in Europe. *Atmospheric Environment*, 38(16), May 2004. doi:10.1016/j.atmosenv.2004.01.041. ISSN:25792595.
- [35] W. A. Hall and M. V. Johnston. Oligomer Content of -Pinene Secondary Organic Aerosol. *Aerosol Science and Technology*, 45(1):37–45, January 1 2011. doi:10.1080/02786826.2010.517580. ISSN:0278-6826.
- [36] H. Yu, P. K. Quinn, G. Feingold, L. A. Remer, and R. A. Kahn. *Atmospheric Aerosol Properties and Climate Impacts: A Report by the U.S. Climate Change Science Program and the Subcommittee on Global Change Research*, book section 2.3:Assessments of Aerosol Characterization and Climate Forcing. National Aeronautics and Space Administration, Washington, D.C., USA, January 2009.
- [37] Earth and Space Research (ESR). Glossary: Albedo. August 29 2011. <https://www.esr.org/outreach/glossary/albedo.html>. Accessed March 18 2016.
- [38] Swinburne University of Technology. Cosmos: The Swinburne Astronomy Online Encyclopedia: Albedo. <http://astronomy.swin.edu.au/cosmos/A/Albedo>. Accessed March 22 2016.
- [39] Vronique Perraud, Emily A. Bruns, Michael J. Ezell, Stanley N. Johnson, Yong Yu, M. Lizabeth Alexander, Alla Zelenyuk, Dan Imre, Wayne L. Chang, Donald Dabdub, James F. Pankow, and Barbara J. Finlayson-Pitts. Nonequilibrium Atmospheric Secondary Organic Aerosol Formation and Growth. *Proceedings of the National Academy of Sciences*, 109(8):28362841, January 30 2012. doi:10.1073/pnas.1119909109. PubMedID:22308444.
- [40] M. Shiraiwaa, M. Ammann, T. Koop, and U. Pöschl. Gas Uptake and Chemical Aging of Semisolid Organic Aerosol Particles. *Proceedings of the*

- National Academy of Sciences*, 108(27):11003–11008, June 20 2011.
doi:10.1073/pnas.1103045108. PubMedID:21690350.
- [41] T. Novakov and J. E. Penner. Large Contribution of Organic Aerosols to Cloud-Condensation-Nuclei Concentrations. *Nature*, 365(6449):823–826, October 28 1993. doi:10.1038/365823a0.
 - [42] M. C. Roberts, M. O. Andreae, J. C. Zhou, and P. Artaxo. Cloud Condensation Nuclei in the Amazon Basin: "Marine" Conditions Over a Continent? *Geophysical Research Letters*, 28(14):2807–2810, July 15 2001. doi:10.1029/2000GL012585. ISSN:1944-8007.
 - [43] J. M. Sun and P. A. Ariya. Atmospheric organic and bio-aerosols as cloud condensation nuclei (ccn): A review. *Atmospheric Environment*, 40(5):795–820, February 1 2006. doi:10.1016/j.atmosenv.2005.05.052. ISSN:1352-2310.
 - [44] A. Evans. Understanding Climate Change. March 4 2016. <http://www.climatejustice.org.uk/category/understanding-climate-change/>. Accessed March 26 2016.
 - [45] A. Virtanen, J. Joutsensaari, T. Koop, J. Kannisto, P. Yli-Pirila, J. Leskinen, J. M. Makela, J. K. Holopainen, U. Poschl, M. Kulmala, D. R. Worsnop, and A. Laaksonen. An Amorphous Solid State of Biogenic Secondary Organic Aerosol Particles. *Nature*, 467(7317):824–827, October 4 2010. doi:10.1038/nature09455. ISSN:0028-0836.
 - [46] B. B. Wang, A. T. Lambe, P. Massoli, T. B. Onasch, P. Davidovits, D. R. Worsnop, and D. A. Knopf. The Deposition Ice Nucleation and Immersion Freezing Potential of Amorphous Secondary Organic Aerosol: Pathways for Ice and Mixed-Phase Cloud Formation. *Journal of Geophysical Research: Atmospheres*, 117(D16), August 27 2012. doi:10.1029/2012JD018063. ISSN: 156-2202.
 - [47] M. Shiraiwa and J. H. Seinfeld. Equilibration Timescale of Atmospheric Secondary Organic Aerosol Partitioning. *Geophysical Research Letters*, 39(24), December 18 2012. doi:10.1029/2012GL054008. ISSN:1944-8007.
 - [48] M. Kuwata and S. T. Martin. Phase of Atmospheric Secondary Organic Material Affects its Reactivity. *Proceedings of the National Academy of Sciences*, 109(43):17354–17359, October 23 2012. doi:10.1073/pnas.1209071109. ISSN:1091-6490.
 - [49] Y. Katrib, G. Biskos, P. R. Buseck, P. Davidovits, J. T. Jayne, M. Mochida, M. E. Wise, D. R. Worsnop, and S. T. Martin. Ozonolysis of Mixed Oleic-Acid/Stearic-Acid Particles: Reaction Kinetics and Chemical

- Morphology. *Journal of Physical Chemistry A*, 109(48):10910–10919, October 8 2005. doi:10.1021/jp054714d. ISSN:1089-5639.
- [50] J. C Pipe and H. G. McKinley. Microfluidic Rheometry. *Mechanics Research Communications*, 36(1):110–120, January 1 2009. doi:10.1016/j.mechrescom.2008.08.009. ISSN:0093-6413.
- [51] Z. Han, X. Tang, and B. Zheng. A PDMS Viscometer for Microliter Newtonian Fluid. *The Chinese University of Hong Kong*, page 1828, August 8 2007. doi:10.1088/0960-1317/17/9/011.
- [52] N. Srivastava and M. A. Burns. Analysis of Non-Newtonian Liquids Using a Microfluidic Capillary Viscometer. *Analytical Chemistry*, 78(5):1690–1696, January 11 2006. doi:10.1021/ac0518046. ISSN:0003-2700.
- [53] Julio C. Pita Francisco J. Mller. A Simple Electronic Capillary Microviscometer. *Analytical Biochemistry*, 135(1):106–111, November 1983. doi:10.1016/0003-2697(83)90737-6. ISSN:0003-2697.
- [54] S. T. Hess, S. Huang, A. A. Heikal, and W. W. Webb. Biological and Chemical Applications of Fluorescence Correlation Spectroscopy: A Review. *Biochemistry*, 41(3):697–705, January 22 2002. doi:10.1021/bi0118512. ISSN:0006-2960.
- [55] D. G. Spiller, C. D. Wood, D. A. Rand, and M. R. H. White. Measurement of Single-Cell Dynamics. *Nature*, 465(7299):736–745, June 10 2010. doi:10.1038/nature09232. ISSN:0028-0836.
- [56] B. Wischnewski. Calculation of Thermodynamic State Variables of Nitrogen. http://www.peacesoftware.de/einigewerte/stickstoff_e.html. Accessed July 12 2016.
- [57] R. K. Pathak, A. A. Presto, T. E. Lane, C. O. Stanier, N. M. Donahue, and S. N. Pandis. Ozonolysis of Alpha-Pinene: Parameterization of Secondary Organic Aerosol Mass Fraction. *Atmospheric Chemistry and Physics*, 7(14):38113821, July 24 2007. doi:10.5194/acp-7-3811-2007. ISSN:1680-7324.
- [58] U.S Geological Survey. USGS Water Science School: Surface Tension and Water. May 02 2016. <http://water.usgs.gov/edu/surface-tension.html>. Accessed May 19 2016.
- [59] N. B. Vargaftik, B. N. Volkov, and L. D. Voljak. International Tables of the Surface Tension of Water. *The Journal of Physical Chemical Reference Data*, 12(3):817–820, 1983. doi:10.1063/1.555688. ISSN:0047-2689.
- [60] Dimitris. Borda-Carnot equation Part I. March 9 2016. Accessed October 10 2017.

- [61] Frank M. White. *Fluid Mechanics Seventh Edition, Chapter 6*. McGraw Hill, New York, 2009.
- [62] C. D. Cantwell, D. Barkley, and H. M. Blackburn. Transient growth analysis of flow through a sudden expansion in a circular pipe. *Physics of Fluids*, 22(3):1–15, March 2010. doi:10.1063/1.3313931. ISSN:1070-6631.
- [63] C. Tropea, A. Yarin, and J. F. Foss. *Springer Handbook of Experimental Fluid Mechanics, Volume 1*, book section 5.3.1:Particle Base Techniques, Tracer Particles, pages 288–289. Springer Science and Business Media, Verlag Berlin Heidelberg, 2007. ISBN:978-3-662-49162-1.
- [64] Fabrice COMSOL Multiphysics Blog Post. Schlegel. Which Multiphase Flow Interface Should I Use?. January 27 2015. <https://www.comsol.com/blogs/which-multiphase-flow-interface-should-i-use/>. Accessed July 26 2016.
- [65] Joseph Kestin, Mordechai Sokolov, and William A. Wakeham. Viscosity of liquid water in the range 8c to 150c. *Journal of Physical and Chemical Reference Data*, 7(3):941–948, 1978. doi:10.1063/1.555581.
- [66] COMSOL Multiphysics Inc. *COMSOL Multiphysics User's Guide: Chapter 12, The Fluid Flow Brach, The Laminar Flow Interface*, 4.3 edition, May 2012.
- [67] ANSYS Inc. *ANSYS FLUENT 12.0 Users Guide: Section 7.3.15*, April 2009.
- [68] H. Schlichting and K. Gersten. *Boundary Layer Theory, Ninth Edition*, book section 2.6: Separation of the Boundary Layer, pages 29–48. Springer, Verlag, Berlin, Heidelberg, 2017. doi:10.1007/978-3-662-52919-5, ISBN:978-3-662-52917-1.
- [69] B. P. LeClair, A. E. Hamielec, H. R. Pruppacher, and W. D. Hall. A Theoretical and Experimental Study of the Internal Circulation in Water Drops Falling at Terminal Velocity in Air. *Journal of the Atmospheric Sciences*, 29(4):728–740, January 10 1972. doi:10.1175/1520-0469(1972)029.
- [70] Simon Watkins and Gioacchino Vino. The effect of vehicle spacing on the aerodynamics of a representative car shape. *Journal of Wind Engineering and Industrial Aerodynamics*, 96(6):1232–1239, August 8 2008. doi:10.1016/j.jweia.2007.06.042. ISSN:0167-6105.
- [71] DataPhysics Instruments GmbH. Surface tension values of some common test liquids for surface energy analysis. Februrary 25 2017. http://www.dataphysics.de/fileadmin/user_upload/pdf/DataPhysics_Surface_Tension_Energy.pdf. Accessed August 01 2017.

APPENDIX A

Droplet Model Mesh Study

A.1 Study A: Water Domain

Table A.1: Water Study size settings

Mesh	Water Domain	Droplet Domain
1	Extremely coarse	Normal
2	Extra coarse	Normal
3	Coarser	Normal
4	Coarse	Normal
5	Normal	Normal

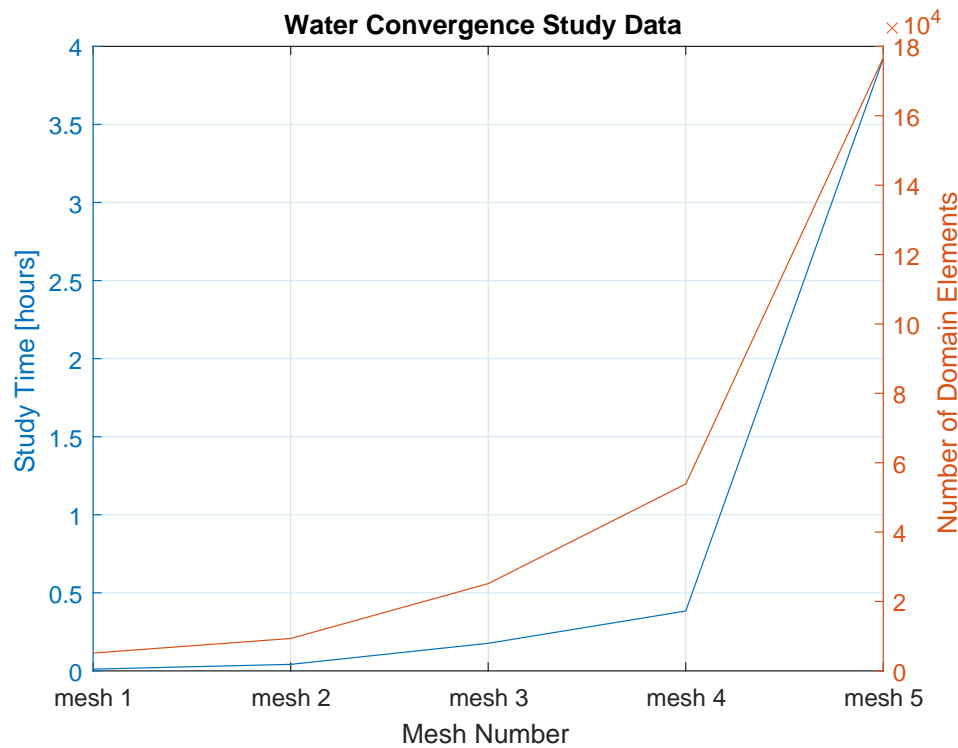
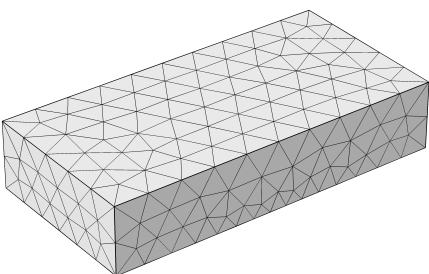
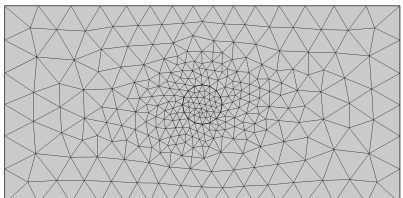
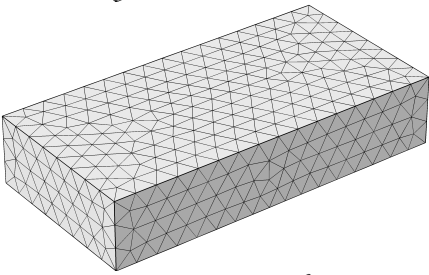
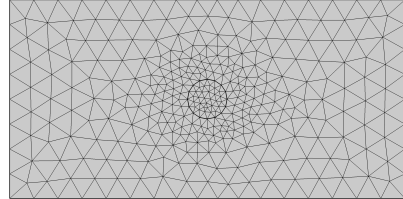
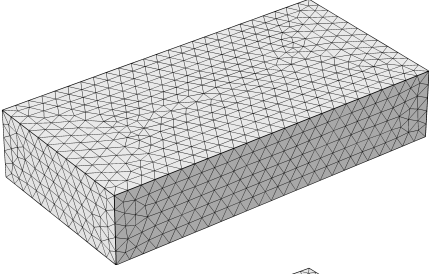
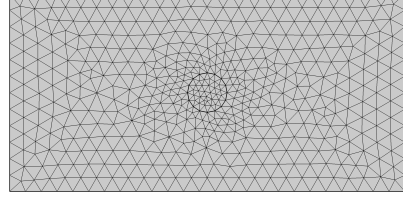
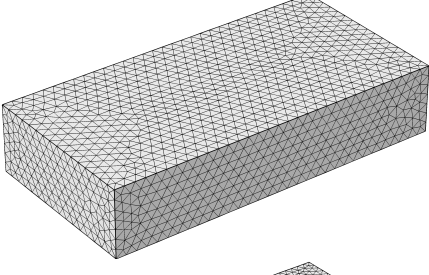
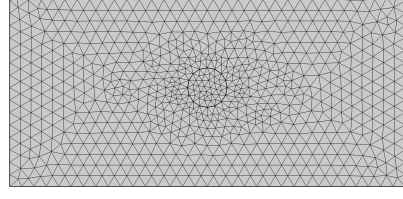
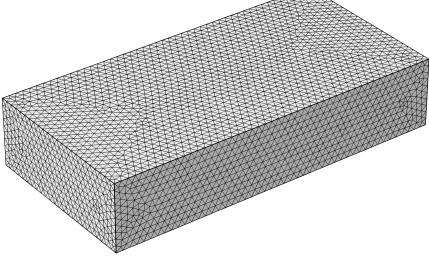
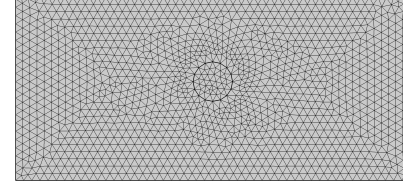


Figure A.1

Table A.2: Water Study meshed domains

Mesh	Isometric View	Bottom View
1		
2		
3		
4		
5		

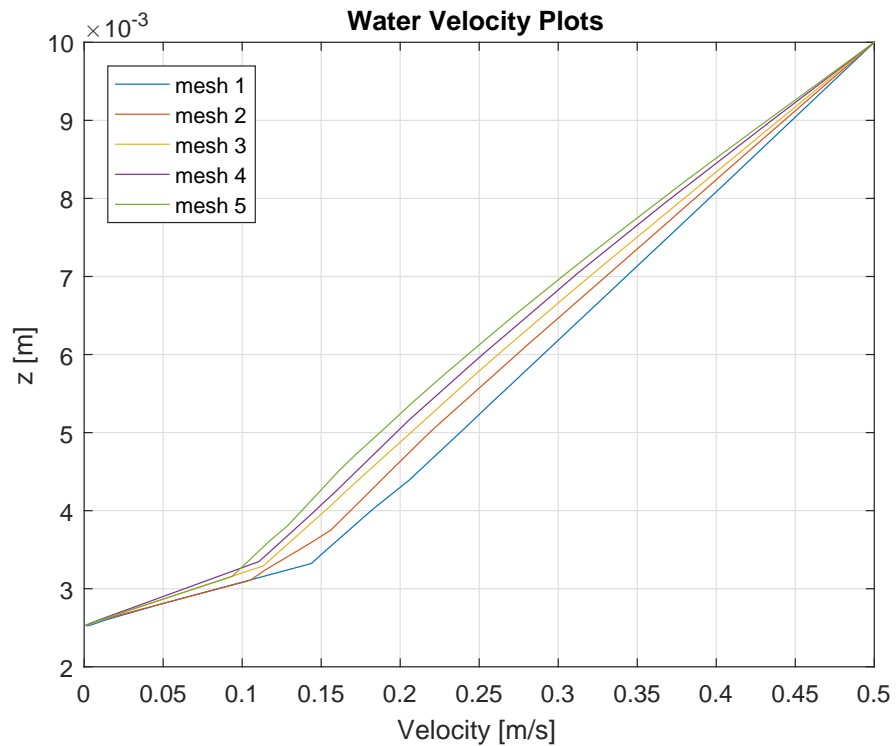


Figure A.2

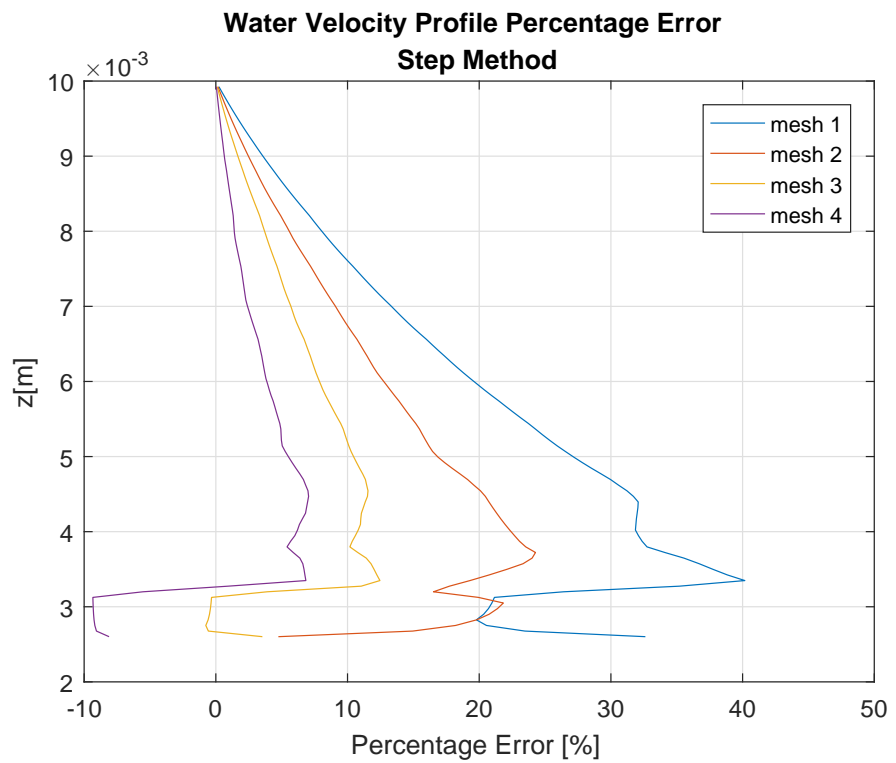


Figure A.3

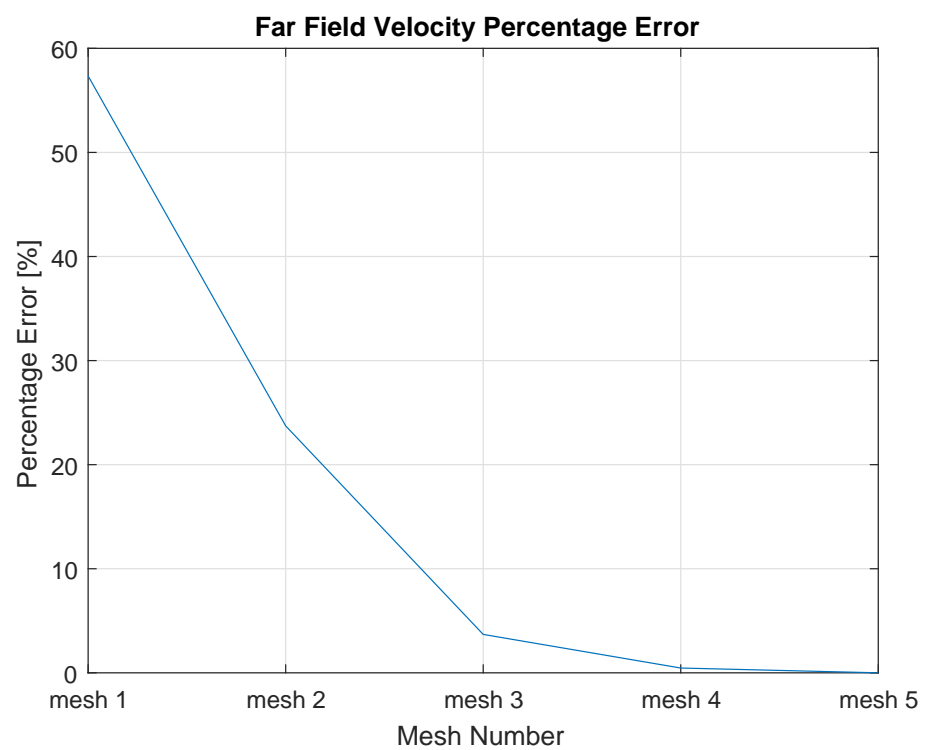


Figure A.4

A.2 Study B: Droplet Domain

Table A.3: Droplet study size settings

Mesh	Water Domain	Droplet Domain
1	Coarser	Finer
2	Coarser	Extra Fine
3	Coarser	Extremely Fine
4	Coarser	Custom

Table A.4: Maximum element and growth rate settings used to define custom mesh relative to COMSOL presets.

Size Setting	Max Element Size ($\times 10^{-4}m$)	Growth Rate
Finer	5.85	1.1
Extra Fine	3.64	1.08
Extremely Fine	2.06	1.05
Custom	1.27	1.09

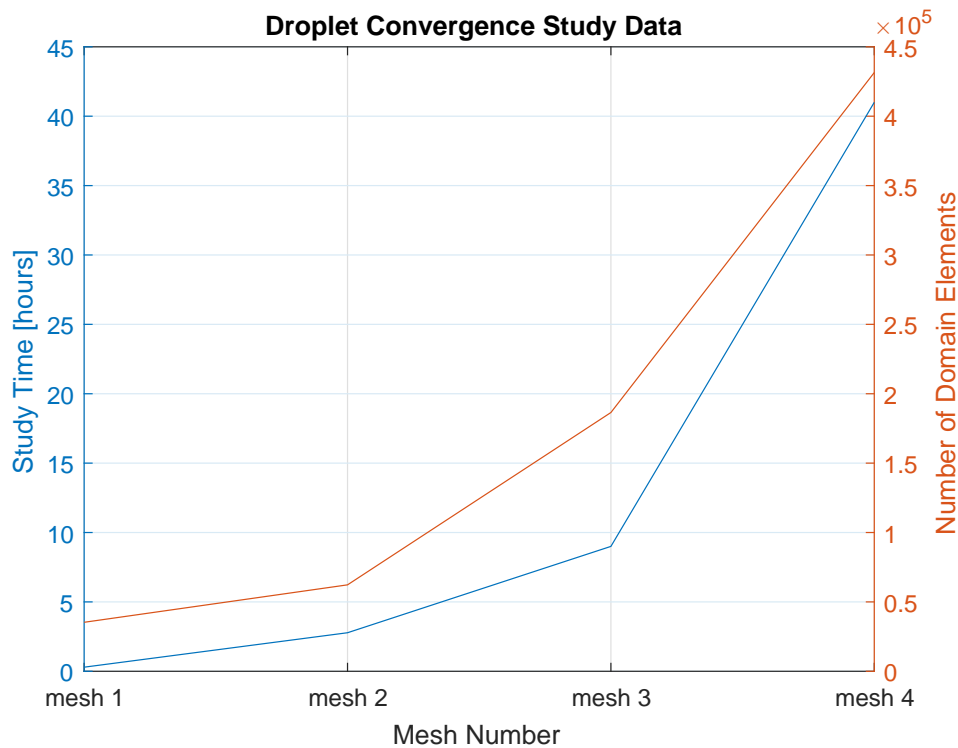
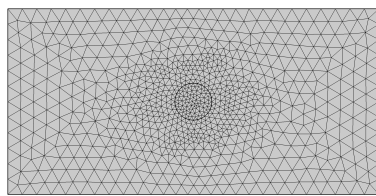
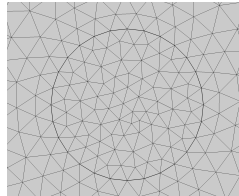
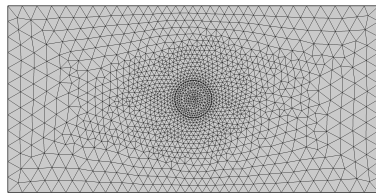
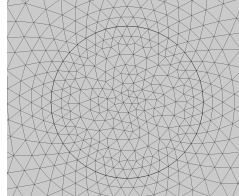
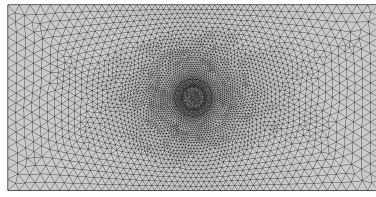
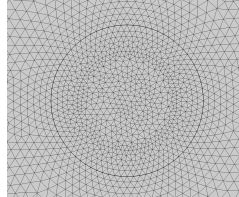
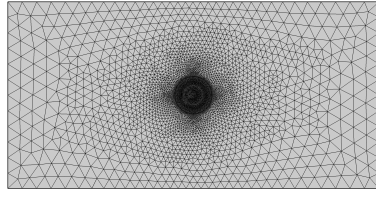
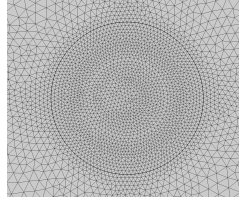
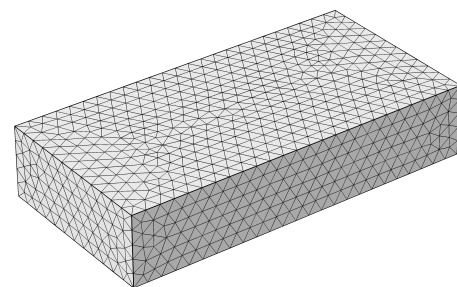
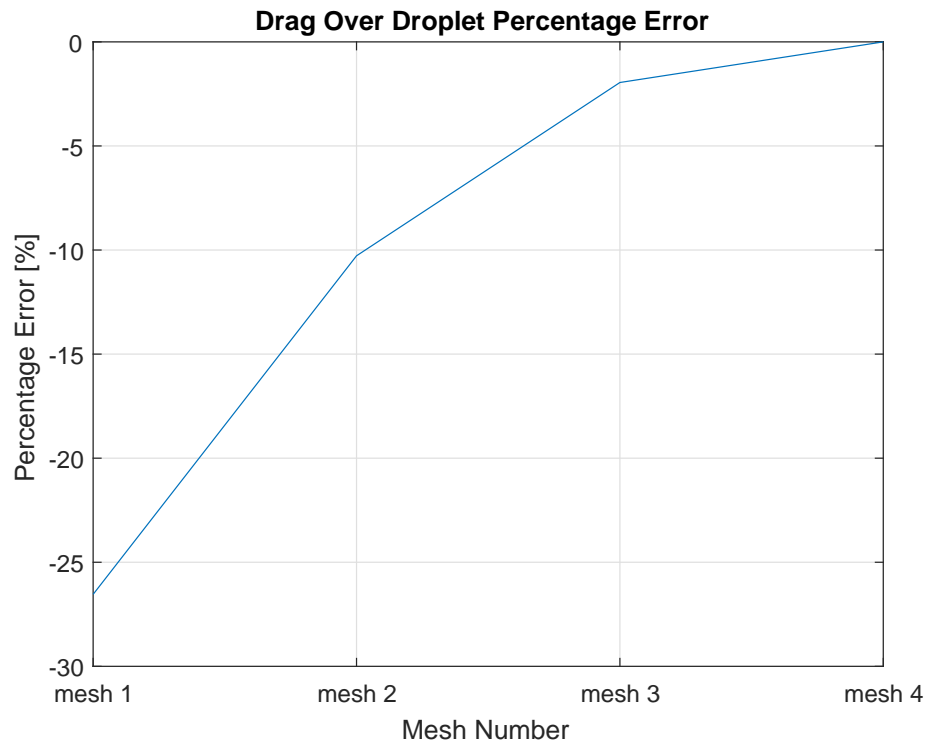
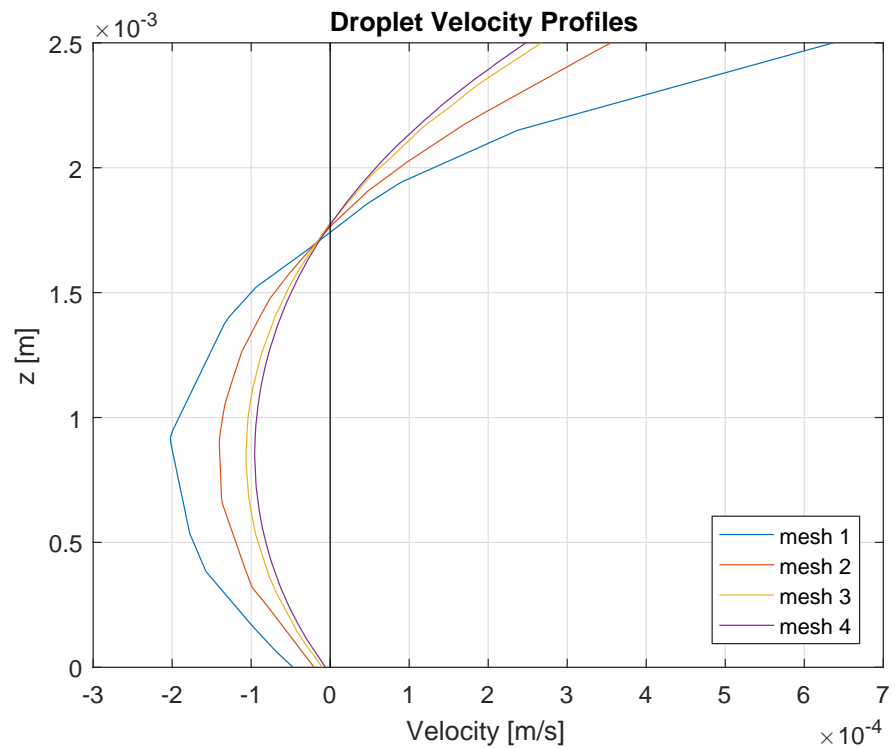


Figure A.5

Table A.5: Droplet Study meshed domains

Mesh	Bottom View	Zoomed
1		
2		
3		
4		

**Figure A.6: Isometric view of droplet study mesh, common to all meshes.**

**Figure A.7****Figure A.8**

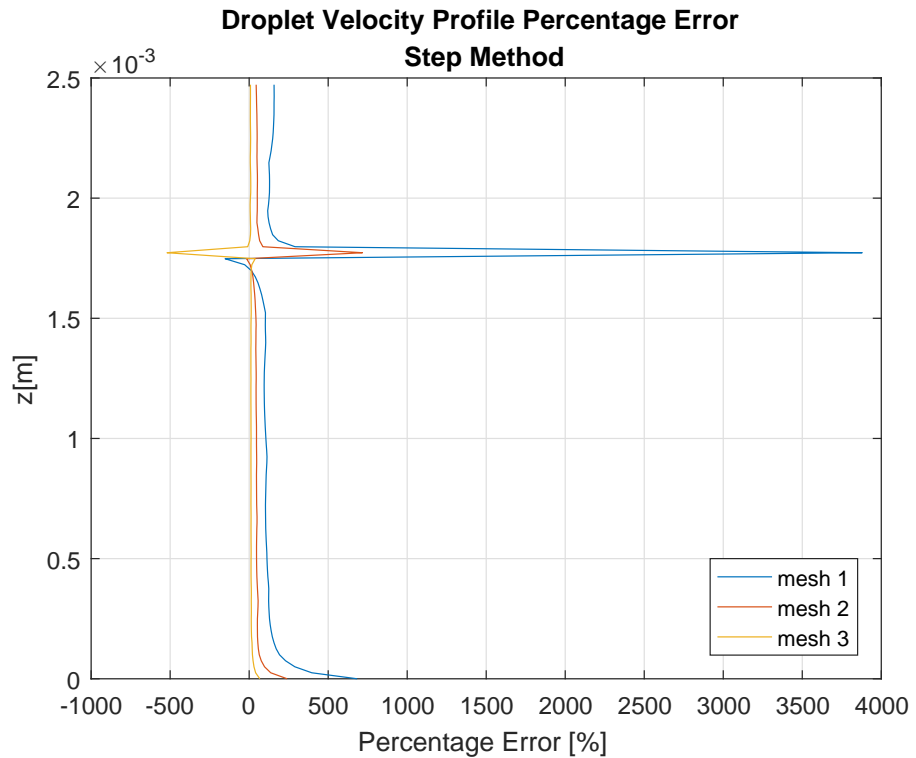


Figure A.9

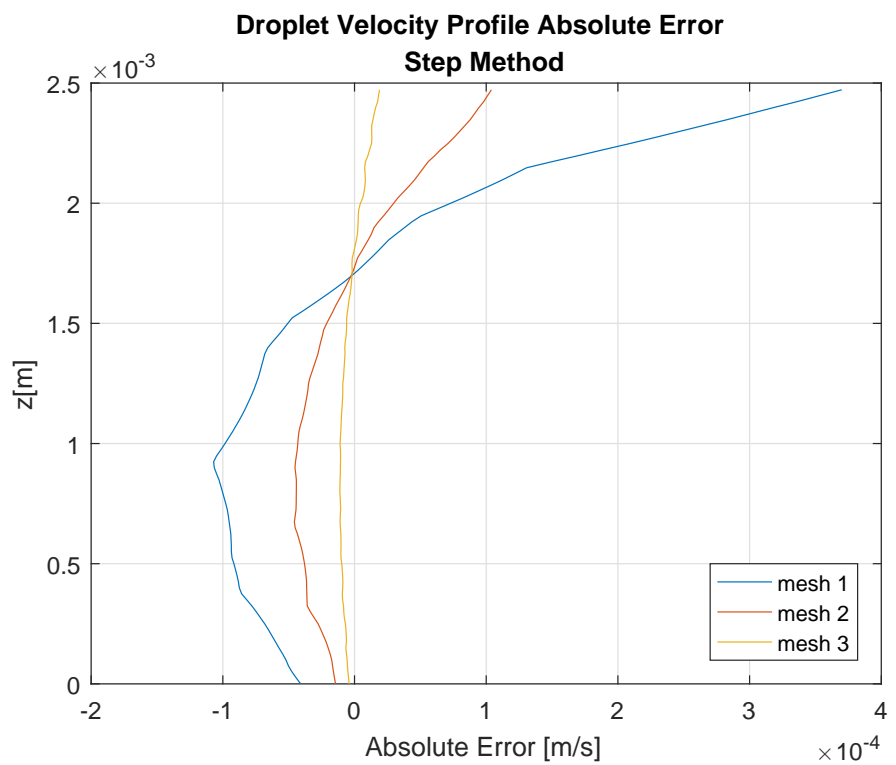


Figure A.10

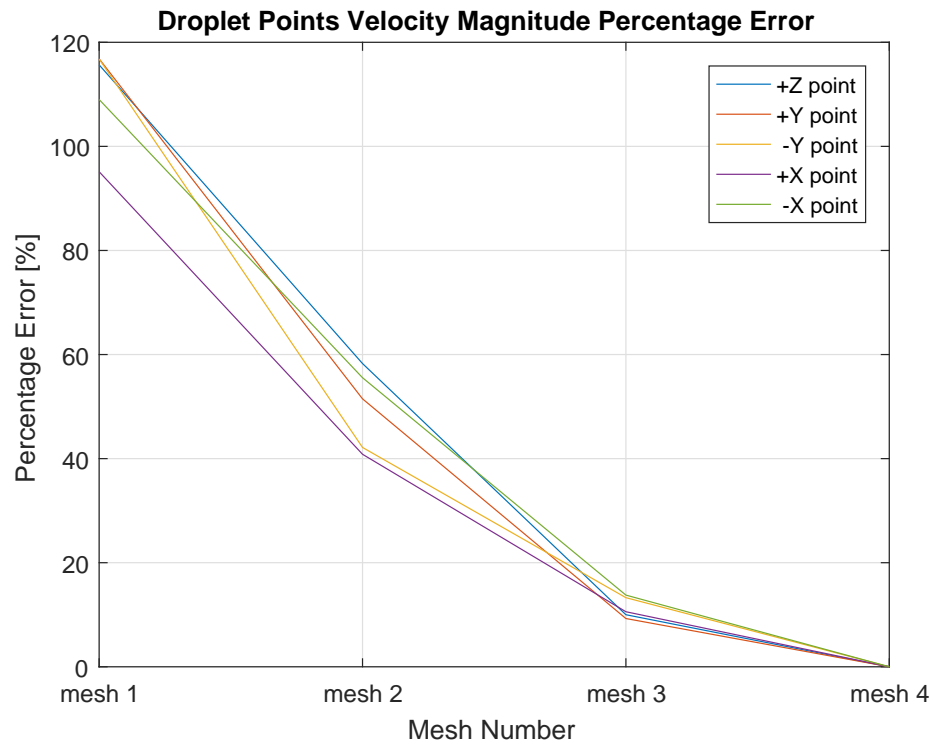


Figure A.11

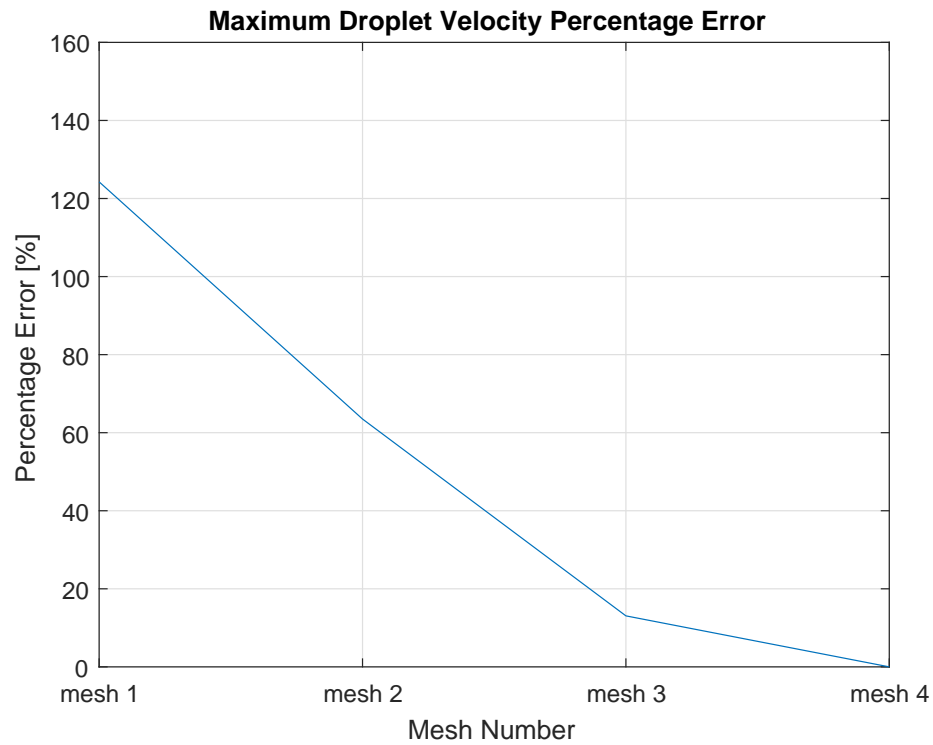


Figure A.12